

REPORT DOCUMENTATION PAGE

AFRL-SR-AR-TR-09-0021

Public reporting burden for this collection of information is estimated to average 1 hour per response, including the time for reviewing in gathering and maintaining the data needed, and completing and reviewing the collection of information. Send comments regarding this of information, including suggestions for reducing this burden to Washington Headquarters Service, Directorate for Information Operations and Reports, 1215 Jefferson Davis Highway, Suite 1204, Arlington, VA 22202-4302, and to the Office of Management and Budget, Paperwork Reduction Project (0704-0188) Washington, DC 20503.

PLEASE DO NOT RETURN YOUR FORM TO THE ABOVE ADDRESS.

1. REPORT DATE (DD-MM-YYYY) 1/31/09		2. REPORT TYPE Final		3. DATES COVERED (From - To) 4/1/2006-10/31/2008	
4. TITLE AND SUBTITLE Coherent Structure and Chaos Control in High Power Microwave and Particle Beam Devices				5a. CONTRACT NUMBER	
				5b. GRANT NUMBER FA9550-06-1-0269	
				5c. PROGRAM ELEMENT NUMBER	
6. AUTHOR(S) Chiping Chen				5d. PROJECT NUMBER	
				5e. TASK NUMBER	
				5f. WORK UNIT NUMBER	
7. PERFORMING ORGANIZATION NAME(S) AND ADDRESS(ES) Massachusetts Institute of Technology 77 Massachusetts Avenue Cambridge, MA 02139				8. PERFORMING ORGANIZATION REPORT NUMBER	
9. SPONSORING/MONITORING AGENCY NAME(S) AND ADDRESS(ES) Dr. Arje Nachman Air Force Office of Scientific Research 875 North Randolph St., Rm 3112 Arlington, VA 22203				10. SPONSOR/MONITOR'S ACRONYM(S) AFOSR/NE	
				11. SPONSORING/MONITORING AGENCY REPORT NUMBER	
12. DISTRIBUTION AVAILABILITY STATEMENT DISTRIBUTION A. Approved for public release; distribution unlimited.					
13. SUPPLEMENTARY NOTES					
14. ABSTRACT This report summarizes research results obtained under the auspices of Air Force Office of Scientific Research, Grant No. FA9550-06-1-0269. In particular, we conducted vigorous theoretical and computational investigations of coherent structures and chaos in a wide range of intense electron beam plasmas relevant to the development of high-power microwave and particle-beam devices for directed energy applications. The research accomplishments includes: a) development of a small-signal theory of magnetrons, b) discovery of vortex structures in relativistic magnetrons, c) discovery of adiabatic thermal equilibria in periodically focused electron beams, d) design of high-brightness circular beam systems, and e) development of elliptic beam theory for high-power microwave device applications.					
15. SUBJECT TERMS					
16. SECURITY CLASSIFICATION OF:			17. LIMITATION OF ABSTRACT	18. NUMBER OF PAGES	19a. NAME OF RESPONSIBLE PERSON
a. REPORT U	b. ABSTRACT U	c. THIS PAGE U	U		19b. TELEPHONE NUMBER (Include area code)

Final Report

**Coherent Structures and Chaos Control in
High-Power Microwave and Charged-Particle Beam Devices**

AFOSR Grant No. FA9550-06-1-0269

Submitted to:

Dr. Arje Nachman
Program Manager
Air Force Office of Scientific Research
875 North Randolph Road
Suite 325, Room 3112
Arlington, VA 22203
Phone: 703-696-8427
FAX: 703-696-8450

Submitted by

Plasma Science and Fusion Center
Massachusetts Institute of Technology
Cambridge, Massachusetts 02139

Principal Investigator

Dr. Chiping Chen

Grant Period

April 1, 2006 – October 31, 2008

20090319163

Cover Page	1
Table of Contents	2
Final Report	3
1. High-Power Magnetron Research	3
1.1 Small-Signal Gain Theory of Non-Relativistic Planar Magnetrons	
1.2 Comparison between Small-Signal Gain Theory and Two-Dimensional Particle-in-Cell Simulations	
1.3 Vortex Structures in Relativistic Magnetrons	
2. Discovery of Adiabatic Thermal Beam Equilibrium in a Periodic Solenoidal Magnetic Field	10
2.1 Kinetic Beam Equilibrium Theory	
2.2 Warm-Fluid Beam Equilibrium Theory	
2.3 Comparison between Theory and Experiment	
3. Design of High-Brightness Circular Electron Beams	13
4. Development of Elliptic Beam Theory for High-Power Microwave Device Applications	16
4.1 Kinetic Equilibrium Theory of Periodically Twisting Elliptic Beams	
4.2 Cold-Fluid Equilibrium Theory of Non-Twisting Elliptic Electron Beams	
4.3 Kinetic Equilibrium Theory of Non-Twisting Elliptic Electron Beams	
4.4 Applications and Simulation Validation of Cold-Fluid and Kinetic Equilibrium Theories	
5. References	24
Compendium of Publications	27

Final Report
Coherent Structures and Chaos Control in
High-Power Microwave and Charged-Particle Beam Devices
AFOSR Grant No. FA9550-06-1-0269

This report summarizes research results obtained under the auspices of Air Force Office of Scientific Research, Grant No. F49620-06-1-0269 (Chen, 2006). In particular, we conducted vigorous theoretical and computational investigations of coherent structures and chaos in a wide range of intense electron beam plasmas relevant to the development of high-power microwave and particle-beam devices for directed energy applications.

The following is a brief summary of our research accomplishments in selected areas, while detailed findings are described in the preprints cited in this report.

1. High-Power Magnetron Research (Zhou and Chen, 2007 and 2008; Davies, Zhou and Chen, 2007; Davies, Chen and Zhou, 2008)

Under the auspices of the grant (Chen, 2006), we have developed a small-signal theory of a non-relativistic magnetron using a planar model with a thin electron cloud (Zhou and Chen, 2007 and 2008). The theory includes both inertial effects and electromagnetic effects in a Floquet expansion. We have derived an analytical dispersion relation of such a planar magnetron, and calculated the growth rate analytically. We have shown that the magnetron instability involves the resonance between the electron cloud and the slow waves in the magnetron cavities. We have found good agreement between the theory and the self-consistent two-dimensional (2D) particle-in-cell (PIC) MAGIC simulations. We have predicted vortex structures in the equilibrium relativistic electron flow in magnetrons (Davies, Zhou and Chen, 2007; Davies, Chen and Zhou, 2008). The vortex structures are induced by the periodic corrugations on the magnetron anode. In the analysis, we have made the guide-center approximation, which is validate at low electron densities. We have validated the analysis using test-particle calculations.

1.1 Small-Signal Gain Theory of Non-Relativistic Planar Magnetrons (Zhou and Chen, 2007 and 2008)

The onset of the unstable oscillations in magnetrons has not been analytically described to complete satisfaction, although extensive particle-in-cell (PIC) simulations can make good predictions for the instability characteristics (see, for example, Chan, Chen and Davidson, 1993; Lemke, Genoni and Spencer, 1999). Previous analytical studies included various models utilizing linear theories. Earlier work focused on the diocotron instability in the guiding-center approximation (Davidson, Chan, Chen, et al., 1991; Ayres, Chen, Stark, et al., 1992), which ignores inertial effects in the electron cloud. The recent work by Riyopoulos on the basis of a guiding-center model provided new insight into the magnetron instability in the low-space-charge limit (Riyopoulos, 1998). A linear theory taking a single rf mode in the Floquet expansion was developed to include electromagnetic effects (Kaup, 2001, 2004 and 2007). Despite these theoretical and PIC

simulation efforts, quantitative agreement between theory and PIC simulations has not been reported until our paper (Zhou and Chen, 2007 and 2008).

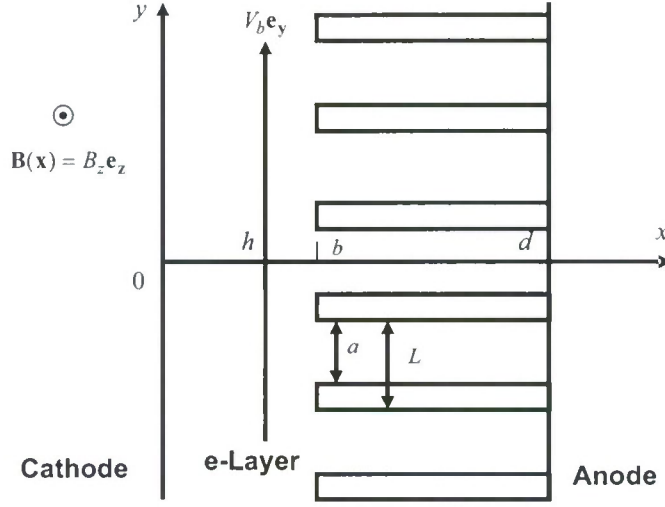


Figure 1.1.1 Schematic of a planar magnetron with a thin electron layer (from Zhou and Chen, 2008).

Assuming a multi-stream thin electron cloud located at a distance of h from the cathode as shown in Fig. 1.1.1, we have obtained the small-signal gain equation or the loaded dispersion relation (Zhou and Chen, 2008)

$$0 = D(\omega, k_z) \equiv \cot\left[\frac{\omega}{c}(d-b)\right] + \frac{\omega ab}{cL} \sum_{q=-\infty}^{\infty} \frac{1}{p_q b} \left| \frac{\sin(k_q a/2)}{k_q a/2} \right|^2 \frac{\cos(p_q b) + \varepsilon_{k_q}(\omega) \cos[p_q(b-h)]}{\sin(p_q b) + \varepsilon_{k_q}(\omega) \sin[p_q(b-h)]} \quad (1.1.1)$$

where

$$\varepsilon_{k_q}(\omega) = \sum_{j=1}^M \frac{p_q}{(\omega - k_q V_{bj})^2} \left(\frac{e^2 \sigma_{bj}}{\varepsilon_0 m} \right) \sin(p_q h) \quad (1.1.2)$$

and $p_q = \sqrt{\omega^2/c^2 - k_q^2}$. For $\varepsilon_{k_q} = 0$, Eq. (1.1.1) is the vacuum dispersion relation for the corrugated structure. For $\varepsilon_{k_q} \neq 0$, on the other hand, Eq. (1.1.1) permits calculations of small-signal gains in magnetrons, which will be discussed in Sec. 1.2.

It should be noted that the simplifying assumption of a thin electron cloud has enabled us to avoid the difficulties in treating multiple poles in the small-signal gain equation in general situation. We plan to further study the general small-signal gain equation.

1.2 Comparison between Small-Signal Gain Theory and Two-Dimensional Particle-in-Cell Simulations (Zhou and Chen, 2008)

To compare our small-signal gain theory with 2D MAGIC simulations, we have restricted to the low-current regime, where the thin-beam equilibrium model is a good approximation to the thin electron cloud in the 2D MAGIC simulations.

As an example, we have considered a system with the parameters: $L = 0.478$ cm, $a = 0.382$ cm, $b = 0.478$ cm, $d = 4.25$ cm, $h = 0.382$ cm, $B_z = 180$ G, $E_x = -5.27$ kV/cm, $\sigma_b = 2.12 \times 10^8$ cm⁻², and $\bar{V}_b = 0.098c$.

First, we have computed the vacuum dispersion relation from Eq. (1.1.1) with $\varepsilon_{k_q} = 0$, and found good agreement with the 2D MAGIC simulation with the absence of the electron cloud, as shown in Fig. 1.2.1.

Second, we have made use of the self-consistent PIC code, 2D MAGIC, to simulate the planar magnetron system. Because 2D MAGIC can handle only a few vane, a 3-vane slow-wave corrugated structure with the same parameters as in Fig. 1.2.1 is used in the simulation. Periodic boundary conditions are used such that the $2\pi/3$ mode is supported by the 3-vane structure. The uniform crossed electric and magnetic fields are applied with $B_z = 180$ G and $E_x = -5.27$ kV/cm. The electron beam is initialized as a slab infinite long in the z direction and with a width of 0.05 cm in the x direction. The electron beam propagates with an initial velocity of $\bar{V}_b = 0.098c$. As the beam propagates, the instability starts to build up which is illustrated by the voltage cross the vane tip of the slow-wave structure. In Fig. 1.2.2, the amplitude of the oscillating voltage filtered by a filter that selects the $2\pi/3$ mode is plotted. In the early stage of the instability (e.g. for $t < 15$ ns), the oscillation has a very small amplitude and exhibits a relatively broad frequency spectrum which is not shown in Fig. 1.2.2. Starting from $t = 10$ ns, the $2\pi/3$ mode grows exponentially. It saturates at about $t = 26$ ns. For this MAGIC simulation, the $2\pi/3$ mode is determined to have a frequency of 1.93 GHz and an amplitude growth rate of 3.12 dB/cm, shown as circle and cross in Fig. 1.2.3, respectively.

Finally, we have solved the loaded dispersion relation in Eq. (1.1.1) with $\varepsilon_{k_q} \neq 0$ to calculate the real frequency and the instability growth rate. Due to the influence of the anode corrugation, the electron cloud velocity prior to the linear growth is observed to vary sinusoidally in the y -direction with small amplitude around the averaged flow velocity in the 2D MAGIC simulation. To model the velocity variation, we have used three electron cloud streams at the same location $x = 0.0384$ cm, each with one third of the total surface charge number $\sigma_{b1} = \sigma_{b2} = \sigma_{b3} = \sigma_b/3$ and a slightly different velocities, i.e., $V_{b1} = 0.98\bar{V}_b$, $V_{b2} = \bar{V}_b$, and $V_{b3} = 1.02\bar{V}_b$. The theoretical growth rate is in good agreement with the 2D MAGIC simulation as shown in Fig. 1.2.3.

1.3 Vortex Structures in Relativistic Magnetrons (Davies, Zhou and Chen, 2007; Davies, Chen and Zhou, 2008)

The periodic corrugations on the anode have a strong influence on the equilibrium flow in magnetrons and crossed-field devices. In particular, we predicted the existence of vortex structures induced by the corrugations on the anode in non-relativistic magnetrons (Chen, 2004; Bhatt and Chen, 2003 and 2004; Davies and Chen, 2006). Until our

prediction, vortex formation had not been discussed in the literature in the context of magnetrons and crossed field devices. In fact, all conventional treatments of the

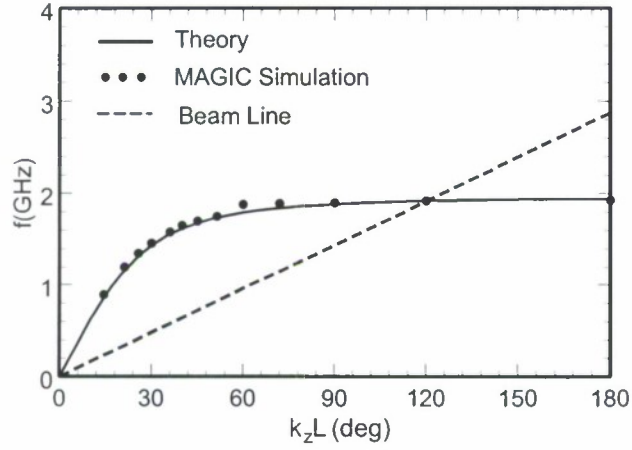


Figure 1.2.1 Vacuum dispersion diagram for a planar magnetron structure obtained from the dispersion relation in Eq. (1.1.1) with $\varepsilon_{k_q} = 0$ (solid curve) and 2D MAGIC simulations (dotted curve). The dashed curve is the beam line $f = k_z / 2\pi \bar{V}_b$. Here, the parameters are $L = 0.478$ cm, $a = 0.382$ cm, $b = 0.478$ cm, $d = 4.25$ cm, and $\bar{V}_b = 0.098c$ (from Zhou and Chen, 2008).

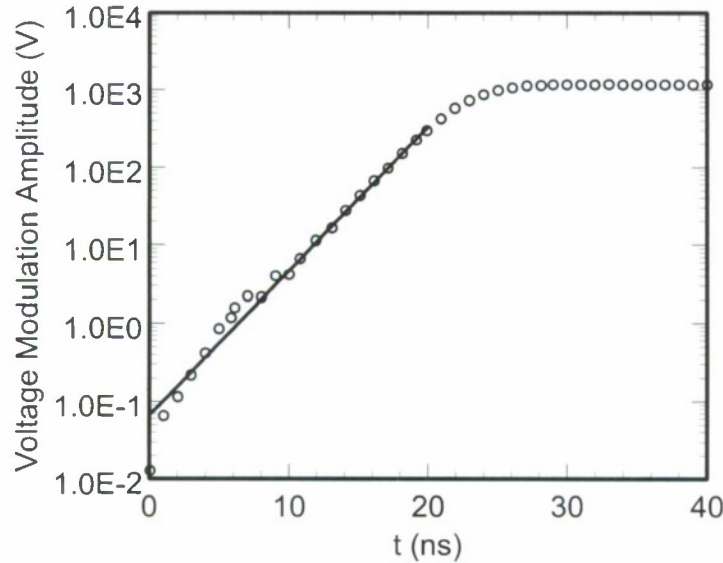


Figure 1.2.2 Plot of the amplitude of oscillating voltage as a function of time as obtained from the MAGIC simulation. Here, the parameters are $L = 0.478$ cm, $a = 0.382$ cm,

$b = 0.478 \text{ cm}$, $d = 4.25 \text{ cm}$, $h = 0.382 \text{ cm}$, $B_z = 180 \text{ G}$, $E_x = -5.27 \text{ kV/cm}$,
 $\sigma_b = 2.12 \times 10^8 \text{ cm}^{-2}$, and $\bar{V}_b = 0.098c$ (from Zhou and Chen, 2008).

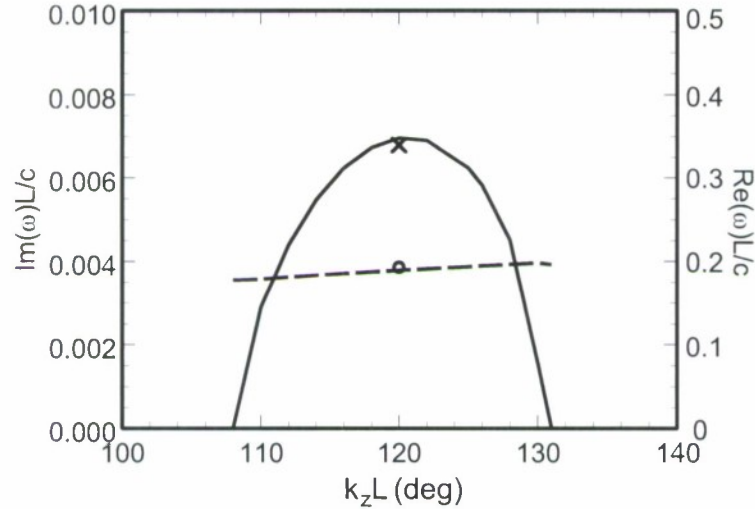


Figure 1.2.3 Plot of the temporal growth rate $\text{Im}(\omega)$ (solid curve) and the real frequency $\text{Re}(\omega)$ (dashed curve) as a function of wave number k_z for the lowest resonant TM mode. The solid and dashed curves are obtained from Eq. (1.1.1) using the three electron cloud streams, whereas the circle and cross are the real frequency and instability growth rate from the MAGIC simulation, respectively. Here, the parameters are $L = 0.478 \text{ cm}$, $a = 0.382 \text{ cm}$, $b = 0.478 \text{ cm}$, $d = 4.25 \text{ cm}$, $h = 0.382 \text{ cm}$, $B_z = 180 \text{ G}$, $E_x = -5.27 \text{ kV/cm}$, $\sigma_{b1} = \sigma_{b2} = \sigma_{b3} = \sigma_b/3 = 7.07 \times 10^7 \text{ cm}^{-2}$, $V_{b1} = 0.98\bar{V}_b$, $V_{b2} = \bar{V}_b = 0.098c$, and $V_{b3} = 1.02\bar{V}_b$ (from Zhou and Chen, 2008).

equilibrium electron flows in magnetrons had ignored effects of the anode corrugations (see, for example, Davidson, Chan, Chen, et al., 1991).

By definition, an equilibrium flow corresponds to a state in magnetrons and crossed-field devices in the absence of rf oscillations. While it is an ideal situation in an actual device, it is of critical importance in order for us to develop a better understanding of magnetrons and crossed-field devices.

Since our report of vortex formation (Chen, 2004) at Magnetron/PIC Simulation Workshop held at AFRL, May 2-3, 2004, several researchers at AFRL (Cartwright, 2007) and elsewhere (Bosman, et al., 2005) have been exploring use of non-axisymmetric cathodes to improve magnetron performance.

Under the auspices of the grant (Chen, 2006), we have established the theory of vortex structures in equilibrium electron flows in relativistic magnetrons (Davies, Zhou and Chen, 2007; Davies, Chen and Zhou, 2008), as a generalization of our earlier work (Davies and Chen, 2006). The theory employs a planar geometry shown in Fig. 1.3.1 and the guiding-center approximation which is valid when the electron plasma frequency is

small compared to the cyclotron frequency. Under the guiding-center approximation, the (nonlinear) equilibrium equations are

$$\nabla^2 \phi(x, y) = 4\pi en(x, y), \quad (1.3.1)$$

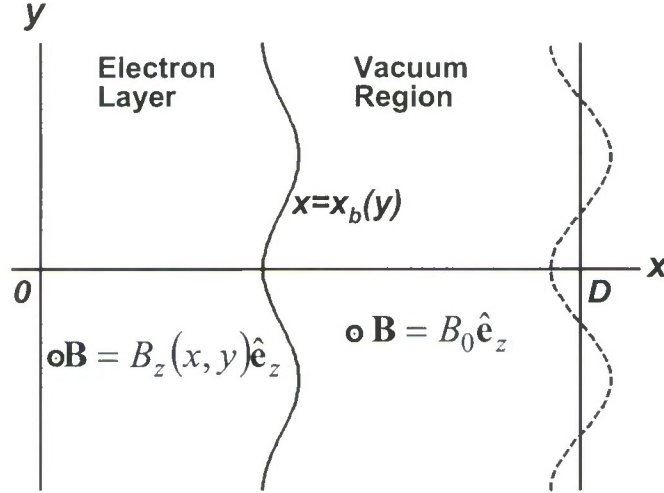


Figure 1.3.1 Electron flow under the influence of anode corrugations in a relativistic planar magnetron. Here, the y axis is the cathode, the curve $x = x_b(y)$ is the electron layer envelope, and the dashed curve is a representative anode (Davies, Zhou and Chen, 2007).

$$\hat{e}_z \times \nabla B_z(x, y) = \frac{4\pi e}{c} n(x, y) \mathbf{V}(x, y), \quad (1.3.2)$$

$$\mathbf{V}(x, y) = \frac{c}{B_z(x, y)} \hat{e}_z \times \nabla \phi(x, y), \quad (1.3.3)$$

where $-e$ is the electron charge, $n(x, y)$ is the electron number density, $\mathbf{V}(x, y)$ is the electron fluid velocity, and $\phi(x, y)$ is the electric potential. The electric field $\mathbf{E}(x, y)$ is given by $\mathbf{E}(x, y) = -\nabla \phi(x, y)$.

For a uniform electron layer, the solutions to the nonlinear equilibrium equations (1.3.1)-(1.3.3) are

$$\phi(x, y) = \begin{cases} -\langle E_x(0, y) \rangle x + 2\pi n_0 e x^2 + \sum_{n=1}^{\infty} F_n (e^{\kappa_n x} - e^{-\kappa_n x}) \cos(\kappa_n y) & (0 < x < x_b) \\ V_0 + C_0(x - D) + V_p e^{-\kappa(x-D)} \cos(\kappa y) + \sum_{n=1}^{\infty} A_n e^{\kappa_n D} (e^{\kappa_n(x-D)} - e^{-\kappa_n(x-D)}) \cos(\kappa_n y) & (x_b < x < x_a) \end{cases} \quad (1.3.4)$$

$$B_z^2(x, y) = \begin{cases} 8\pi e n_0 [\phi(x, y) - \phi(x_b(y), y)] + B_0^2 & (0 < x < x_b) \\ B_0^2 & (x_b < x < x_a) \end{cases} \quad (1.3.5)$$

where the coefficients are given by analytical expressions. One important result is that the solution given in Eqs. (1.3.4) and (1.3.5) supports relativistic vortex structures, as shown in Figs. 1.3.2 and 1.3.3. The other important result is that the constant magnetic field contours coincide with the equipotential contours, as seen in Eq. (1.3.5) and Fig. 1.3.3.

As a numerical example, we have considered a system with the following parameters: $V_0 = 512 \text{ kV}$, $V_p = 49.049 \text{ kV}$, $B_0 = 20 \text{ kG}$, $\langle E_x(0, y) \rangle = 0$, $\kappa = 2\pi / L = \pi \text{ cm}^{-1}$ (corresponding to $L = 2.0 \text{ cm}$), and $D = 0.5 \text{ cm}$. The geometry, magnetic field B_0 , and potential V_0 of this example provide a rectangular approximation to a typical cylindrical L-band relativistic magnetron (see, for example, Lemke, Genoni and Spencer, 1999). Instead of directly specifying a value of n_0 , we have chosen $\omega_p / \omega_c = 1/3$, where $\omega_p = (4\pi m_0 e^2 / m)^{1/2}$ is the nonrelativistic plasma frequency in the electron layer, and $\omega_c = eB_0 / mc$ is the nonrelativistic cyclotron frequency in the vacuum region. From the values of B_0 and ω_p / ω_c specified above, it follows that $n_0 = 4.3200 \times 10^{12}$.

Computed contours of constant potential are shown in Fig. 1.3.2. The cathode at potential $\phi = 0$ is represented by the line $x = 0$. The equipotential contour at 512 kV shown by a dashed curve corresponds to the corrugated conducting anode. The electron-layer boundary is represented by the second dashed curve at 93 kV. The error of $\pm 1 \text{ kV}$ in its potential of $\phi(x_b(y), y) = 93 \text{ kV}$ is due to the neglect of higher order terms than the first in the perturbation calculation.

Also shown in Fig. 1.3.3 are the test particle trajectories which follow the equipotential contours. This is a numerical validation of our vortex theory in equilibrium electron flows of relativistic magnetrons.

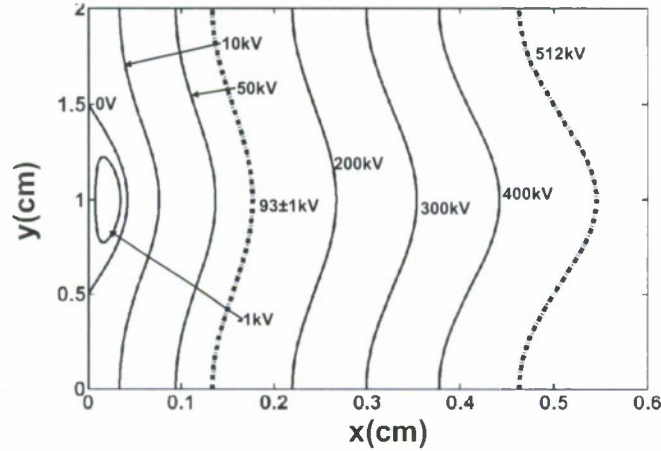


Figure 1.3.2 Contours of constant potential as functions of x and y for a system with parameters $V_0 = 512 \text{ kV}$, $V_p = 49.049 \text{ kV}$, $\kappa = \pi \text{ cm}^{-1}$, $\langle E_x(0, y) \rangle = 0$, $B_0 = 20 \text{ kV}$, $D = 0.5 \text{ cm}$, and $\omega_p / \omega_c = 1/3$. The corrugated anode and the electron-layer boundary

(also contours of constant potential) are depicted by the dashed curves at 93 kV and 512 kV, respectively (from Davies, Chen and Zhou, 2008).

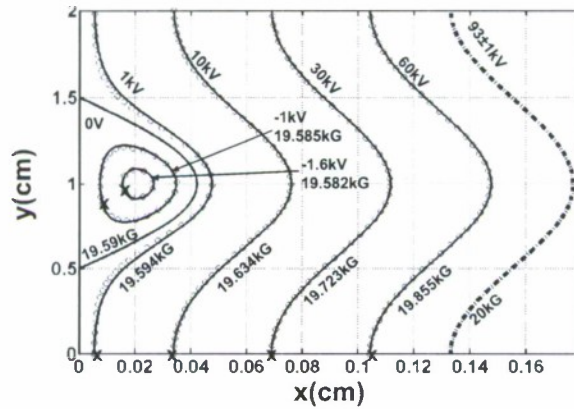


Figure 1.3.3 Detail of the electron-layer region for the system of Fig. 1.3.2. Contours of constant potential are shown by the solid lines with the electron-layer boundary shown by the dashed curve at 93 kV. Because these contours are also lines of constant magnetic field, each contour is labeled with both a value of ϕ and of B_z . Trajectories of test particles, each launched from the point marked with an “x”, are shown by circles (from Davies, Chen and Zhou, 2008).

Our discovery of vortex structures in magnetrons and crossed-field amplifiers provides new insight into a number of areas in magnetron and CFA research, including

- a) Elimination of ion trapping and ion noise,
- b) Elimination of turbulence and noise,
- c) Improvement of magnetron efficiency (Cartwright, 2007), and
- d) Suppression of mode competition (Bosman, et al, 2005).

We plan further investigate them.

2. Discovery of Adiabatic Thermal Beam Equilibrium in a Periodic Solenoidal Magnetic Field (Samokhvalova, Zhou and Chen, 2006, 2007a and 2007b; Zhou, Samokhvalova and Chen, 2006 and 2008; Samokhvalova, 2008)

Many HPM devices such as klystrons and TWTs employ a periodic solenoidal (or permanent) magnetic focusing field. Under the auspices of the present grant (Chen, 2006), we have discovered the thermal equilibrium state of an electron beam as it undergoes adiabatic expansion and compression processes in a periodic or axially varying solenoidal magnetic field. In particular, we have developed paraxial kinetic and warm-fluid equilibrium theories for a thermal electron beam (Samokhvalova, Zhou and Chen, 2006, 2007a and 2007b; Zhou, Samokhvalova and Chen, 2006 and 2008). While our kinetic and warm-fluid beam equilibrium theories are equivalent and applicable to for both the non-

relativistic and relativistic regimes, to our warm-fluid equilibrium theory, our kinetic beam equilibrium theory provides detailed information about the electron distribution in phase space. We have found good agreement between our theories and the recent experimental measurements of the electron density profiles at University of Maryland Electron Ring (UMER) (Bernal, Quinn, Reiser, et al., 2002; Zhou, Samokhvalova and Chen, 2008). Our discovery of the adiabatic thermal beam equilibrium has filled a major gap in the understanding of periodically focused beam equilibria.

2.1 Kinetic Beam Equilibrium Theory (Zhou, Samokhvalova and Chen, 2006 and 2008; Samokhvalova, 2008)

In our kinetic beam equilibrium theory (Zhou, Samokhvalova and Chen, 2006 and 2008; Samokhvalova, 2008), we have considered a thin, continuous, axisymmetric ($\partial/\partial\theta = 0$), single-species charged-particle beam, propagating with constant axial velocity $V_z \hat{\mathbf{e}}_z$ through an applied periodic solenoidal magnetic focusing field. The applied periodic solenoidal focusing field inside the beam can be approximated by

$$\mathbf{B}^{ext}(r, s) = -\frac{1}{2} B'_z(s) r \hat{\mathbf{e}}_r + B_z(s) \hat{\mathbf{e}}_z, \quad (2.1.1)$$

where $s = z$ is the axial coordinate, $r = \sqrt{x^2 + y^2}$ is the radial distance from the beam axis, the prime denotes the derivative with respect to s , and $B_z(s)$ is the axial magnetic field which can be either periodic along the z -axis with periodicity length S or an arbitrary function of s . In the paraxial approximation, $r_{brms} \ll S$ is assumed, where r_{brms} is the rms beam envelope. The transverse kinetic energy of the beam is assumed to be small compared with its axial kinetic energy, i.e., $|V_z| \gg |V_\perp|$, and the Budker parameter of the beam is assumed to be small, i.e., $q^2 N_b / mc^2 \ll \gamma_b^3 \beta_b^2$, where q and m are the particle charge and rest mass, respectively, c is the speed of light in vacuum, $N_b = 2\pi \int_0^\infty dr r n_b(r, s)$ is the number of particles per unit axial length, and γ_b is the relativistic mass factor, which, to leading order, is $\gamma_b = \text{const} = (1 - \beta_b^2)^{-1/2}$ with $\beta_b = V_b / c \cong V_z / c$.

Because the beam is axisymmetric, the canonical angular momentum P_θ is a constant of motion, i.e.,

$$\frac{dP_\theta}{ds} = 0. \quad (2.1.2)$$

After performing a two-step canonical transformation, we have also found that the scaled transverse Hamiltonian for the single-particle motion

$$\bar{E} \equiv w^2(s) \bar{H}_\perp(\bar{x}, \bar{y}, \bar{P}_x, \bar{P}_y, s) \quad (2.1.3)$$

is an approximate invariant (for detailed analyses and definitions of $w(s)$, \bar{H}_\perp , \bar{x} , \bar{P}_x , etc., see Zhou, Samokhvalova and Chen, 2008). We have chosen the beam equilibrium

distribution in the form similar to the Maxwell-Boltzmann distribution (Zhou, Samokhvalova and Chen, 2008; Samokhvalova, 2008)

$$f_b = C \exp[-\beta(\bar{E} - \omega_b \bar{P}_\theta)], \quad (2.1.4)$$

where C , β and ω_b are constants. C is an integration constant, β is related to the beam emittance, and ω_b is the rotation frequency relative to the Larmor frame. The distribution function f_b defined in Eq. (2.1.4) is a Vlasov equilibrium, i.e., $\partial f_b / \partial s = 0$. The kinetic beam equilibrium theory makes the following two important predictions:

1. The thermal beam emittance is a constant.

$$\varepsilon_{th}^2 \equiv \frac{1}{\beta_b^2 c^2} \langle x^2 \rangle \langle (v_x - V_x)^2 \rangle = \frac{k_B T_\perp(s) r_{brms}^2(s)}{2 \gamma_b m \beta_b^2 c^2} = const, \quad (2.1.5)$$

2. The equation of state is adiabatic, i.e., $T_\perp(s) r_{brms}^2(s) = const$.

The rms envelope equation (2.2.4) is (Zhou, Samokhvalova and Chen, 2008)

$$\frac{d^2 r_{brms}(s)}{ds^2} - \frac{\Omega_b(s)}{\beta_b^2 c^2} [\Omega_b(s) + \Omega_c(s)] r_{brms}(s) - \frac{K}{2 r_{brms}(s)} = \frac{4 \varepsilon_{th}^2}{r_{brms}^3(s)}, \quad (2.1.6)$$

where $\Omega_b(s) = \omega_b \varepsilon_T \beta_b c / 2 r_{brms}^2(s) - \Omega_c(s)/2$ and $\Omega_c(s) = q B_z(s) / \gamma_b m c$. The beam density profile is

$$n_b(r, s) = w^{-2}(s) \iint f d\bar{P}_x d\bar{P}_y = \frac{4 \pi C \varepsilon_{th}^2}{r_{brms}^2(s)} \exp \left\{ - \left[\frac{K}{2} + \frac{4 \varepsilon_{th}^2}{r_{brms}^2(s)} \right] \frac{r^2}{4 \varepsilon_{th}^2} - \frac{q}{\gamma_b^2 k_B T_\perp(s)} \phi^{self}(r, s) \right\}, \quad (2.1.7)$$

where the scalar potential for the self-electric field is determined by the Poisson equation

$$\frac{1}{r} \frac{\partial}{\partial r} \left(r \frac{\partial \phi^{self}}{\partial r} \right) = -4 \pi q n_b(r, s). \quad (2.1.8)$$

It should be pointed out that because the derivation of the theory does not assume specific magnetic profile as defined in Eq. (2.1.1) it is valid not only for the periodic solenoid magnetic field but also for an arbitrary varying solenoid magnetic field. Therefore, our results apply for the periodic focusing channel as well as for the matching section between the electron source and the periodic focusing channel, which is important in the design of electron beams for HPM applications and beam experiments such as University of Maryland Electron Ring (Bernal, Quinn, Reiser, et al., 2002).

2.2 Warm-Fluid Beam Equilibrium Theory (Samokhvalova, Zhou and Chen, 2006, 2007a and 2007b; Samokhvalova, 2008)

We have recovered the results of the macroscopic qualities in the kinetic beam equilibrium theory [i.e., Eqs. (2.1.5)-(2.1.8)] by solving the following adiabatic warm-fluid equilibrium equations (Samokhvalova, Zhou and Chen, 2007b; Samokhvalova, 2008)

$$n_b \mathbf{V} \cdot \nabla (\gamma_b m \mathbf{V}) = n_b q \left[-\nabla \phi^{self} + \frac{\mathbf{V}}{c} \times (\mathbf{B}^{ext} + \mathbf{B}^{self}) \right] - \nabla \cdot \tilde{\mathbf{P}}(\mathbf{x}), \quad (2.2.1)$$

$$\nabla \cdot (n_b \mathbf{V}) = 0, \quad (2.2.2)$$

$$\nabla^2 \phi^{self}(r, s) = -4\pi q n_b(r, s), \quad (2.2.3)$$

$$p_{\perp}(r, s) = n_b(r, s) k_B T_{\perp}(s), \quad (2.2.4)$$

$$T_{\perp}(s) r_{brms}^2(s) = const. \quad (2.2.5)$$

The detailed analysis is available in our paper (Samokhvalova, Zhou and Chen, 2007b) and Samokhvalova's doctoral thesis (Samokhvalova, 2008).

2.3 Comparison between Theory and Experiment (Zhou, Samokhvalova and Chen, 2008; Samokhvalova, 2008)

Using our adiabatic thermal beam equilibrium theories, we have replicated the beam density profiles at different axial distances in good agreement with the experimental measurements conducted on the University of Maryland Electron Ring. Our equilibrium theory is applicable to this experiment from the anode aperture to a distance prior to the wave breaking initiated by high order density distribution fluctuations induced by a pressure force at the anode aperture. Wave breaking occurs at about one quarter of plasma wavelength, which is about 30 cm in this example. Our equilibrium theories do not explain the density distribution distortion in the present form, but it is possible to develop a perturbation theory based on the equilibrium in the future.

By solving Eqs. (2.1.6)-(2.1.8), we have calculated the beam transverse density profiles of the UMER 5 keV, 6.5 mA electron beam at three axial distances: $s = 6.4$ cm, 11.2 cm, and 17.2 cm, as shown in solid curves in Fig. 2.3.1. The dashed curves are the equivalent Kapchinskij-Vladimirskij (KV) beam density profiles (Kapchinskij and Vladimirskij, 1959). Compared with the experimental measurements (dotted curves), the calculated beam density profiles are in good agreement. As the beam radius increases, the beam density profile approaches to the KV (uniform) beam density profile, because the beam temperature must decrease in order to keep $T_{\perp}(s) r_{brms}^2(s)$ at a constant. In this adiabatic process, the Debye length $\lambda_D \equiv \sqrt{\gamma_b^2 k_B T_{\perp}(s) / 4\pi q^2 n_b(0, s)} = 0.54$ mm is constant.

3. Design of High-Brightness Circular Electron Beams (Bemis, Bhatt, Chen and Zhou, 2007a and 2007b)

An experimental demonstration of the thermal beam equilibrium over long propagation distances requires a high-brightness circular electron beam which is well matched into a periodic solenoidal magnetic focusing channel. To gain experience in the design of high-brightness electron beams, we have developed, under the auspices of the present grant, a method for the design of a high-brightness non-relativistic circular beam system including a charged-particle emitting diode, a diode aperture, a circular beam tunnel, and a focusing magnetic field that matches the beam from the emitter to the beam tunnel. The applied magnetic field has been determined by balancing the forces throughout the gun and transport sections of the beam system. The method has been validated by three-dimensional simulations.

While the detailed method is described in our paper (Bemis, Bhatt, Chen and Zhou, 2007b) and our US patent application (Chen, Bemis, Bhatt and Zhou, 2007), Figs. 3.1-3.4 summarize the results for a high-perveance electron beam at a voltage of 2.3 kV. This system is scalable to moderately high voltages.

Figure 3.1 shows the final results of an OMNITRAK simulation for a circular electron beam which is emitted from an emitter (cathode) with a radius of 1.52 mm, a current of 0.11 A, a cathode-to-anode distance of 4.11 mm at radius $r = 1.52$ mm. The diode voltage is 2300 V.

Figure 3.2 shows plots of E_r versus z at $r = 1.0$ mm and $B_z(0, z)$ versus z from the OMNITRAK simulation after two iterations. The radial electric field vanishes at the

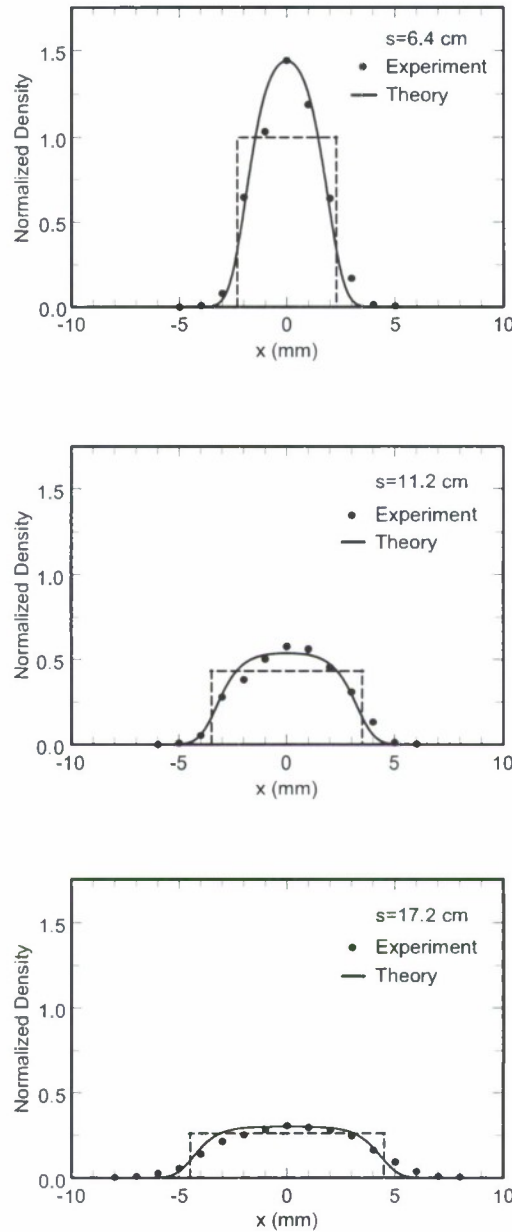


Figure 2.3.1 Normalized beam transverse density profiles of a 5 keV, 6.5 mA ($4\mathcal{E}_{\tilde{x}rms} = 30$ mm-mrad) electron beam at three axial distances: $s = 6.4$ cm, 11.2 cm, and

17.2 cm. The solid curves are from theory, the dotted curves are the experimental measurements, and the dashed lines are the equivalent KV beam density distributions. The densities are normalized to the equivalent KV beam density (from Zhou, Samokhvalova and Chen, 2008).

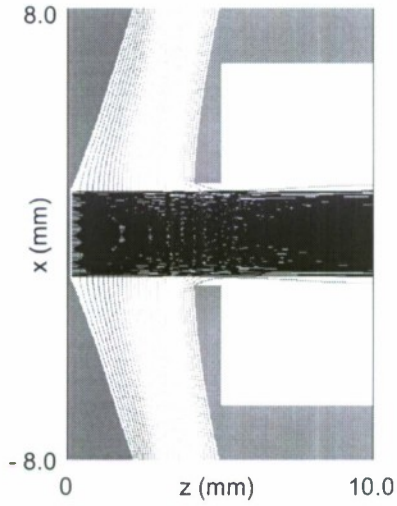


Figure 3.1 OMNITRAK simulation of the dynamics of an electron beam emitted from a flat circular cathode with a radius of 1.52 mm and a current of 0.11 amperes in an optimized magnetic field. Here, the cathode-to-anode distance is 4.11 mm at $r = 1.52$ mm, the circular anode aperture has a radius of 1.8 mm, and the beam tunnel has a radius of 6.0 mm. The diode voltage is 2300 V (from Bemis, Bhatt, Chen and Zhou, 2007b).

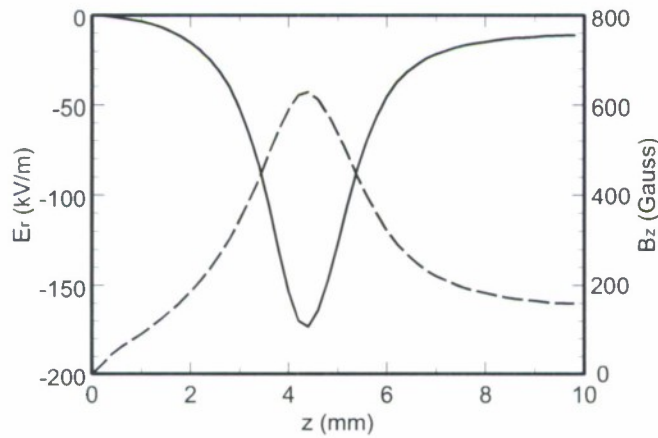


Figure 3.2 Plots of E_r versus z at $r = 1$ mm (solid curve) and $B_z(0, z)$ versus z (dashed curve) from the OMNITRAK simulations after two iterations (from Bemis, Bhatt, Chen and Zhou, 2007b).

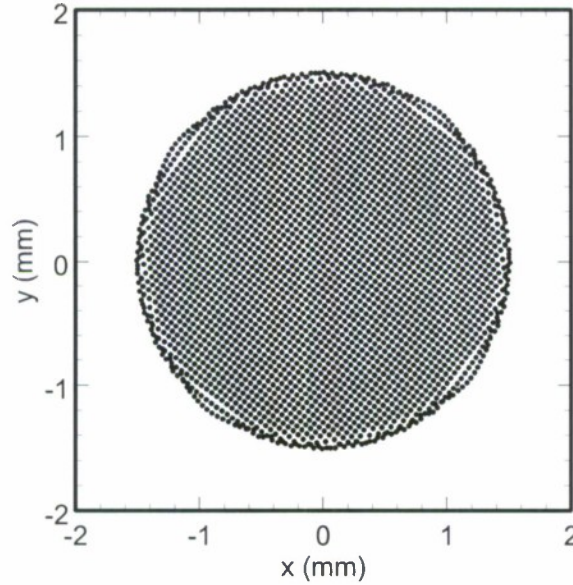


Figure 3.3 Plot of the electron distribution at $z = 8$ mm in the phase plane (x, y) (from Bemis, Bhatt, Chen and Zhou, 2007b).

emitter (i.e., at $z = 0$), achieves a maximum magnitude at $z = 4.11$ mm, and then approaches to a constant value well inside the beam tunnel. The applied axial magnetic field at the emitter vanishes, increases to 640 G at the aperture, and then falls to about 160 G well inside the beam tunnel.

Figure 3.3 shows the electron distribution in the phase plane (x, y) at $z = 8$ mm. The beam distribution maintains transverse uniformity. Indeed, the normalized fourth moment $\langle r^4 \rangle / \langle r^2 \rangle^2$ which is equal to 4/3 for a transversely uniform density distribution, remains 4/3 within $\pm 1\%$. The outer beam radius remains the same as the emitter radius within 1 to 3%. The beam is very bright, and its normalized rms emittance is predicted to be 0.33 mm-mrad, which is 1.15 times the intrinsic normalized rms emittance of 0.33 mm-mrad.

Our design method is limited to a nonrelativistic beam matching into a uniform magnetic field. We plan to extend our design method to include thermal effects and beam matching into periodic solenoidal (permanent) magnetic focusing field. We will also extend our design method to relativistic electron beams in which both relativistic effects and self-magnetic field effects are important.

4. Development of Elliptic Beam Theory for High-Power Microwave Device Applications (Bhatt, 2006; Zhou, 2006; Chen and Zhou, 2007; Zhou, Bhatt and Chen, 2008)

Existing HPM devices employ either a pencil electron beam or an annular electron beam. One of the main objectives in high-power microwave (HPM) research has been to develop innovative science and technology which could lead to improve the efficiency, output power level, and other performance (such as weight reduction) of high-power microwave (HPM) devices. A promising approach is to use a large-aspect-ratio elliptic electron beam rather than the conventional pencil or annular electron beam as the energy source. Compared with a conventional HPM device, a HPM device powered by an elliptic electron beam has the following attractive features:

- a) Power scales as f^{-1} instead of f^{-2} (where f is the frequency), thus more power;
- b) Low effective beam perveance, thus higher efficiency;
- c) Use of permanent magnets for beam focusing, thus lower energy consumption; and
- d) Low cathode loading, thus longer device lifetime.

In order to experimentally demonstrate high-power elliptic electron beams which can be employed in HPM and vacuum electron devices, we must advance our understanding of the generation, compression, focusing and transport of elliptic electron beams.

Building upon our recent work on elliptic electron beam formation (Bhatt and Chen, 2005; Bhatt, Bemis and Chen, 2005 and 2006) and periodically twisting elliptic electron beams (Zhou, Bhatt and Chen, 2006), we have developed a kinetic theory of periodically twisting elliptic beams and both cold-fluid and kinetic theories of non-twisting elliptic electron beams under the auspices of the grant (Chen, 2006).

4.1 Kinetic Equilibrium Theory of Periodically Twisting Elliptic Electron Beams (Zhou, 2006; Zhou and Chen, 2006a and 2006b)

We have developed our kinetic equilibrium theory to examine effects of beam temperature on periodically twisting elliptic electron beam. In the kinetic equilibrium theory (Zhou, 2006; Zhou and Chen, 2006a and 2006b), we have derived a constants of motion analogous to the Courant-Snyder invariant (Courant and Snyder, 1958). We have constructed a Vlasov beam equilibrium distribution of the Kapchinskij-Vladimirskij form using the two constants of motion. We have obtained the generalized envelope equations which include beam temperature effects. In the cold-fluid limit, the generalized envelope equations recover those in the cold-fluid beam equilibrium theory (Zhou, 2006; Zhou, Bhatt and Chen, 2006). Detailed results are available in our paper (Zhou and Chen, 2006b) and Zhou's doctoral thesis (Zhou, 2006).

To illustrate the effects of beam temperature, we have considered a relativistic elliptic beam with $V_b = 198.5$ keV, current $I_b = 85.5$ A, aspect ratio $a/b = 5$, and non-axisymmetric periodic permanent magnet focusing with $B_0 = 2.4$ kG, $S = 2.2$ cm, and $k_{0,y}/k_{0,x} = 1.52$. Such a relativistic elliptic beam could be used in a 10 MW L-Band ribbon-beam klystron (RBK) for the International Linear Collider (ILC).

As shown in Fig. 4.1.1, the solid curves represent the beam semi-axis envelopes and twist angle with zero temperature which is corresponding to a cold beam, while the dotted curves represent the beam envelopes and twist angle with 2.5 keV on-axis temperature. It is evident in Fig. 4.1.1 that the temperature effects on the beam envelopes

and twist angle are negligibly small. Since an actual relativistic elliptic beam in a well designed system will have a temperature which will be considerably less than 2.5 keV,

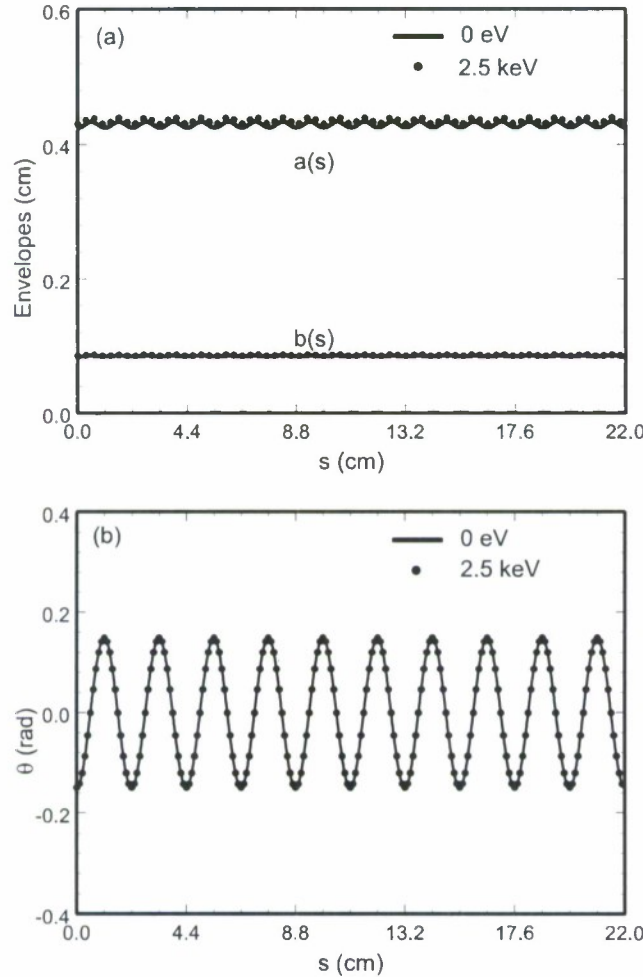


Figure 4.1.1 Plots of (a) envelopes $a(s)$ and $b(s)$ and (b) twist angle $\theta(s)$ versus the axial distance s for the relativistic periodically twisting elliptic electron beam. The solid curves are the generalized envelope solution for a zero-temperature beam, whereas the dotted curves are for a 2.5 keV on-axis temperature beam (from Zhou and Chen, 2006b).

the results in Fig. 4.1.1 implies that the temperature effect on the beam envelopes and twist angle is expected to be negligibly small (Zhou and Chen, 2006b).

4.2 Cold-Fluid Equilibrium Theory of Non-Twisting Elliptic Electron Beams (Bhatt, 2006; Zhou, 2006; Chen and Zhou, 2007; Zhou, Bhatt and Chen, 2008)

For HPM and vacuum electron device applications, non-twisting elliptic electron beams are desirable. Under auspices of the present grant (Chen, 2006), we have

developed a cold-fluid equilibrium theory of a non-twisting elliptic electron beam (Bhatt, 2006; Chen and Zhou, 2007; Zhou, Bhatt and Chen, 2008), which is a generalization of our cold-fluid equilibrium theory of a periodically twisting elliptic electron beam (Zhou, 2006; Zhou, Bhatt and Chen, 2006).

We have used the combination of a periodic non-axisymmetric magnetic field and a quadrupole magnetic field to focus a nearly straight large-aspect-ratio elliptic beam, whose twist angle vanishes approximately. The (nonlinear) cold-fluid equilibrium equations are:

$$\beta_b c \frac{\partial}{\partial s} n_b + \nabla_{\perp} \cdot (n_b \mathbf{V}_{\perp}) = 0, \quad (4.2.1)$$

$$\nabla_{\perp}^2 \phi^s = \beta_b^{-1} \nabla_{\perp}^2 A_z^s = -4\pi q n_b, \quad (4.2.2)$$

$$n_b \left(\beta_b c \frac{\partial}{\partial s} + \mathbf{V}_{\perp} \cdot \nabla_{\perp} \right) \mathbf{V}_{\perp} = \frac{q n_b}{\gamma_b m} \left[-\frac{1}{\gamma_b^2} \nabla_{\perp} \phi^s + \beta_b \hat{\mathbf{e}}_z \times \mathbf{B}_{\perp}^{ext} + \frac{\mathbf{V}_{\perp}}{c} \times B_z^{ext}(s) \hat{\mathbf{e}}_z \right]. \quad (4.2.3)$$

For the beam dimensions small relative to the characteristic scale of magnetic variations, i.e., $(k_{0x}x)^2/6 \ll 1$ and $(k_{0y}y)^2/6 \ll 1$, the combined magnetic field can be described to the lowest order in the transverse dimensions as

$$\mathbf{B}^{ext} = B_z(s) \mathbf{e}_z - \frac{dB_z(s)}{ds} \left[\frac{k_{0x}^2}{k_0^2} x \mathbf{e}_x + \frac{k_{0y}^2}{k_0^2} y \mathbf{e}_y \right] + B_q'(s) [y \mathbf{e}_x + x \mathbf{e}_y], \quad (4.2.4)$$

where $k_0 = 2\pi/S$, $k_{0x}^2 + k_{0y}^2 = k_0^2$, S is the axial periodicity length, and $B_q'(s) \equiv \partial B_x^q / \partial y|_{(s,0,0)} = \partial B_y^q / \partial x|_{(s,0,0)}$.

We seek solutions to Eqs. (2.4.2.1)-(2.4.2.3) of the form

$$n_b(\mathbf{x}_{\perp}, s) = \frac{N_b}{\pi a(s)b(s)} \Theta \left[1 - \frac{\tilde{x}^2}{a^2(s)} - \frac{\tilde{y}^2}{b^2(s)} \right], \quad (4.2.5)$$

$$\mathbf{V}_{\perp}(\mathbf{x}_{\perp}, s) = [\mu_x(s)\tilde{x} - \alpha_x(s)\tilde{y}] \beta_b c \hat{\mathbf{e}}_{\tilde{x}} + [\mu_y(s)\tilde{y} + \alpha_y(s)\tilde{x}] \beta_b c \hat{\mathbf{e}}_{\tilde{y}}. \quad (4.2.6)$$

In Eqs. (4.2.5) and (4.2.6), $\mathbf{x}_{\perp} = \tilde{x} \hat{\mathbf{e}}_{\tilde{x}} + \tilde{y} \hat{\mathbf{e}}_{\tilde{y}}$ is a transverse displacement in the twisted coordinate system; $\theta(s)$ is the twist angle of the ellipse; $\Theta(x) = 1$ if $x > 0$ and $\Theta(x) = 0$ if $x < 0$; and the functions $a(s)$, $b(s)$, $\mu_x(s)$, $\mu_y(s)$, $\alpha_x(s)$, $\alpha_y(s)$ and $\theta(s)$ are to be determined self-consistently [see Eqs. (4.2.8)-(4.2.12)]. The self-electric and self-magnetic fields are well known for an elliptical beam with density distribution specified in Eq. (4.2.5), i.e.,

$$\phi^s = \beta_b^{-1} A_z^s = -\frac{2qN_b}{a+b} \left(\frac{\tilde{x}^2}{a} + \frac{\tilde{y}^2}{b} \right). \quad (4.2.7)$$

Using the expressions in Eqs. (4.2.4)-(4.2.7), we have shown that both the equilibrium continuity equation (4.2.1) and force equation (4.2.3) are satisfied if the dynamical variables $a(s)$, $b(s)$, $\mu_x(s) \equiv a^{-1} da/ds$, $\mu_y(s) \equiv b^{-1} db/ds$, $\alpha_x(s)$, $\alpha_y(s)$ and $\theta(s)$ obey the (cold-fluid) generalized beam envelope equations (Chen and Zhou, 2007; Zhou, Bhatt and Chen, 2008)

$$\begin{aligned} \frac{d^2 a}{ds^2} - \frac{b^2(\alpha_x^2 - 2\alpha_x\alpha_y) + a^2\alpha_y^2}{a^2 - b^2} a - \frac{2K}{(a+b)} - 2\sqrt{\kappa_z(s)}\alpha_y a \\ + \left[\frac{k_{0x}^2 - k_{0y}^2}{k_0^2} \frac{d\sqrt{\kappa_z(s)}}{ds} \sin(2\theta) + \kappa_q(s)\cos(2\theta) \right] a = 0, \end{aligned} \quad (4.2.8)$$

$$\begin{aligned} \frac{d^2 b}{ds^2} + \frac{a^2(\alpha_y^2 - 2\alpha_x\alpha_y) + b^2\alpha_x^2}{a^2 - b^2} b - \frac{2K}{(a+b)} - 2\sqrt{\kappa_z(s)}\alpha_x b \\ - \left[\frac{k_{0x}^2 - k_{0y}^2}{k_0^2} \frac{d\sqrt{\kappa_z(s)}}{ds} \sin(2\theta) + \kappa_q(s)\cos(2\theta) \right] b = 0, \end{aligned} \quad (4.2.9)$$

$$\begin{aligned} \frac{d}{ds}(a^2\alpha_y) - \frac{ab^3(\alpha_x - \alpha_y)}{a^2 - b^2} \frac{d}{ds}\left(\frac{a}{b}\right) + 2a'a\sqrt{\kappa_z(s)} \\ + a^2 \left[2 \frac{k_{0x}^2 \cos^2 \theta + k_{0y}^2 \sin^2 \theta}{k_0^2} \frac{d\sqrt{\kappa_z(s)}}{ds} - \kappa_q(s)\sin(2\theta) \right] = 0, \end{aligned} \quad (4.2.10)$$

$$\begin{aligned} \frac{d}{ds}(b^2\alpha_x) - \frac{a^3b(\alpha_x - \alpha_y)}{a^2 - b^2} \frac{d}{ds}\left(\frac{b}{a}\right) + 2b'b\sqrt{\kappa_z(s)} \\ + b^2 \left[2 \frac{k_{0x}^2 \sin^2 \theta + k_{0y}^2 \cos^2 \theta}{k_0^2} \frac{d\sqrt{\kappa_z(s)}}{ds} + \kappa_q(s)\sin(2\theta) \right] = 0, \end{aligned} \quad (4.2.11)$$

$$\frac{d\theta}{ds} = \frac{a^2\alpha_y - b^2\alpha_x}{a^2 - b^2}, \quad (4.2.12)$$

where

$$\sqrt{\kappa_z(s)} \equiv \frac{qB_z(s)}{2\gamma_b\beta_b mc^2}, \quad \kappa_q(s) \equiv \frac{qB'_q(s)}{\gamma_b\beta_b mc^2} \quad \text{and} \quad K \equiv \frac{2q^2 N_b}{\gamma_b^3 \beta_b^2 mc^2}. \quad (4.2.13)$$

Equations (4.2.8)-(4.2.12) support non-twisting elliptic electron beam solutions in the non-relativistic regime which is of interest to vacuum electron device applications, as well as in the relativistic regimes which is of interest to HPM applications.

4.3 Kinetic Equilibrium Theory of Non-Twisting Elliptic Electron Beams (Bhatt, 2006; Chen and Zhou, 2007; Zhou, Bhatt and Chen, 2008)

We have developed our kinetic equilibrium theory to examine effects of beam temperature on non-twisting elliptic electron beam. In the kinetic equilibrium theory (Bhatt, 2006; Zhou, Bhatt and Chen, 2008), we have derived a constants of motion analogous to the Courant-Snyder invariant (Courant and Snyder, 1958). We have constructed a Vlasov beam equilibrium distribution of the Kapchinskij-Vladimirskij form using the constant of motion. We have obtained the (kinetic) generalized envelope equations which include beam temperature effects. In the cold-fluid limit, the (kinetic) generalized envelope equations recover the cold-fluid ones (Chen and Zhou, 2007; Zhou,

Bhatt and Chen, 2008). Detailed results are available in our paper (Zhou, Bhatt and Chen, 2008) and Bhatt's doctoral thesis (Bhatt, 2006).

4.4 Application and Simulation Validation of Cold-Fluid and Kinetic Equilibrium Theories (Bhatt, 2006; Chen and Zhou, 2007; Zhou, Bhatt and Chen, 2008)

As an example, we have considered a relativistic elliptic beam that can be used in a 10 MW L-Band ribbon-beam klystron (RBK) for the International Linear Collider (ILC). The beam has a current of $I_b = 111.1$ A, a voltage of $V_b = 120$ kV and an aspect ratio of 20:1. Solving the (cold-fluid) generalized envelope equations (4.2.8)-(4.2.12), the hybrid magnetic fields are determined to be the form of Eq. (4.2.4) with $B_z(s) = -2000 \sin(k_0 s)$ G, $B'_q = 80.8$ G/cm, $S = 2.2$ cm, and $k_{0y}/k_{0x} = 20$. In Fig. 4.4.1, the solid curves are the beam semi-axes $a(s)$ and $b(s)$ calculated from the (cold-fluid) generalized envelope equations, whereas dotted curves are from the self-consistent PIC PFB2D simulation. The twist angle vanishes, i.e., $\theta(s) = 0$, in this example.

To study the temperature effects in the 111.1 A and 120 kV elliptic electron beam, we have solved the (kinetic) generalized envelope equations with nonzero initial thermal emittances, i.e., $\varepsilon_{th,x}^2 = k_B T a^2(s=0) / m \gamma_b \beta_b^2 c^2$ and $\varepsilon_{th,y}^2 = k_B T b^2(s=0) / m \gamma_b \beta_b^2 c^2$. As shown in Fig. 4.4.2, the elliptic beam envelopes are calculated for three different temperature choices: 0 eV, 50 eV and 100 eV. Compared with the cold beam envelopes shown as solid curves in Fig. 4.4.1, the warm beam envelopes are found to increase slightly as the beam temperature increases, while the aspect ratio of the beam decreases from 20:1 to 16.4:1 as the beam temperature increases from 0 eV to 100 eV.

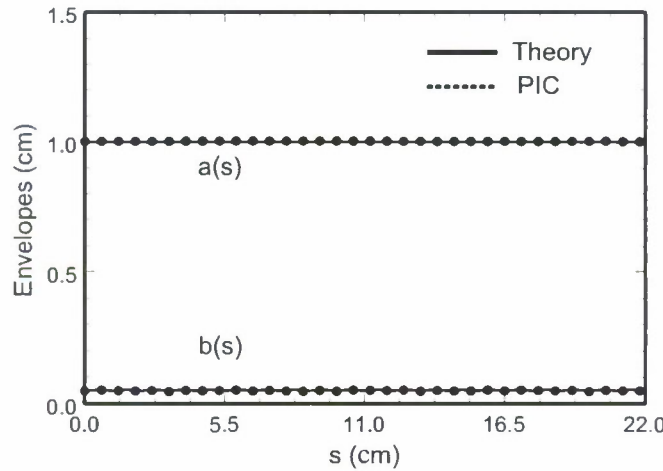


Figure 4.4.1 Plots of the beam envelopes $a(s)$ and $b(s)$ versus the axial distance s for the 111.1 A, 120 kV relativistic elliptic electron beam with zero temperature. The solid curves are the (cold-fluid) generalized envelope solution, whereas the dotted curves are from the PFB2D simulation (from Zhou, Bhatt and Chen, 2008).

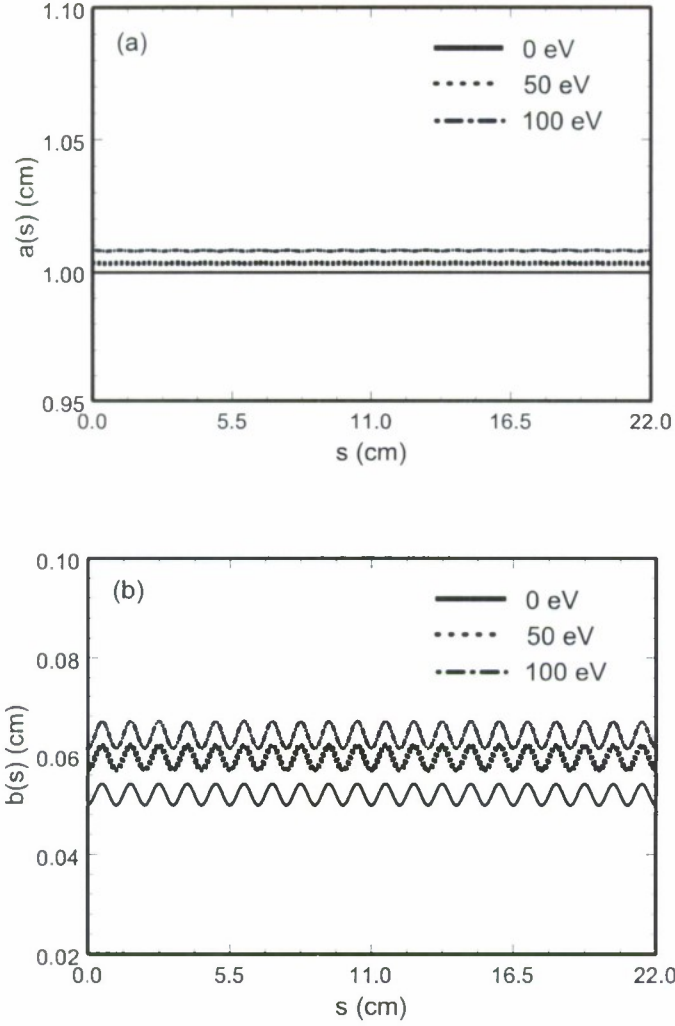


Figure 4.4.2 Plots of the beam envelopes (a) $a(s)$ and (b) $b(s)$ versus the axial distance s for the 111.1 A, 120 kV relativistic elliptic electron beam for three different temperature choices: 0 eV, 50 eV and 100 eV (from Zhou, Bhatt and Chen, 2008).

For a practical HPM device, we have assumed that the elliptic beam is generated from an electron gun with an intrinsic temperature of 0.1 eV and a current density of 1.5 A/cm. The elliptic beam has to be compressed by a factor of 471.5 in area to achieve a current density of 707.3 A/cm² in the focusing channel. During the compression, the temperature increases by a factor of 471.5 to 47.2 eV. Therefore, in our calculations, a temperature of 50 eV is a reasonable assumption. As shown in Fig. 4.4.3, the envelopes of the elliptic beam with a temperature of 50 eV are obtained by solving the (kinetic) generalized envelope equations (solid curves) and by the PFB2D PIC simulations (dotted curves). Both results showed a slight increase in the two envelope dimensions and the aspect ratio of the elliptic beam decreases to 17.8, compared with the cold elliptic beam.

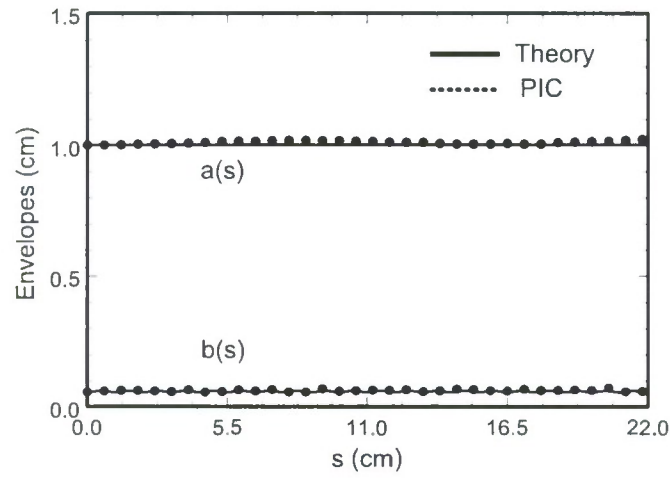


Figure 4.4.3 Plots of the beam envelopes $a(s)$ and $b(s)$ versus the axial distance s for the 111.1 A, 120 kV relativistic elliptic electron beam for a temepature of 50 eV. The solid curves are the (kinetic) generalized envelope solution, whereas the dotted curves are from the PFB2D simulation (from Zhou, Bhatt and Chen, 2008).

5. References

- Ayres, V. M., H. C. Chen, R. A. Stark, H.S.Uhm, and H. E. Brandt, 1992, Phys. Fluids **B4**, 3396.
- Bemis, T., R. Bhatt, C. Chen and J. Zhou, 2007a, "An Ideal Circular Charged-Particle Beam System," Proc. 2007 Part. Accel. Conf., p. 2999.
- Bemis, T., R. Bhatt, C. Chen and J. Zhou, 2007b, "A High-Brightness Circular Charged-Particle Beam System," Appl. Phys. Lett. **91**, 201504.
- Bernal, S., B. Quinn, M. Reiser, P.G. O'Shea, 2002, Phys. Rev. Special Topics – Accel. Beams **5**, 064202;
- Bhatt, R.J., 2006, *Inverse Problems in Elliptic Charged-Particle Beams*, Ph.D. Thesis, Massachusetts Institute of Technology.
- Bhatt, R. and C. Chen, 2003, "Laminar electron flow solutions for two-dimensional electrode geometries," American Physical Society, Bulletin **48**, 314.
- Bhatt, R. and C. Chen, 2005, "Theory and Simulation of Non-Relativistic Elliptic Beam Formation with Child-Langmuir Flow Characteristics," Phys. Rev. ST Accel. Beams **8**, 014201.
- Bhatt, R., T. Bemis, and C. Chen, 2005, "Three-Dimensional Theory and Simulation of Large-Aspect-Ratio Ellipse-Shaped Charged-Particle Beam Gun," Proc. 2005 Part. Accel. Conf. p. 3372 (**First Prize for Outstanding Technical Paper by a Student**).
- Bhatt, R., T. Bemis, and C. Chen, 2006, "Theory and Simulation of Non-Relativistic Elliptic Electron and Ion Beam Generation," (**Invited Paper**) IEEE Trans. Plasma Sci. **34**, 187 (2006).
- Bosman, H.L., et al., 2005, American Physical Society, Bulletin **50**, 72.
- Cartwright, K.L., 2007, private communication.
- Chan, H.-W., C. Chen, and R. C. Davidson, 1993, J. Appl. Phys. **73**, 7053.
- Chen, C., 2004, "Analytic results on high-power microwave devices," presented at AFRL Magnetron/PIC Simulation Workshop, May 2-3.
- Chen, C., 2006, "Coherent structures and chaos control in high-power microwave and particle beam devices," Research proposal funded by AFOSR under Grant No. FA9550-06-1-0269, Chipping Chen, Principal Investigator; and references therein. Lemke, R. W., T. C. Genoni, and T. A. Spencer, 1999, Phys. Plasmas **6**, 603.
- Chen, C., T.M. Bemis, R.J. Bhatt, and J. Zhou, 2007, "Generation, acceleration, focusing and collection of a high-brightness, space-charge-dominated charged-particle beam," US Patent Application No. 11/954,495, November 15.
- Chen, C., and J. Zhou, 2007, "Equilibrium Theory of an Intense Elliptic Beam for High-Power Ribbon-Beam Klystron Applications," Proc. 2007 Part. Accel. Conf. p. 2316.
- Courant, E.D., and H.S. Snyder, 1958, Ann. Phys. (N.Y.) **3**, 1.
- Davidson, R. C., H. W. Chan, C. Chen, and S. Lund, 1991, Rev. Mod. Phys. **63**, 341.
- Davies, J.A., and C. Chen, 2006, "Vertex Structure in a High Density ExB Equilibrium Flow," J. A. Davies and C. Chen, Phys. Plasmas **13**, 012310.
- Davies, J.A., J. Zhou, and C. Chen, 2007, "Vortex structures in relativistic magnetrons," Bulletin of American Physical Society **52**, No. 16, p. 294.
- Davies, J.A., C. Chen, and J. Zhou, 2008, "Vortex structures in relativistic magnetrons," manuscript in preparation.

- Kapchinskij, I. M., and V. V. Vladimirskij, 1959, in *Proceedings of the Conference on High Energy Accelerators and Instrumentation* (CERN, Geneva), p. 274.
- Kaup, D.J., 2001, *Phys Plasmas* **8**, 2473.
- Kaup, D.J., 2004, *Phys. Plasmas* **11**, 3164.
- Kaup, D.J., 2007, "RF modes in the saturation stage of a magnetron," *Bulletin of American Physical Society* **52**, No 16, p. 294.
- Lemke, R.W., T.C. Genoni, and T.A. Spencer, 1999, *Phys. Plasmas* **6**, 603.
- Riyopoulos, S., 1998, *Phys. Rev. Lett.* **81**, 3026.
- Samokhvalova, K.R., 2008, *Thermal Equilibrium Theory of Periodically Focused Charged-Particle Beams*, Ph.D. Thesis, Massachusetts Institute of Technology.
- Samokhvalova, K.R., J. Zhou and C. Chen, 2006, "Warm-Fluid Equilibrium Theory of a Charged Particle Beam in a Periodic Solenoidal Focusing Field," *Advanced Accelerator Concepts*, AIP Conf. Proc. **877**, 445.
- Samokhvalova, K.R., J. Zhou, and C. Chen, 2007a, "Warm-Fluid Equilibrium Theory of an Intense Charged-Particle Propagating Beam in a Periodic Solenoidal Focusing Channel," *Proc. 2007 Part. Accel. Conf.*, p. 3558.
- Samokhvalova, K.R., J. Zhou, and C. Chen, 2007b, "Warm-Fluid Equilibrium Theory for a Thermal Charged-Particle Beam in a Periodic Solenoidal Focusing Field," *Phys. Plasmas* **14**, 103102.
- Zhou, J., 2006, *Transport of Elliptic Intense Charged-Particle Beams*, Ph.D Thesis, Massachusetts Institute of Technology.
- Zhou, J., R. Bhatt, and C. Chen, 2006, "Cold-Fluid Theory of Equilibrium and Stability of a High-Intensity Periodically Twisted Ellipse-Shaped Charged-Particle Beam," *Phys. Rev. Special Topics – Accel. Beams* **9**, 034401.
- Zhou, J., and C. Chen, 2006a, "Vlasov Equilibrium of A Periodically Twisted Ellipse-Shaped Charged-Particle Beam in a Non-Axisymmetric Periodic Magnetic Field," *Proc. 2006 European Part. Accel. Conf.*, p. 2826.
- Zhou, J., and C. Chen, 2006b, "Kinetic Equilibrium of a Periodically Twisted Ellipse-Shaped Charged-Particle Beam," *Phys. Rev. Special Topics – Accel. Beams* **9**, 104201.
- Zhou, J., and C. Chen, 2007, "Small-signal gain theory of a planar magnetron," *Bulletin of American Physical Society* **52**, No. 16, p. 294.
- Zhou, J., and C. Chen, 2008, "Small-signal gain theory of a non-relativistic planar magnetron," *Appl. Phys. Lett.* **93**, 151502.
- Zhou, J., K.R. Samokhvalova, and C. Chen, 2006, "Thermal Rigid-Rotor Equilibrium of Intense Beam Propagation through a Periodic Solenoidal Focusing Field," *Advanced Accelerator Concepts*, AIP Conf. Proc. **877**, 489.
- Zhou, J., K.R. Samokhvalova, and C. Chen, 2008, "Adiabatic Thermal Equilibrium for Periodically Focused Axisymmetric Intense Beam Propagation," *Phys. Plasmas* **15**, 023102.
- Zhou, J., R. Bhatt, C. Chen, 2008, "Periodic focusing of a high-space-charge elliptic charged-particle beam," *Phys. Rev. Special Topics – Accel. Beams* (submitted for publication).

Compendium of Publications
AROSR Grant Number FA9550-06-1-0269
Principal Investigator: Chipping Chen
Program Manager: Dr. Arje Nachman
Directorate: Physics and Electronics

Referred Journals (included):

1. "Kinetic Equilibrium of a Periodically Twisted Ellipse-Shaped Charged-Particle Beam," J. Zhou and C. Chen, *Physical Review Special Topics – Accelerators and Beams* **9**, 104201 (2006).
2. "A High-Brightness Circular Charged-Particle Beam System," T. Bemis, R. Bhatt, C. Chen, and J. Zhou, *Applied Physics Letters* **91**, 201504 (2007).
3. "Warm-Fluid Equilibrium Theory for a Thermal Charged-Particle Beam in a Periodic Solenoidal Focusing Field," K.R. Samokhvalova, J. Zhou and C. Chen, *Physics of Plasmas* **14**, 103102 (2007).
4. "Adiabatic Thermal Equilibrium for Periodically Focused Axisymmetric Intense Beam Propagation," J. Zhou, K.R. Samokhvalova, and C. Chen, *Physics of Plasmas* **15**, 023102 (2008).
5. "Small-Signal Gain Theory of a Non-Relativistic Planar Magnetron," J. Zhou and C. Chen, *Applied Physics Letters* **93**, 151502 (2008).
6. "Periodic focusing of a high-space-charge elliptic charged-particle beam," J. Zhou, R. Bhatt, C. Chen, *Special Topics – Accelerators and Beams*, submitted for publication (2008).

Patent (included):

1. "Non-axisymmetric charged-particle beam system," R.J. Bhatt, C. Chen, and J. Zhou, US Patent No. 7,381,967, June 3, 2008.

Conference Proceedings (not included):

1. "Vlasov Equilibrium of A Periodically Twisted Ellipse-Shaped Charged-Particle Beam in a Non-Axisymmetric Periodic Magnetic Field," J. Zhou and C. Chen, *Proc. 2006 European Part. Accel. Conf.* (2006), p. 2826.
2. "Thermal Rigid-Rotor Equilibrium of Intense Beam Propagation through a Periodic Solenoidal Focusing Field," J. Zhou, K., Samokhvalova, and C. Chen, *Advanced Accelerator Concepts, AIP Conf. Proc.* **877**, 489 (2006).
3. "Warm-Fluid Equilibrium Theory of a Charged Particle Beam in a Periodic Solenoidal Focusing Field," K. Samokhvalova, J. Zhou, and C. Chen, *Advanced Accelerator Concepts, AIP Conf. Proc.* **877**, 445 (2006).
4. "Edge-Emittance Growth and Particle Diffusion Induced by Numerical Discrete-Particle Effects in Self-Consistent Intense Beam Simulations," J. Zhou, C. Chen and R. Pakter, *Advanced Accelerator Concepts, AIP Conf. Proc.* **877**, 248 (2006).
5. "Equilibrium Theory of an Intense Elliptic Beam for High-Power Ribbon-Beam Klystron Applications," C. Chen and J. Zhou, *Proc. 2007 Part. Accel. Conf.* (2007), p. 2316.
6. "An Ideal Circular Charged-Particle Beam System," T. Bemis, R. Bhatt, C. Chen and J. Zhou, *Proc. 2007 Part. Accel. Conf.* (2007), p. 2999.

7. "Warm-Fluid Equilibrium Theory of an Intense Charged-Particle Propagating Beam in a Periodic Solenoidal Focusing Channel," K. Samokhvalova, J. Zhou and C. Chen, Proc. 2007 Part. Accel. Conf. (2007), p. 3558.

Kinetic equilibrium of a periodically twisted ellipse-shaped charged-particle beam

Jing Zhou and Chiping Chen

Intense Beam Theoretical Research Group, Plasma Science and Fusion Center, Massachusetts Institute of Technology, Cambridge, Massachusetts 02139, USA

(Received 26 July 2006; published 26 October 2006)

A Vlasov equilibrium of the Kapchinskij-Vladimirskij form is obtained for a periodically twisted ellipse-shaped charged-particle beam in a nonaxisymmetric periodic magnetic focusing field. The single-particle Hamiltonian dynamics is analyzed self-consistently. A constant of motion analogous to the Courant-Snyder invariant is found. The equilibrium distribution function is constructed. The statistical properties of the beam equilibrium are studied. In the zero-temperature limit, the generalized envelope equations derived from the kinetic equilibrium theory recover the generalized envelope equations obtained in the cold-fluid equilibrium theory. Examples of periodically twisted elliptic beam equilibria are presented, and potential applications are discussed. For ribbon-beam amplifier and ribbon-beam klystron applications, the kinetic equilibrium theory predicts that the effect of beam temperature on the beam envelopes is negligibly small.

DOI: 10.1103/PhysRevSTAB.9.104201

PACS numbers: 29.27.-a, 52.59.Sa, 41.75.-i, 52.25.Dg

I. INTRODUCTION

A fundamental understanding of the kinetic equilibrium and stability properties of high-intensity electron and ion beams in periodic focusing fields is desirable in the design and operation of particle accelerators [1–14], such as storage rings and rf and induction linacs, as well as vacuum electron devices, such as klystrons and traveling-wave tubes with periodic permanent magnet (PPM) focusing. There are two well-known equilibria for periodically focused intense beams, including the Kapchinskij-Vladimirskij (KV) equilibrium [7–9] in an alternating-gradient quadrupole magnetic focusing field and the periodically focused rigid-rotor Vlasov equilibrium [10,11] in a periodic solenoid magnetic focusing field. In general, for linear focusing forces, self-consistent beam distributions can be formally constructed using a matrix formulation [12,13].

It was shown formally in Ref. [12] that self-consistent beam distributions can be obtained that allow elliptical space-charge beams of arbitrary aspect ratio and with arbitrary rotation angle of the ellipse as long as the field is linear. However, obtaining concrete equilibria with non-upright ellipses is nontrivial. The previous explicitly known Vlasov equilibria of KV form [7,9–11] for high-intensity, space-charge-dominated charged-particle beams propagating in the alternating-gradient quadrupole magnetic focusing field and the periodic solenoid magnetic focusing field charged-particle beams are circular on average; that is, the averages of the beam envelopes in different transverse directions over one period are the same.

There is considerable interest in the research and development of high-intensity charged-particle beams with a large aspect ratio transverse to the direction of propagation. First, large-aspect-ratio elliptic beams (or ribbon beams) can transport larger amounts of beam currents at reduced

intrinsic space-charge forces and energies. Second, they couple efficiently to planar or rectangular rf structures. The combination of the space-charge reduction and efficient coupling allows efficient rf generation in vacuum electronic devices, and efficient acceleration in particle accelerators. Third, elliptic beams provide an additional adjustable parameter (e.g., the aspect ratio) which may be useful for better matching a beam into a periodic focusing channel [14].

One important application of ribbon beams is in the development of advanced radiation devices such as ribbon-beam amplifiers (RBAs) and ribbon-beam klystrons (RBKs), which have advantages over the corresponding conventional (circular-beam) devices in terms of efficiency and operational parameters. Other applications include the development of advanced accelerators capable of generating nonconventional beams, e.g., a planar radio-frequency (rf) linac producing ribbonlike bunches of charged particles.

Although sheet beams have been discussed in the literature for four decades, the Vlasov equilibrium of a high-intensity, space-charge-dominated beam with a large-aspect-ratio elliptic cross section has not been discovered until this paper. Sturrock [15] first suggested use of a periodic magnetic focusing consisting of an array of planar-wiggler magnets for rectilinear beams. Zhang *et al.* [16] had some modest success in the experimental demonstration of the transport of a low-intensity (10 A, 500 kV) sheet beam in a planar-wiggler magnetic field, and observed considerable beam loss. Researchers made use of the multiple-time-scale analysis and the paraxial approximations to obtain the smooth-beam approximation of high-intensity sheet beam equilibria [17,18]. Recently, Russell *et al.* demonstrated the transformation of a circular beam into a sheet beam using asymmetric lenses [19]. The authors discovered a cold-fluid equilibrium for a high-

intensity periodically twisted elliptic beam in a nonaxisymmetric periodic magnetic focusing field [6].

In this paper, it is shown that there exists a Vlasov equilibrium for a periodically twisted large-aspect-ratio intense charged-particle beam with uniform density in the transverse plane propagating through a nonaxisymmetric periodic magnetic focusing field. The single-particle Hamiltonian of such a periodically twisted large-aspect-ratio elliptic beam is investigated. The constant of motion analogous to the Courant-Snyder invariant [20] is found. The equilibrium beam distribution is constructed. The beam envelope equations and flow velocity equations are derived. In the zero-temperature limit, they are consistent with the generalized envelope equations derived from cold-fluid equilibrium theory [6]. Statistical properties and possible applications of the present beam equilibrium are discussed.

II. VLASOV EQUILIBRIUM THEORY

We consider an ellipse-shaped, continuous, intense charged-particle beam propagating with constant axial velocity $\beta_b c \mathbf{e}_z$ through an applied nonaxisymmetric periodic magnetic focusing field. The applied nonaxisymmetric periodic magnetic focusing field inside the thin beam can be approximated by

$$\mathbf{B}^{\text{ext}} \cong -B_0 \sin(k_0 s) \mathbf{e}_z + B_0 \cos(k_0 s) \left[\frac{k_{0x}^2}{k_0} x \mathbf{e}_x + \frac{k_{0y}^2}{k_0} y \mathbf{e}_y \right], \quad (1)$$

where $s = z$ is the axial coordinate, $k_0 = 2\pi/S$, $k_{0x}^2 + k_{0y}^2 = k_0^2$, and S is the axial periodicity length. The 3D magnetic field in Eq. (4) is fully specified by the three parameters B_0 , S , and k_{0x}/k_{0y} . The associated magnetic vector potential can be expressed as

$$\mathbf{A}^{\text{ext}} = -B_0 \sin(k_0 s) \left[-\frac{k_{0y}^2}{k_0^2} y \mathbf{e}_x + \frac{k_{0x}^2}{k_0^2} x \mathbf{e}_y \right]. \quad (2)$$

To determine the self-electric and self-magnetic fields of the beam self-consistently in the present paraxial approximation, we assume that the density profile of the beam is uniform inside the beam boundary, i.e.,

$$n_b(x, y) = \frac{N_b}{\pi a(s)b(s)} \Theta \left(1 - \frac{\tilde{x}^2}{a^2(s)} - \frac{\tilde{y}^2}{b^2(s)} \right). \quad (3)$$

In Eq. (3), $\tilde{x} = x \cos[\theta(s)] + y \sin[\theta(s)]$ and $\tilde{y} = -x \sin[\theta(s)] + y \cos[\theta(s)]$ represent the twisted coordinate as illustrated in Fig. 1; $\theta(s)$ is the twist angle of the ellipse; $\Theta(x) = 1$ if $x > 0$ and $\Theta(x) = 0$ if $x < 0$. The density of the elliptic beam with semimajor axis $a(s) = a(s + S)$ and semiminor axis $b(s) = b(s + S)$ is uniform in the beam interior ($\tilde{x}^2/a^2 + \tilde{y}^2/b^2 \leq 1$). The semimajor and semiminor axes have the same periodicity as the

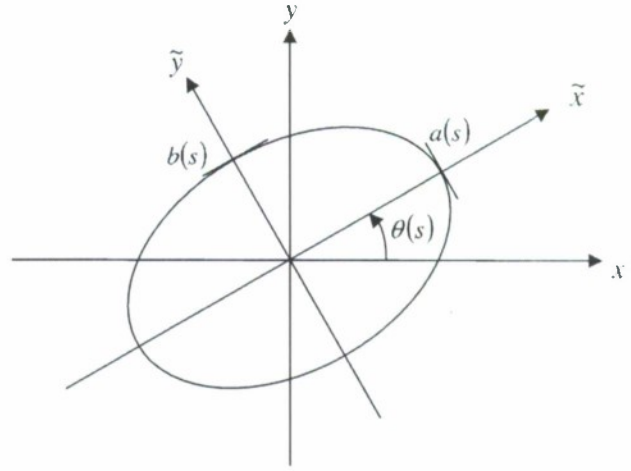


FIG. 1. Laboratory and twisted coordinate systems.

applied magnetic field with $S = 2\pi/k_0$. $N_b = 2\pi \int^\infty dx dy n_b(x, y, s) = \text{const}$ is the number of particles per unit axial length. In the paraxial approximation, the Budker parameter of the beam is assumed to be small, i.e., $q^2 N_b / mc^2 \ll \gamma_b$, and the transverse kinetic energy of a beam particle is assumed to be small compared with its axial kinetic energy. Here, c is the speed of light in vacuo, $\gamma_b = (1 - \beta_b^2)^{-1/2}$ is the relativistic mass factor, and q and m are the particle charge and rest mass, respectively.

From the equilibrium Maxwell equations, we find that the self-electric and self-magnetic fields, \mathbf{E}^s and \mathbf{B}^s , are given by

$$\mathbf{E}^s(\tilde{x}, \tilde{y}, s) = \frac{2qN_b}{a(s) + b(s)} \left[\frac{\tilde{x}}{a(s)} \mathbf{e}_{\tilde{x}} + \frac{\tilde{y}}{b(s)} \mathbf{e}_{\tilde{y}} \right], \quad (4)$$

$$\beta_b^{-1} \mathbf{B}^s(\tilde{x}, \tilde{y}, s) = \frac{2qN_b}{a(s) + b(s)} \left[-\frac{\tilde{y}}{b(s)} \mathbf{e}_{\tilde{x}} + \frac{\tilde{x}}{a(s)} \mathbf{e}_{\tilde{y}} \right], \quad (5)$$

in the beam interior ($\tilde{x}^2/a^2 + \tilde{y}^2/b^2 \leq 1$). It is convenient to express the self-fields in terms of the scalar and vector potentials defined for $\tilde{x}^2/a^2 + \tilde{y}^2/b^2 \leq 1$ by

$$\begin{aligned} \Phi^s(\tilde{x}, \tilde{y}, s) &= \beta_b^{-1} A_z^s(\tilde{x}, \tilde{y}, s) \\ &= -\frac{2qN_b}{a(s) + b(s)} \left[\frac{\tilde{x}^2}{a(s)} + \frac{\tilde{y}^2}{b(s)} \right], \end{aligned} \quad (6)$$

where $\mathbf{A}^s(\tilde{x}, \tilde{y}, s) = A_z^s(\tilde{x}, \tilde{y}, s) \mathbf{e}_z$, $\mathbf{E}^s(\tilde{x}, \tilde{y}, s) = -(\mathbf{e}_{\tilde{x}} \partial / \partial \tilde{x} + \mathbf{e}_{\tilde{y}} \partial / \partial \tilde{y}) \Phi^s$, and $\mathbf{B}^s = (-\mathbf{e}_{\tilde{y}} \partial / \partial \tilde{x} + \mathbf{e}_{\tilde{x}} \partial / \partial \tilde{y}) A_z^s$.

In the paraxial approximation, the transverse motion for an individual particle in the combined self-fields and applied magnetic field is described by the normalized perpendicular Hamiltonian $\hat{H}_\perp = H_\perp / \gamma_b \beta_b mc^2$,

$$\begin{aligned} \hat{H}_\perp(x, y, P_x, P_y, s) = & \frac{1}{2} \left[\left(P_x + \sqrt{\kappa_z(s)} \frac{k_{0y}^2}{k_0^2} y \right)^2 \right. \\ & + \left. \left(P_y - \sqrt{\kappa_z(s)} \frac{k_{0x}^2}{k_0^2} x \right)^2 \right] \\ & - \frac{K}{a+b} \left[\frac{\tilde{x}^2}{a} + \frac{\tilde{y}^2}{b} \right]. \end{aligned} \quad (7)$$

where (x, P_x) and (y, P_y) are canonical conjugate pairs, $\sqrt{\kappa_z(s)} = qB_z(s)/2\gamma_b\beta_b mc^2$, $K = 2q^2 N_b / \gamma_b^3 \beta_b^2 mc^2$ is the self-field perveance, and the normalized transverse canonical momentum $\mathbf{P}_\perp = (P_x, P_y)$ is related to the transverse mechanical momentum \mathbf{p}_\perp by $\mathbf{P}_\perp = (\gamma_b\beta_b mc)^{-1} \times (\mathbf{p}_\perp + q\mathbf{A}_\perp^{\text{ext}}/c)$.

It is convenient to transform the Hamiltonian in the Cartesian canonical coordinate (x, y, P_x, P_y) to a new canonical coordinate $(x_1, y_1, P_{x1}, P_{y1})$, so that the new Hamiltonian assumes a simpler form from which the invariants of motion are easily identified. The transformation of the Hamiltonian from the Cartesian canonical coordi-

nate (x, y, P_x, P_y) to the canonical coordinate $(x_1, y_1, P_{x1}, P_{y1})$ involves two steps.

We first transform the Cartesian canonical coordinate (x, y, P_x, P_y) to a twisted canonical coordinate $(\tilde{x}, \tilde{y}, \tilde{P}_x, \tilde{P}_y)$ using the generating function

$$\begin{aligned} F_2(x, y; \tilde{P}_x, \tilde{P}_y, s) = & \tilde{P}_x [x \cos\theta(s) + y \sin\theta(s)] \\ & + \tilde{P}_y [-x \sin\theta(s) + y \cos\theta(s)]. \end{aligned} \quad (8)$$

It follows from Eq. (8) that

$$P_x = \tilde{P}_x \cos\theta(s) - \tilde{P}_y \sin\theta(s), \quad (9a)$$

$$P_y = \tilde{P}_x \sin\theta(s) + \tilde{P}_y \cos\theta(s), \quad (9b)$$

$$\tilde{x} = x \cos\theta(s) + y \sin\theta(s), \quad (9c)$$

$$\tilde{y} = -x \sin\theta(s) + y \cos\theta(s). \quad (9d)$$

The Hamiltonian in the twisted canonical coordinate is then expressed as

$$\begin{aligned} \tilde{H}_\perp(\tilde{x}, \tilde{y}, \tilde{P}_x, \tilde{P}_y, s) = & \hat{H}_\perp(x, y, P_x, P_y, s) + \partial F_2 / \partial s \\ = & \frac{1}{2} \left[\tilde{P}_x \cos\theta(s) - \tilde{P}_y \sin\theta(s) + \sqrt{\kappa_z(s)} \frac{k_{0y}^2}{k_0^2} \tilde{x} \sin\theta(s) + \sqrt{\kappa_z(s)} \frac{k_{0y}^2}{k_0^2} \tilde{y} \cos\theta(s) \right]^2 \\ & + \frac{1}{2} \left[\tilde{P}_x \sin\theta(s) + \tilde{P}_y \cos\theta(s) - \sqrt{\kappa_z(s)} \frac{k_{0x}^2}{k_0^2} \tilde{x} \cos\theta(s) + \sqrt{\kappa_z(s)} \frac{k_{0x}^2}{k_0^2} \tilde{y} \sin\theta(s) \right]^2 \\ & - \frac{K}{a+b} \left(\frac{\tilde{x}^2}{a} + \frac{\tilde{y}^2}{b} \right) + (\tilde{P}_x \tilde{y} - \tilde{P}_y \tilde{x}) \frac{d\theta(s)}{ds}. \end{aligned} \quad (10)$$

The equations of motion associated with the Hamiltonian in Eq. (10) are

$$\tilde{x}' = \frac{\partial \tilde{H}_\perp}{\partial \tilde{P}_x} = \tilde{P}_x + C(s)\tilde{x} + [\theta'(s) - \alpha_x(s)]\tilde{y}, \quad (11a)$$

$$\tilde{y}' = \frac{\partial \tilde{H}_\perp}{\partial \tilde{P}_y} = \tilde{P}_y - C(s)\tilde{y} - [\theta'(s) - \alpha_y(s)]\tilde{x}, \quad (11b)$$

$$\begin{aligned} \tilde{P}_x' = -\frac{\partial \tilde{H}_\perp}{\partial \tilde{x}} = & - \left\{ \kappa_z(s) \frac{k_{0x}^4 \cos^2[\theta(s)] + k_{0y}^4 \sin^2[\theta(s)]}{k_0^4} - \frac{2K}{a(s)[a(s) + b(s)]} \right\} \tilde{x} - C(s)\tilde{P}_x + [\theta'(s) - \alpha_y(s)]\tilde{P}_y \\ & - \kappa_z(s) \left(\frac{k_{0y}^4 - k_{0x}^4}{k_0^4} \right) \frac{\sin[2\theta(s)]}{2} \tilde{y}, \end{aligned} \quad (11c)$$

$$\begin{aligned} \tilde{P}_y' = -\frac{\partial \tilde{H}_\perp}{\partial \tilde{y}} = & - \left\{ \kappa_z(s) \frac{k_{0x}^4 \sin^2[\theta(s)] + k_{0y}^4 \cos^2[\theta(s)]}{k_0^4} - \frac{2K}{b(s)[a(s) + b(s)]} \right\} \tilde{y} + C(s)\tilde{P}_y - [\theta'(s) - \alpha_x(s)]\tilde{P}_x \\ & - \kappa_z(s) \left(\frac{k_{0y}^4 - k_{0x}^4}{k_0^4} \right) \frac{\sin[2\theta(s)]}{2} \tilde{x}, \end{aligned} \quad (11d)$$

where prime denotes derivative with respect to s ,

$$C(s) \equiv \sqrt{\kappa_z(s)} \frac{k_{0y}^2 - k_{0x}^2}{2k_0^2} \sin[2\theta(s)], \quad (12)$$

$$\alpha_x(s) = -\sqrt{\kappa_z(s)} \left\{ \frac{k_{0x}^2}{k_0^2} \sin^2[\theta(s)] + \frac{k_{0y}^2}{k_0^2} \cos^2[\theta(s)] \right\}, \quad (13)$$

and

$$\alpha_y(s) = -\sqrt{\kappa_z(s)} \left\{ \frac{k_{0x}^2}{k_0^2} \cos^2[\theta(s)] + \frac{k_{0y}^2}{k_0^2} \sin^2[\theta(s)] \right\}. \quad (14)$$

The functions α_x and α_y are related to the variables α_x and α_y in the cold-fluid equilibrium theory [6]. Indeed, by adding Eqs. (10) and (11) and subtracting Eq. (10) from Eq. (11) in [6], and carrying out the integrations on resulting equations with the initial condition $\alpha_x(0) = \alpha_y(0) = 0$, it is readily shown that the functions α_x and α_y in Eqs. (13) and (14) correspond to a particular solution to Eqs. (10) and (11) in [6].

As a second step, we apply another transformation from the twisted canonical variables $(\tilde{x}, \tilde{y}, \tilde{P}_x, \tilde{P}_y)$ to the canonical variables $(x_1, y_1, P_{x1}, P_{y1})$ using the generating function

$$\begin{aligned} \tilde{F}_2(\tilde{x}, \tilde{y}; P_{x1}, P_{y1}, s) = & \frac{1}{2} \left[\frac{w'_x(s)}{w_x(s)} - C(s) \right] \tilde{x}^2 \\ & + \frac{1}{2} \left[\frac{w'_y(s)}{w_y(s)} + C(s) \right] \tilde{y}^2 \\ & + \frac{\tilde{x}P_{x1}}{w_x(s)} + \frac{\tilde{y}P_{y1}}{w_y(s)}, \end{aligned} \quad (15)$$

where $w_x(s) = w_x(s + S)$ and $w_y(s) = w_y(s + S)$ are periodic functions solving the differential equations

$$\begin{aligned} \frac{w''_x(s)}{w_x(s)} - C'(s) - C^2(s) - \alpha_y - \frac{2K}{a(s)[a(s) + b(s)]} \\ = \frac{1}{w_x^4(s)}, \end{aligned} \quad (16)$$

$$\begin{aligned} \frac{w''_y(s)}{w_y(s)} + C'(s) - C^2(s) - \alpha_x - \frac{2K}{b(s)[a(s) + b(s)]} \\ = \frac{1}{w_y^4(s)}. \end{aligned} \quad (17)$$

It follows from Eq. (15) that

$$\tilde{P}_x = \left[\frac{w'_x(s)}{w_x(s)} - C(s) \right] \tilde{x} + \frac{P_{x1}}{w_x(s)}, \quad (18a)$$

$$\tilde{P}_y = \left[\frac{w'_y(s)}{w_y(s)} + C(s) \right] \tilde{y} + \frac{P_{y1}}{w_y(s)}, \quad (18b)$$

$$x_1 = \frac{\tilde{x}}{w_x(s)}, \quad (18c)$$

$$y_1 = \frac{\tilde{y}}{w_y(s)}. \quad (18d)$$

The Hamiltonian in the canonical coordinate $(x_1, y_1, P_{x1}, P_{y1})$ is then expressed as

$$\begin{aligned} H_{1\perp}(x_1, y_1, P_{x1}, P_{y1}, s) = & \tilde{H}_\perp(\tilde{x}, \tilde{y}, \tilde{P}_x, \tilde{P}_y, s) + \frac{\partial \tilde{F}_2}{\partial s} \\ = & \frac{1}{2} \left\{ \frac{P_{x1}^2}{w_x^2(s)} + \frac{P_{y1}^2}{w_y^2(s)} + \frac{x_1^2}{w_x^2(s)} \right. \\ & \left. + \frac{y_1^2}{w_y^2(s)} \right\} \\ & + \frac{d\varphi(s)}{ds} (y_1 P_{x1} - x_1 P_{y1}), \end{aligned} \quad (19)$$

where we have introduced and demanded

$$\frac{d\varphi(s)}{ds} \equiv \frac{w_y(s)}{w_x(s)} \left\{ \frac{d\theta(s)}{ds} - \alpha_x \right\} = \frac{w_x(s)}{w_y(s)} \left\{ \frac{d\theta(s)}{ds} - \alpha_y \right\}. \quad (20)$$

Following Eq. (20), it can be shown that the twisted angle $\theta(s)$ has to satisfy the differential equation

$$\frac{d\theta(s)}{ds} = \frac{w_x^2(s)\alpha_y(s) - w_y^2(s)\alpha_x(s)}{w_x^2(s) - w_y^2(s)}. \quad (21)$$

The motion described by the simplified Hamiltonian in the new canonical coordinate $(x_1, y_1, P_{x1}, P_{y1})$ in Eq. (19) is described by the equations

$$x'_1 = \frac{\partial H_{1\perp}}{\partial P_{x1}} = \frac{P_{x1}}{w_x^2(s)} + \frac{d\varphi(s)}{ds} y_1, \quad (22a)$$

$$y'_1 = \frac{\partial H_{1\perp}}{\partial P_{y1}} = \frac{P_{y1}}{w_y^2(s)} - \frac{d\varphi(s)}{ds} x_1, \quad (22b)$$

$$P'_{x1} = -\frac{\partial H_{1\perp}}{\partial x_1} = -\frac{x_1}{w_x^2(s)} + \frac{d\varphi(s)}{ds} P_{y1}, \quad (22c)$$

$$P'_{y1} = -\frac{\partial H_{1\perp}}{\partial y_1} = -\frac{y_1}{w_y^2(s)} - \frac{d\varphi(s)}{ds} P_{x1}. \quad (22d)$$

From Eq. (22), it is readily shown that

$$E = x_1^2 + y_1^2 + P_{x1}^2 + P_{y1}^2 \quad (23)$$

is an exact single-particle constant of the motion for the Hamiltonian in Eq. (19).

We consider the following trial choice of the Vlasov equilibrium distribution function:

$$f_b(x_1, y_1, P_{x1}, P_{y1}, s) = \frac{N_b}{\pi^2 \varepsilon_T} \delta(x_1^2 + y_1^2 + P_{x1}^2 + P_{y1}^2 - \varepsilon_T), \quad (24)$$

where $df_b/ds = 0$, $\varepsilon_T = \text{const} > 0$ is an effective emittance, and $\delta(x)$ is the Dirac δ function. As will be shown in Sec. III, the density profile of the beam described by the distribution function f_b is consistent with the uniform-density profile within an ellipse, which is the key requirement for the quantity $E = x_1^2 + y_1^2 + P_{x1}^2 + P_{y1}^2$ to be a constant of motion. Therefore, the distribution function defined in Eq. (24) is indeed a Vlasov equilibrium, i.e.,

$$\frac{\partial f_b}{\partial s} = 0. \quad (25)$$

III. STATISTICAL PROPERTIES

The distribution function described in Eq. (24) has the following statistical properties. First, the distribution is consistent with the assumed density profile in Eq. (3), i.e.,

$$\begin{aligned} n_b(\tilde{x}, \tilde{y}, s) &= \frac{1}{w_x w_y} \iint f dP_{x1} dP_{y1} \\ &= \begin{cases} N_b / (\pi \epsilon_T w_x w_y), & \text{if } x_1^2 / \epsilon_T + y_1^2 / \epsilon_T \leq 1, \\ 0, & \text{otherwise.} \end{cases} \end{aligned} \quad (26)$$

The beam has the uniform-density profile given in Eq. (3), provided that $a = \sqrt{\epsilon_T w_x}$ and $b = \sqrt{\epsilon_T w_y}$ are satisfied. Under these self-consistent conditions, Eqs. (16), (17), and (21) can be expressed as

$$\begin{aligned} \frac{d^2 a}{ds^2} &- \left[\frac{b^2(\alpha_x^2 - 2\alpha_x \alpha_y) + a^2 \alpha_y^2}{a^2 - b^2} \right. \\ &+ \left. \sqrt{\kappa_{z0}} \frac{k_{0x}^2 - k_{0y}^2}{k_0} \cos(k_0 s) \sin(2\theta) - 2\sqrt{\kappa_{z0}} \alpha_y \sin(k_0 s) \right] a \\ &- \frac{2K}{a+b} = \frac{\epsilon_T^2}{a^3}, \end{aligned} \quad (27)$$

$$\begin{aligned} \frac{d^2 b}{ds^2} &+ \left[\frac{a^2(\alpha_y^2 - 2\alpha_x \alpha_y) + b^2 \alpha_x^2}{a^2 - b^2} \right. \\ &+ \left. \sqrt{\kappa_{z0}} \frac{k_{0x}^2 - k_{0y}^2}{k_0} \cos(k_0 s) \sin(2\theta) + 2\sqrt{\kappa_{z0}} \alpha_x \sin(k_0 s) \right] b \\ &- \frac{2K}{a+b} = \frac{\epsilon_T^2}{b^3}, \end{aligned} \quad (28)$$

$$\frac{d\theta}{ds} = \frac{a^2 \alpha_y - b^2 \alpha_x}{a^2 - b^2}. \quad (29)$$

Equations (27)–(29) are written in a form similar to the generalized envelope equations in the cold-fluid equilibrium theory [6]. They are identical to the generalized envelope equations of $a(s)$, $b(s)$, and $\theta(s)$ in the cold-fluid equilibrium theory, except that the emittance terms appearing on the right-hand side of Eqs. (27) and (28) are zero in the cold-fluid equilibrium theory. Therefore, they are more general than the cold-fluid equilibrium theory.

Second, in the normalized units, the average (macroscopic flow) transverse velocity of the beam equilibrium described by Eq. (24) is given in the twisted coordinates by

$$\begin{aligned} \mathbf{v}_\perp &= \left(\frac{N_b}{\pi \epsilon_T w_x w_y} \right)^{-1} \frac{1}{w_x w_y} \int \mathbf{v}_\perp f dP_{x1} dP_{y1} \\ &= \left(\frac{w'_x}{w_x} \tilde{x} - \alpha_x \tilde{y} \right) \mathbf{e}_{\tilde{x}} + \left(\frac{w'_y}{w_y} \tilde{y} + \alpha_y \tilde{x} \right) \mathbf{e}_{\tilde{y}}. \end{aligned} \quad (30)$$

The flow velocity in Eq. (30) is identical to the flow velocity derived by the cold-fluid equilibrium theory [6] provided that the relations $\mu_x = a'/a = w'_x/w_x$ and $\mu_y = b'/b = w'_y/w_y$ are satisfied.

As a third statistical property, the beam equilibrium described by Eq. (24) has the effective transverse temperature profile (in dimensional units)

$$\begin{aligned} T_\perp(\tilde{x}, \tilde{y}, s) &= \left(\frac{N_b}{\pi \epsilon_T w_x w_y} \right)^{-1} \frac{m \gamma_b}{2} \int (\mathbf{v}_\perp - \mathbf{V}_\perp)^2 f dP_{x1} dP_{y1} \\ &= \frac{mc^2 \gamma_b \beta_b^2 \epsilon_T^2}{2} \left(\frac{1}{a^2} + \frac{1}{b^2} \right) \left(1 - \frac{\tilde{x}^2}{a^2} - \frac{\tilde{y}^2}{b^2} \right). \end{aligned} \quad (31)$$

As the fourth property, the rms emittances of the beam in the \tilde{x} and the \tilde{y} directions are

$$\epsilon_{th\tilde{x}} = \frac{1}{\beta_c c} \sqrt{\langle \tilde{x}^2 \rangle \langle (v_{\tilde{x}} - V_{\tilde{x}})^2 \rangle} = \frac{\epsilon_T}{4}, \quad (32a)$$

$$\epsilon_{th\tilde{y}} = \frac{1}{\beta_c c} \sqrt{\langle \tilde{y}^2 \rangle \langle (v_{\tilde{y}} - V_{\tilde{y}})^2 \rangle} = \frac{\epsilon_T}{4}. \quad (32b)$$

Finally, the Vlasov elliptic beam equilibrium has two limiting cases which are well known. It recovers the familiar periodic (circular) rigid-rotor Vlasov equilibrium [10] by setting the major-axis equal to the minor axis of the beam ellipse. It also recovers the familiar constant-radius, uniform-density rigid-rotor Vlasov equilibrium [9] by taking the limit of a uniform magnetic field with $B_z = B = \text{const.}$

IV. EXAMPLES

We illustrate examples of periodically twisted Vlasov elliptic beam equilibria in a periodic nonaxisymmetric magnetic focusing field and the temperature effects with numerical calculations. A numerical module in the PFB2D code [6,21] has been developed to solve the generalized envelope equations (13), (14), and (27)–(29), which determines the rotational flow velocity, the outer equilibrium major axis $a(s)$ and minor axis $b(s)$ of the beam ellipse, and the twisted angle $\theta(s)$.

In particular, we consider a nonrelativistic elliptic beam with voltage $V_b = 2.29$ keV, current $I_b = 0.11$ A, aspect ratio $a/b = 6$, and nonaxisymmetric periodic permanent magnet focusing with $B_0 = 337.5$ G, $S = 1.912$ cm, and $k_{0y}/k_{0x} = 1.6$, which is corresponding to a beam design for a high-efficiency 200 W RBA under development at Massachusetts Institute of Technology (MIT) and beam power technology for wireless communication. For such a system the matched solution of the generalized envelope equations (13), (14), and (27)–(29) is calculated numerically as shown in Figs. 2 and 3 for several maximum (on-axis) temperature choices and fixed parameters: $k_{0x} = 1.90 \text{ cm}^{-1}$, $k_{0y} = 3.03 \text{ cm}^{-1}$, $\sqrt{\kappa_{z0}} = 1.04 \text{ cm}^{-1}$, and $K = 1.52 \times 10^{-2}$. The solutions to the generalized envelope

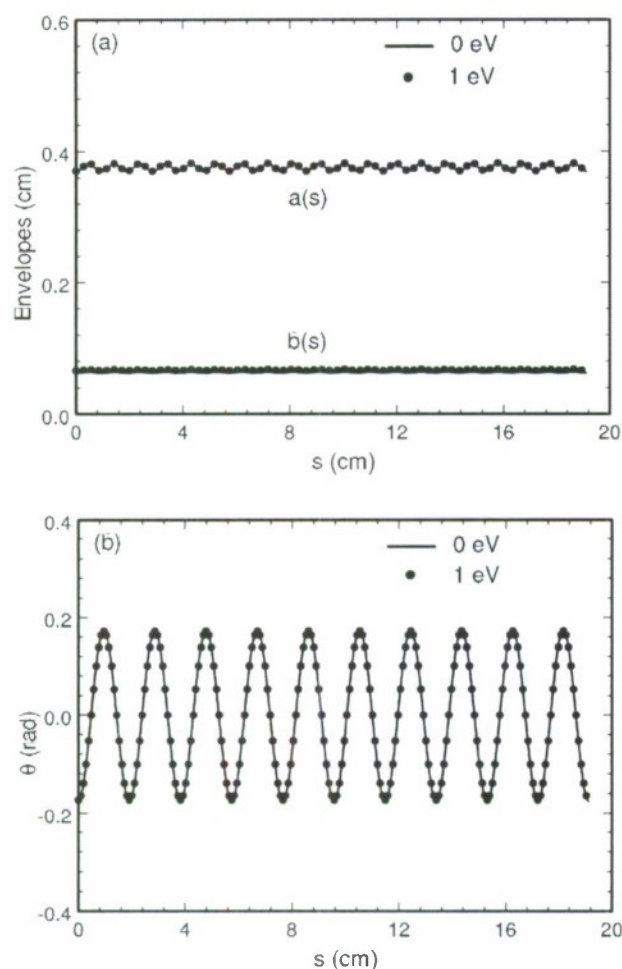


FIG. 2. Plots of (a) envelopes $a(s)$ and $b(s)$ and (b) twist angle $\theta(s)$ versus the axial distance s for the nonrelativistic twisted elliptic beam. The solid curves are the generalized envelope solution for a zero-temperature beam, whereas the dotted curves are for a 1 eV on-axis temperature beam.

lopes equations (13), (14), and (27)–(29), displayed as solid and dotted curves in Figs. 2 and 3, show that the semiaxes of the elliptical beam remain almost constant with small-amplitude oscillations, that the orientation of the ellipse twists periodically with an amplitude of ten degrees.

The solid lines in Figs. 2 and 3 represent the beam envelopes and twisted angle with zero temperature which is corresponding to a cold beam, while the dotted curves represent the beam envelopes and twisted angles with 1 eV on-axis temperature in Fig. 2 and 10 eV on-axis temperature in Fig. 3, respectively. The aspect ratio of the beam reduces from 6 to 4 as the on-axis temperature of the beam increases from 0 to 10 eV, i.e., the elliptic beam becomes more circular. However, the twisted angle is almost unchanged as the on-axis temperature increases from 0 to 10 eV. For the elliptic beam designed for the 200 W ribbon-beam amplifier, the temperature of the beam is estimated to

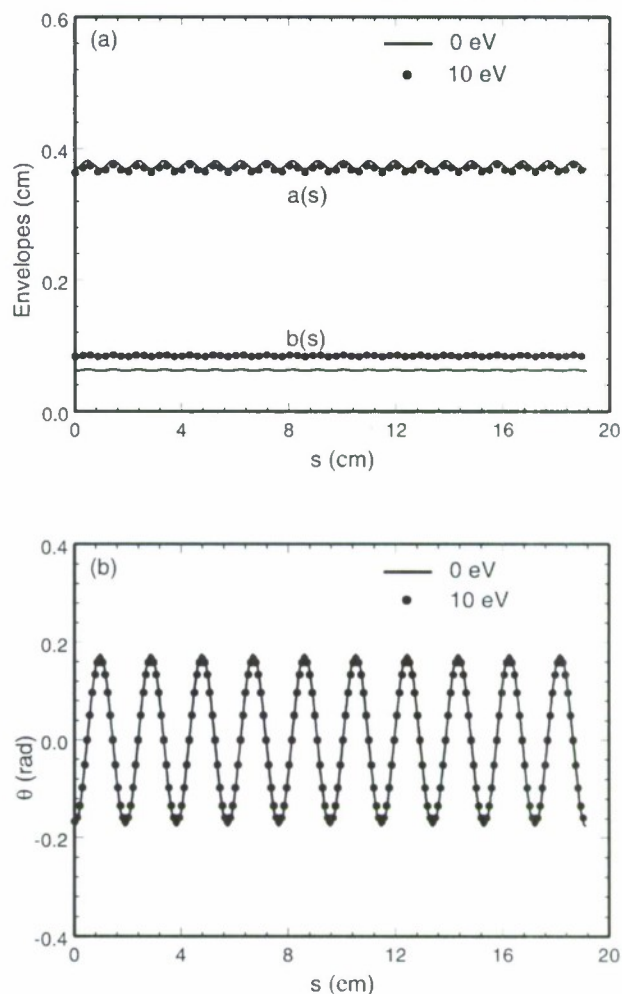


FIG. 3. Plots of (a) envelopes $a(s)$ and $b(s)$ and (b) twist angle $\theta(s)$ versus the axial distance s for the nonrelativistic twisted elliptic beam. The solid curves are the generalized envelope solution for a zero-temperature beam, whereas the dotted curves are for a 10 eV on-axis temperature beam.

be 0.1 eV from simulations [22,23]. In such a case, the temperature effect is negligible.

To further illustrate the effects of beam temperature, we consider a relativistic elliptic beam with $V_b = 198.5$ keV, current $I_b = 85.5$ A, aspect ratio $a/b = 5$, and nonaxisymmetric periodic permanent magnet focusing with $B_0 = 2.4$ kG, $S = 2.2$ cm, and $k_{0y}/k_{0x} = 1.52$. [Such a relativistic elliptic beam could be used in a 10 MW L-band RBK for the International Linear Collider (ILC).] For such a system the matched solution of the generalized envelope equations (13), (14), and (27)–(29) is calculated numerically with the corresponding parameters: $k_{0x} = 1.57$ cm $^{-1}$, $\sqrt{\kappa_{z0}} = 0.732$ cm $^{-1}$, and $K = 1.13 \times 10^{-2}$. As shown in Fig. 4, the solid lines represent the beam semiaxis envelopes and twist angle with zero temperature which is corresponding to a cold beam, while the dotted

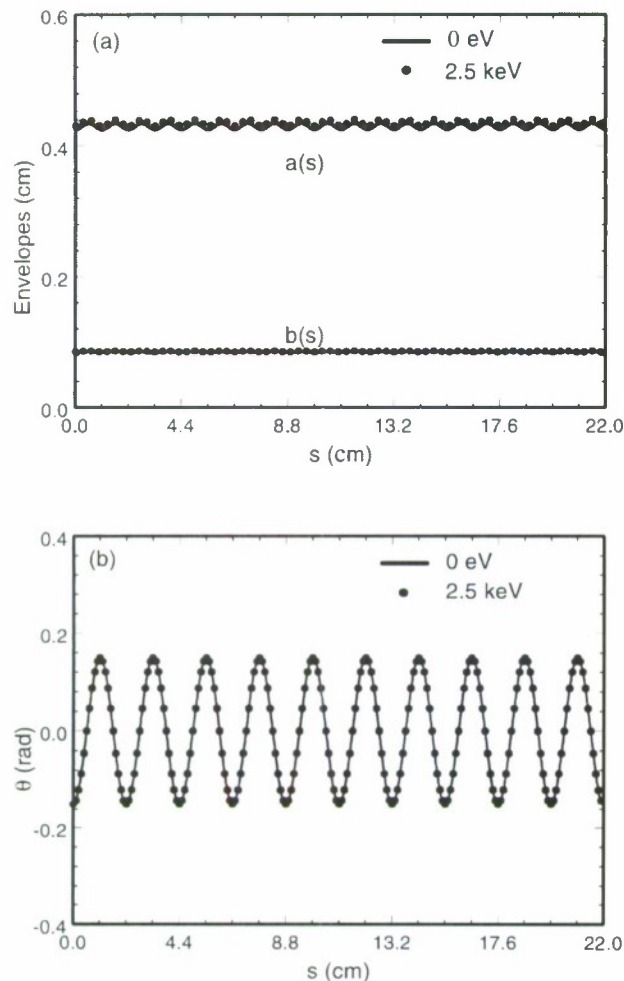


FIG. 4. Plots of (a) envelopes $a(s)$ and $b(s)$ and (b) twist angle $\theta(s)$ versus the axial distance s for the relativistic twisted elliptic beam. The solid curves are the generalized envelope solution for a zero-temperature beam, whereas the dotted curves are for a 2.5 keV on-axis temperature beam.

curves represent the beam envelopes and twist angle with 2.5 keV on-axis temperature. It is evident in Fig. 4 that the temperature effects on the beam envelopes and twist angle are negligibly small. Since an actual relativistic elliptic beam in a well designed system will have a temperature which will be considerably less than 2.5 keV, the results in Fig. 4 imply that the temperature effect on the beam envelopes and twist angle is expected to be negligibly small.

V. CONCLUSIONS

The single-particle Hamiltonian of a periodically twisted large-aspect-ratio elliptic beam in a nonaxisymmetric periodic magnetic focusing field has been investigated. A constant of motion analogous to the Courant-Snyder invariant has been found such that the self-

consistent beam equilibrium can be constructed as a function of the constant of motion. The beam envelope equations and flow velocity equations have been derived. They are consistent with the generalized envelope equations derived from the cold-fluid equilibrium theory [6] when the temperature is taken to be zero. Statistical properties of the present Vlasov elliptic beam equilibrium have been studied. For current applications of interest, namely, the RBA and RBK, the temperature effects have been found to be negligibly small on periodically twisted large-aspect-ratio elliptic beams.

ACKNOWLEDGMENTS

This research was supported by the U.S. Department of Energy, Office of High-Energy Physics, Grant No. DE-FG02-95ER40919, Office of Fusion Energy Science, Grant No. DE-FG02-01ER54662, and in part by Air Force Office of Scientific Research, Grant No. FA9550-06-1-0269.

- [1] R. C. Davidson and C. Chen, *Part. Accel.* **59**, 175 (1998); *Nucl. Instrum. Methods Phys. Res., Sect. A* **415**, 370 (1998).
- [2] R. C. Davidson, P. Stoltz, and C. Chen, *Phys. Plasmas* **4**, 3710 (1997).
- [3] R. Pakter and C. Chen, *Phys. Rev. E* **62**, 2789 (2000).
- [4] C. Chen and R. Pakter, *Phys. Plasmas* **7**, 2203 (2000).
- [5] S. Bernal *et al.*, *Proceedings of the 2005 Particle Accelerator Conference*, 2005, p. 892.
- [6] J. Zhou, R. Bhatt, and C. Chen, *Phys. Rev. ST Accel. Beams* **9**, 034401 (2006).
- [7] I. M. Kapchinskij and V. V. Vladimirskij, in *Proceedings of the International Conference on High Energy Accelerators* (CERN, Geneva, 1959), p. 274.
- [8] S. M. Lund and B. Bukh, *Phys. Rev. ST Accel. Beams* **7**, 024801 (2004).
- [9] R. C. Davidson, *Physics of Nonneutral Plasma* (Addison-Wesley, Reading, MA, 1990).
- [10] C. Chen, R. Pakter, and R. C. Davidson, *Phys. Rev. Lett.* **79**, 225 (1997).
- [11] R. C. Davidson and H. Qin, *Physics of Intense Charged Particle Beams in High Energy Accelerators* (World Scientific, Singapore, 2001), p. 242.
- [12] F. J. Sacherer, Ph.D. thesis, Lawrence Radiation Laboratory, University of California, Berkeley, 1968, pp. 15–19.
- [13] V. Danilov, S. Cousineau, S. Henderson, and J. Holmes, *Phys. Rev. ST Accel. Beams* **6**, 094202 (2003).
- [14] C. Chen, R. Pakter, and R. C. Davidson, *Nucl. Instrum. Methods Phys. Res., Sect. A* **464**, 518 (2001).
- [15] P. A. Sturrock, *J. Electron. Control* **7**, 162 (1959).
- [16] Z. X. Zhang *et al.*, *IEEE Trans. Plasma Sci.* **21**, 760 (1993).
- [17] J. H. Booske, A. H. Kumbasar, and M. A. Basten, *Phys. Rev. Lett.* **71**, 3979 (1993).

-
- [18] M. A. Basten and J. H. Booske, J. Appl. Phys. **85**, 6313 (1999).
- [19] S. J. Russell *et al.*, Phys. Rev. ST Accel. Beams **8**, 080401 (2005).
- [20] E. D. Courant and H. S. Snyder, Ann. Phys. (N.Y.) **3**, 1 (1958).
- [21] J. Zhou, Ph.D. thesis, Massachusetts Institute of Technology, 2006.
- [22] R. Bhatt and C. Chen, Phys. Rev. ST Accel. Beams **8**, 014201 (2005).
- [23] R. Bhatt, T. Bemis, and C. Chen, IEEE Trans. Plasma Sci. **34**, 187 (2006).

Warm-fluid equilibrium theory of a thermal charged-particle beam in a periodic solenoidal focusing field

Ksenia R. Samokhvalova,^{a)} Jing Zhou, and Chiping Chen
*Plasma Science and Fusion Center, Massachusetts Institute of Technology,
 Cambridge, Massachusetts 02139, USA*

(Received 9 May 2007; accepted 10 August 2007; published online 5 October 2007)

A warm-fluid equilibrium theory is presented which describes a new thermal equilibrium of a rotating charged-particle beam in a periodic solenoidal focusing field. Warm-fluid equations are solved in the paraxial approximation. The rms beam envelope, the density and flow velocity profiles, and the self-consistent Poisson equations are derived. Density profiles are calculated numerically for high-intensity and low-intensity beams. Temperature effects in such beams are investigated. Radial confinement of the beam is discussed. © 2007 American Institute of Physics.

[DOI: 10.1063/1.2779281]

I. INTRODUCTION

Many charged-particle beam experiments and applications, such as particle accelerators, spallation neutron sources, high-power microwave sources and high-energy colliders, use high-intensity beams of charged particles. For such systems, beams of high quality (i.e., low emittance, high current, small energy spread, and low beam loss) are required. Exploration of equilibrium states of charged-particle beams and their stability properties is critical to the advancement of basic particle accelerator physics, as well as the design, construction, commissioning, and operation of high-brightness particle beams and accelerator systems.

Of particular concern are emittance growth and beam losses which are related to the evolution of particle beams in their nonequilibrium states. To minimize emittance growth and control beam losses, it is critical to find equilibrium distributions of high-brightness charged-particle beams in accelerators and beam transport systems.

Several kinetic equilibria have been discovered for periodically focused intense charged-particle beams, for example, the Kapchinsky-Vladimirsky (KV) self-consistent two-dimensional Vlasov equilibrium for an intense charged-particle beam in an alternating-gradient quadrupole magnetic focusing field¹ and the periodically focused rigid-rotor Vlasov equilibrium in a periodic solenoidal magnetic focusing field.²⁻⁴ Both equilibria use a δ -function phase-space distribution, which is unphysical. Although there is a well-known rigid-rotor thermal equilibrium in a uniform magnetic field,⁵ periodically focused thermal beam equilibrium has not been reported until our present work, which includes both a kinetic treatment presented elsewhere^{6,7} and a warm-fluid treatment presented in this paper.

In this paper, we present a warm-fluid equilibrium theory of a new thermal charged-particle beam in a periodic solenoidal focusing field. Solving the warm-fluid equations in the paraxial approximation, the beam density and flow velocity are obtained. The self-consistent rms beam envelope equation is derived. The self-consistent Poisson equation, govern-

ing the beam density and potential distributions, is also derived. For such thermal beam equilibria, temperature effects are found to play an important role. Due to temperature effects, the beam density profile has a smooth edge, which is a more realistic representation of the beam density than the uniform density profile in previous theories (see, for example, Refs. 1, 2, and 8). Finally, we discuss the radial confinement of the beam.

The organization of this paper is as follows. In Sec. II, the basic assumptions in the present model are presented. Warm-fluid equilibrium equations are used to derive expressions for the flow velocity profile and beam density distribution, a root-mean-squared (rms) beam envelope equation, and a self-consistent Poisson equation. In Sec. III, a numerical technique for computing the warm-fluid beam equilibria is discussed. Several examples of the thermal beam equilibrium are presented. The radial confinement of the beam is demonstrated. In Sec. IV, the conclusions are presented.

II. WARM-FLUID BEAM EQUILIBRIUM

We consider a thin, continuous, axisymmetric ($\partial/\partial\theta = 0$), single-species charged-particle beam, propagating with constant axial velocity $V_z\hat{e}_z$ through an applied periodic solenoidal magnetic focusing field. The applied periodic solenoidal focusing field inside the beam can be approximated by

$$\mathbf{B}^{\text{ext}}(r, s) = -\frac{1}{2}B'_z(s)r\hat{e}_r + B_z(s)\hat{e}_z, \quad (1)$$

where $s=z$ is the axial coordinate, $r=\sqrt{x^2+y^2}$ is the radial distance from the beam axis, prime denotes the derivative with respect to s , and $B_z(s)=B_z(s+S)$ is the axial magnetic field, which is periodic along the z -axis with periodicity length S .

In the paraxial approximation, $r_{\text{brms}} \ll S$ is assumed, where r_{brms} is the rms beam envelope. The transverse kinetic energy of the beam is assumed to be small compared to its axial kinetic energy, i.e., $|V_z| \gg |V_\perp|$. The Budker parameter of the beam is assumed to be small, i.e., $q^2 N_b / mc^2 \ll \gamma_b$, where q and m are the particle charge and rest mass, respectively, c is the speed of light in vacuum, $N_b = 2\pi \int_0^r dr n_b(r, s)$ is the number of particles per unit axial length, and γ_b is the

^{a)}Electronic mail: ksenias@mit.edu

relativistic mass factor, which, to leading order, is $\gamma_b = \text{const} = (1 - \beta_b^2)^{-1/2}$ with $\beta_b = V_b/c \equiv V_z/c$.

It is convenient to express the self-electric and self-magnetic fields, produced by the space charge and axial current of the beam, in terms of the scalar and vector potentials, i.e., $\mathbf{E}^{\text{self}}(r, s) = -\nabla\phi^{\text{self}}(r, s)$ and $\mathbf{B}^{\text{self}}(r, s) = \nabla \times \mathbf{A}^{\text{self}}(r, s)$. In the paraxial approximation, the self-field potentials ϕ^{self} and \mathbf{A}^{self} are related by the familiar expression $\mathbf{A}^{\text{self}} = A_z^{\text{self}} \hat{\mathbf{e}}_z = \beta_b \phi^{\text{self}}(r, s) \hat{\mathbf{e}}_z$.⁵ Consequently, the self-magnetic field is $\mathbf{B}_\theta^{\text{self}} \hat{\mathbf{e}}_\theta = -\beta_b (\partial \phi^{\text{self}} / \partial r) \hat{\mathbf{e}}_\theta$.

In the paraxial approximation, the warm-fluid equilibrium ($\partial/\partial t = 0$) equations are⁹

$$n_b \mathbf{V} \cdot \nabla (\gamma_b m \mathbf{V}) = n_b q \left[-\nabla \phi^{\text{self}} + \frac{\mathbf{V}}{c} \times (\mathbf{B}^{\text{ext}} + \mathbf{B}^{\text{self}}) \right] - \nabla p, \quad (2)$$

$$\nabla \cdot (n_b \mathbf{V}) = 0, \quad (3)$$

$$\nabla^2 \phi^{\text{self}}(r, s) = -4\pi q n_b(r, s), \quad (4)$$

$$p(r, s) = n_b(r, s) k_B T_\perp(s), \quad (5)$$

$$T_\perp(s) r_{\text{brms}}^2(s) = \text{const}. \quad (6)$$

In Eqs. (2)–(6), $p(r, s)$ is the thermal pressure, $T_\perp(s)$ is the transverse beam temperature which remains constant across the cross section of the beam, and $r_{\text{brms}}(s)$ is the root-mean-square (rms) radius of the beam, defined by $r_{\text{brms}}^2(s) = N_b^{-1} 2\pi \int_0^\infty dr r^3 n_b(r, s)$. Equation (6) states that the beam motion is adiabatic. Note that for the axisymmetric beam in the paraxial approximation, we can approximate $\nabla^2 \equiv (1/r)(\partial/\partial r)r\partial/\partial r$ to leading order in the Poisson equation (4).

We seek a solution for the equilibrium beam profile of the form

$$V_r(r, s) = r \frac{r'_{\text{brms}}(s)}{r_{\text{brms}}(s)} \beta_b c, \quad (7)$$

$$V_\theta(r, s) = r \Omega_b(s), \quad (8)$$

which corresponds to a beam undergoing rotation with the angular frequency $\Omega_b(s)$ to be determined self-consistently later [see Eq. (20)].

The radial component of the momentum equation (2) can be rewritten as

$$\begin{aligned} \frac{\partial}{\partial r} \ln[n_b(r, s)] &= -\frac{\gamma_b m}{k_B T_\perp(s)} r \left\{ \beta_b^2 c^2 \frac{r''_{\text{brms}}(s)}{r_{\text{brms}}(s)} - \Omega_b(s) \cdot [\Omega_b(s) + \Omega_c(s)] \right\} \\ &\quad - \frac{q}{\gamma_b^2 k_B T_\perp(s)} \frac{\partial \phi^{\text{self}}(r, s)}{\partial r}, \end{aligned} \quad (9)$$

where use of Eqs. (5), (7), and (8) have been made and $\Omega_c(s) = qB_z(s)/mc\gamma_b$ is the relativistic cyclotron frequency. Equation (9) can be integrated to give the density profile

$$\begin{aligned} n_b(r, s) &= f(s) \exp \left(-\frac{\gamma_b m \beta_b^2 c^2 r^2}{2 k_B T_\perp(s)} \right) \\ &\quad \times \left\{ \frac{r''_{\text{brms}}(s)}{r_{\text{brms}}(s)} - \frac{\Omega_b(s) \cdot [\Omega_b(s) + \Omega_c(s)]}{\beta_b^2 c^2} \right\} \\ &\quad - \frac{q \phi^{\text{self}}(r, s)}{\gamma_b^2 k_B T_\perp(s)}, \end{aligned} \quad (10)$$

where $f(s)$ is the peak density at the center of the beam, which is an arbitrary function of s to be determined later [see Eq. (18)]. Using the density profile given in Eq. (10), we obtain a useful expression for the rms beam radius, i.e.,

$$\begin{aligned} r_{\text{brms}}^2(s) &= 2 \left[\frac{k_B T_\perp(s)}{\gamma_b m \beta_b^2 c^2} + \frac{q^2 N_b}{2 \gamma_b^3 m \beta_b^2 c^2} \right] \\ &\quad \times \left\{ \frac{r''_{\text{brms}}(s)}{r_{\text{brms}}(s)} - \frac{\Omega_b(s) [\Omega_b(s) + \Omega_c(s)]}{\beta_b^2 c^2} \right\}^{-1}, \end{aligned} \quad (11)$$

where we have assumed that the beam density is infinitely small at $r = \infty$.

Since $k_B T_\perp(s) = (m\gamma_b/2) \langle (v_\perp - V_\perp)^2 \rangle_\Gamma = m\gamma_b \langle (v_x - V_x)^2 \rangle_\Gamma$, $\langle \chi^2 \rangle_\Gamma = r_{\text{brms}}^2(s)/2$, we can express the rms thermal emittance of the beam as

$$\varepsilon_{\text{th}}^2 = (\beta_b c)^{-2} \langle \chi^2 \rangle_\Gamma \langle (v_x - V_x)^2 \rangle_\Gamma = \frac{k_B T_\perp(s) r_{\text{brms}}^2(s)}{2 m \gamma_b \beta_b^2 c^2}. \quad (12)$$

where the statistical average of χ is defined in the usual manner by $\langle \chi \rangle_\Gamma = N_b^{-1} \int \chi f_b dx dy dp_x dp_y$ with f_b being the particle distribution function corresponding to the warm-fluid beam equilibrium.^{6,7} Combining Eqs. (11) and (12) yields the following rms beam envelope equation

$$r''_{\text{brms}}(s) - \frac{\Omega_b(s) [\Omega_b(s) + \Omega_c(s)]}{\beta_b^2 c^2} r_{\text{brms}}(s) - \frac{K}{2 r_{\text{brms}}(s)} = \frac{4\varepsilon_{\text{th}}^2}{r_{\text{brms}}^3(s)}, \quad (13)$$

where $K \equiv 2N_b q^2 / \gamma_b^3 m \beta_b^2 c^2$ is the self-field perveance.

Substituting Eq. (13) into Eq. (10) we obtain the simplified expression for the equilibrium beam density

$$n_b(r, s) = f(s) \exp \left\{ -\frac{r^2}{4\varepsilon_{\text{th}}^2} \left[\frac{K}{2} + \frac{4\varepsilon_{\text{th}}^2}{r_{\text{brms}}^2(s)} \right] - \frac{q \phi^{\text{self}}(r, s)}{\gamma_b^2 k_B T_\perp(s)} \right\}, \quad (14)$$

where the scalar potential for the self-electric field satisfies the Poisson equation

$$\begin{aligned} \frac{1}{r} \frac{\partial}{\partial r} \left[r \frac{\partial}{\partial r} \phi^{\text{self}}(r, s) \right] &= -4\pi q f(s) \exp \left\{ -\frac{r^2}{4\varepsilon_{\text{th}}^2} \left[\frac{K}{2} + \frac{4\varepsilon_{\text{th}}^2}{r_{\text{brms}}^2(s)} \right] - \frac{q \phi^{\text{self}}(r, s)}{\gamma_b^2 k_B T_\perp(s)} \right\}. \end{aligned} \quad (15)$$

Note that when $B_z(s) = \text{const}$, the beam density in Eq. (14) recovers the well-known thermal rigid-rotor equilibrium in a uniform magnetic field.⁵

The density profile in the form of Eq. (14) and the velocity profiles (7) and (8) have to satisfy the continuity Eq.

(3). Substituting Eqs. (7), (8), and (14) into Eq. (3), and integrating over the cross section of the beam yields

$$\frac{d}{ds} \left[2 \frac{r'_{\text{brms}}}{r_{\text{brms}}} + \frac{1}{f(s)} \frac{df(s)}{ds} \right] - \frac{K}{4\epsilon_{\text{tb}}^2} \frac{d}{ds} \left[\frac{r_{\text{brms}}^2(s)}{2} + r_{\text{brms}}^2(s) \left\langle \frac{\phi^{\text{self}}(r,s)}{qN_b} \right\rangle \right] = 0. \quad (16)$$

Note that Eq. (16) is equivalent to the conservation of the total number of particles per unit axial length, i.e.,

$$\frac{dN_b}{ds} = 0, \quad \text{or } N_b = \text{const.} \quad (17)$$

Setting the sum of the first two terms in Eq. (16) to zero gives

$$f(s) \equiv \frac{C}{r_{\text{brms}}^2(s)}, \quad (18)$$

where C is a constant of integration.

We solve the Poisson equation (15) to determine the electric self-field potential, with $f(s)$ satisfying Eq. (18), where the electric self-field potential on axis $\phi^{\text{self}}(r=0,s)$ is determined by setting the sum of the third and fourth terms in Eq. (16) to zero. A numerical scheme for determining $\phi^{\text{self}}(r=0,s)$ will be described in Sec. III. The electric self-field potential energy on axis $q\phi^{\text{self}}(0,s)$ is very small compared to the beam transverse thermal energy, which will be demonstrated in Sec. III.

To gain further insight into the azimuthal motion of the beam, we make use of Eqs. (7) and (8) to re-express the azimuthal component of the momentum equation (2), i.e.,

$$n_b(r,s) \left[r \frac{r'_{\text{brms}}(s)}{r_{\text{brms}}(s)} \beta_b c \frac{\partial}{\partial r} + \beta_b c \frac{\partial}{\partial s} \right] \left[\Omega_b(s)r^2 + \frac{1}{2} \Omega_c(s)r^2 \right] = 0. \quad (19)$$

Consistent with Eq. (8), we find the solution to Eq. (19) as

$$\Omega_b(s) = -\frac{1}{2} \Omega_c(s) + \frac{\omega_b r_{b0}^2}{r_{\text{brms}}^2(s)}, \quad (20)$$

where ω_b and r_{b0} are constants. In Eq. (20), the term $\omega_b r_{b0}^2 / r_{\text{brms}}^2(s)$ represents the azimuthal beam rotation relative to the Larmor frame, which rotates at the frequency $-\Omega_c(s)/2$ relative to the laboratory frame.

Substituting Eq. (20) into Eq. (13), we obtain the following alternative form of the rms beam envelope equation:

$$r''_{\text{brms}}(s) + \left[\kappa_z(s) - \frac{\omega_b^2 r_{b0}^4}{r_{\text{brms}}^4(s) \beta_b^2 c^2} \right] r_{\text{brms}}(s) - \frac{K}{2r_{\text{brms}}(s)} = \frac{4\epsilon_{\text{tb}}^2}{r_{\text{brms}}^3(s)}, \quad (21)$$

where $\sqrt{\kappa_z(s)} \equiv qB_z(s)/2\gamma_b\beta_b mc^2$ is the focusing parameter. In the limit $\epsilon_{\text{tb}}=0$, Eq. (21) recovers the previous envelope equation for the cold-fluid beam equilibrium.⁸

Note that the term proportional to $\omega_b^2 r_{b0}^4 / r_{\text{brms}}^3(s)$ in Eq. (21) plays the role of an effective emittance contribution to the envelope equation associated with the average azimuthal

beam rotation relative to the Larmor frame, and that the rms beam envelope equation (21) agrees with the well-known rms envelope equation,¹⁰ with the interpretation of the total emittance

$$\epsilon_T^2 = 16\epsilon_{\text{tb}}^2 + 4 \frac{\omega_b^2 r_{b0}^4}{\beta_b^2 c^2}. \quad (22)$$

III. EXAMPLES OF WARM-FLUID BEAM EQUILIBRIA

In this section, we present a numerical technique for computing the warm-fluid beam equilibria. We calculate the beam density by solving the self-consistent Poisson equation and present several examples of warm-fluid beam equilibria. We show that thermal beam equilibria exist for a wide range of parameters and discuss the radial confinement of the beam.

To determine the warm-fluid beam equilibrium numerically, we obtain the matched rms beam envelope by solving the rms beam envelope equation (21) with periodic boundary conditions.² Then, we use the matched rms beam envelope in the calculation of the beam density and potential at any given s from Eqs. (14) and (15).

We calculate the scalar potential for the self-electric field using the Poisson equation (15). We rewrite the Poisson equation (15) as

$$\begin{aligned} & \frac{1}{r} \frac{\partial}{\partial r} \left[r \frac{\partial}{\partial r} \Delta \phi(r,s) \right] \\ &= -\frac{4\pi qC}{r_{\text{brms}}^2(s)} \exp \left[-\frac{q\phi^{\text{self}}(r=0,s)}{\gamma_b^2 k_B T_{\perp}(s)} \right] \\ & \times \exp \left\{ -\frac{r^2}{4\epsilon_{\text{tb}}^2} \left[\frac{K}{2} + \frac{4\epsilon_{\text{tb}}^2}{r_{\text{brms}}^2(s)} \right] - \frac{q\Delta\phi(r,s)}{\gamma_b^2 k_B T_{\perp}(s)} \right\}, \end{aligned} \quad (23)$$

where $\Delta\phi(r,s) \equiv \phi^{\text{self}}(r,s) - \phi^{\text{self}}(r=0,s)$ and use has been made of Eq. (18). We solve Eq. (23) with the boundary conditions

$$\Delta\phi(0,s) = 0 \quad \text{and} \quad \left. \frac{\partial \Delta\phi(r,s)}{\partial r} \right|_{r=0} = 0. \quad (24)$$

We integrate Eq. (23) from $r=0$ to a few r_{brms} , paying special attention to the singularity at $r=0$. To avoid the singularity, we analytically integrate Eq. (23) with boundary conditions (24) near the z -axis from $r=0$ to $r=\Delta r$ (with $\Delta r \ll r_{\text{brms}}$), treating the beam density as a constant. Then, we approximate $\Delta\phi(r,s)$ by the scalar potential of the space-charge-dominated beam with $SK/\epsilon_{\text{th}} \gg 1$ as

$$\Delta\phi(r,s) \approx -\frac{qN_b}{2r_{\text{brms}}^2(s)} r^2, \quad \text{for } r \leq \sqrt{2}r_{\text{brms}}. \quad (25)$$

Using this potential we numerically integrate Eq. (23) outward from $r=\Delta r$.

For the purposes of numerical calculations, it is useful to rewrite Eq. (17) as

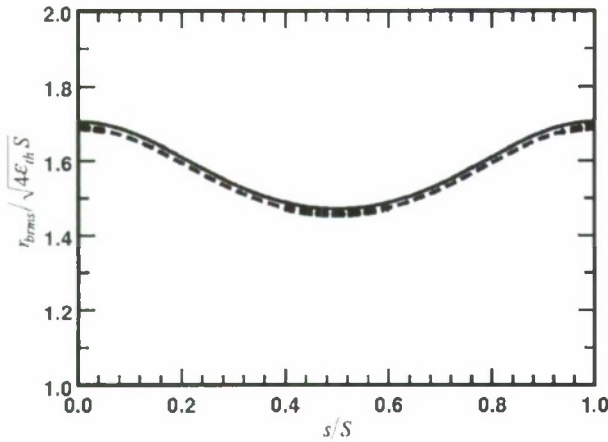


FIG. 1. Normalized beam envelope profiles for $S\sqrt{\kappa_z(s)} = a_0 + a_1 \cos(2\pi s/S)$, $a_0 = a_1 = 1.14$, $\omega_b = 0$, a warm-fluid (solid curve) beam equilibrium with $\hat{K} = 10$, and a cold-fluid (dashed curve) beam equilibrium with $\hat{K} = \infty$.

$$\begin{aligned} \Delta &\equiv 1 - N_b^{-1} \int_0^\infty 2\pi n_b r dr \\ &= 1 - C \exp \left[-\frac{q\phi^{\text{self}}(r=0, s)}{\gamma_b^2 k_B T_\perp(s)} \right] \\ &\quad \times \int_0^\infty \exp \left\{ -\frac{r^2}{4\varepsilon_{\text{th}}^2} \left[\frac{K}{2} + \frac{4\varepsilon_{\text{th}}^2}{r_{\text{brms}}^2(s)} \right] - \frac{q\Delta\phi(r, s)}{\gamma_b^2 k_B T_\perp(s)} \right\} r dr \\ &= 0. \end{aligned} \quad (26)$$

In our numerical calculations, an iterative procedure is applied to solve Eq. (26), and Δ is less than 10^{-4} .

Figure 1 shows the rms envelope profiles for $S\sqrt{\kappa_z(s)} = a_0 + a_1 \cos(2\pi s/S)$, $a_0 = a_1 = 1.14$, $\omega_b = 0$, a warm-fluid (solid curve) beam equilibrium with the “scaled” normalized perveance $\hat{K} \equiv KS/4\varepsilon_{\text{th}} = 10$, and a cold-fluid (dashed curve) beam equilibrium with $\hat{K} = \infty$. The rms beam radius $r_{\text{brms}}^{\text{cold}}(s)$ for the cold-fluid beam equilibrium is determined from Eq. (21) with the right-hand side equal to zero. In Fig. 1, the effects of the finite temperature enlarge the rms beam envelope by 1%.

In Fig. 2 we plot the on-axis electric self-field potential energy relative to the beam transverse thermal energy, $q\phi^{\text{self}}(0, s)/\gamma_b^2 k_B T_\perp(s)$, as a function of s/S for $\hat{K} = 0.1, 1$, and 10. The rest of the parameters are the same as in Fig. 1. The integration constant C is chosen such that $\phi^{\text{self}}(0, S/4) = 0$. The electric self-field potential on axis is indeed small, which is consistent with the paraxial approximation.

Figure 3 shows the density profiles for the warm-fluid (solid curve) and cold-fluid (dashed curve) beam equilibria corresponding to the examples discussed in Fig. 1. The warm-fluid beam density is nearly uniform up to the beam edge where it falls rapidly within a few Debye lengths. Here, the Debye length is defined as

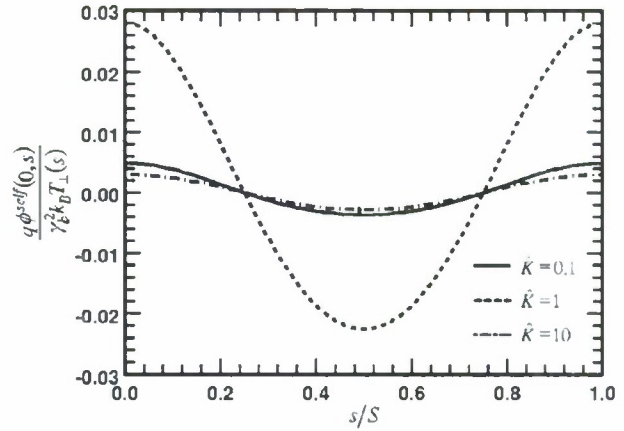


FIG. 2. Plot of the on-axis electric self-field potential energy relative to the beam transverse thermal energy as a function of s/S for $\hat{K} = 0.1, 1$, and 10. The other system parameters are the same as in Fig. 1.

$$\lambda_D \equiv \sqrt{\frac{\gamma_b^2 k_B T_\perp(s)}{4\pi q^2 n_b(0, s)}}. \quad (27)$$

For the warm-fluid beam equilibrium, $r_{\text{brms}} \approx 15.4\lambda_D$. The density of the cold [$T_\perp(s) \equiv 0$] beam is (see, for example, Ref. 8)

$$n_b^{\text{cold}}(r, s) = \frac{N_b}{2\pi r_{\text{brms}}^{\text{cold}}(s)^2}, \quad \text{for } r \leq \sqrt{2} r_{\text{brms}}^{\text{cold}}(s). \quad (28)$$

The effect of the beam temperature on beam density distribution is illustrated in Fig. 4. As we increase the beam temperature and keep other system parameters the same, \hat{K} decreases, and the density profile makes the transition from a step-function profile (for $T_\perp = 0$) to a bell-shape profile, as shown in Fig. 4.

There is a wide range of parameters for which the warm-fluid beam equilibrium exists in a periodic focusing channel. For practical purposes, it is useful to determine the radial confinement in an average sense. In Fig. 5, we plot the nor-

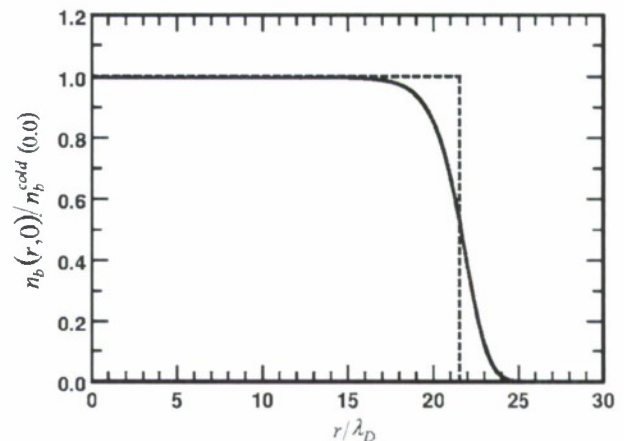


FIG. 3. Plot of the relative beam density vs. r/λ_D for a warm-fluid beam equilibrium (solid curve) and a cold-fluid beam equilibrium (dashed curve) at $s=0$ for the same parameters as in Fig. 1. Here, $r_{\text{brms}} \approx 15.4\lambda_D$ for the warm-fluid beam equilibrium.

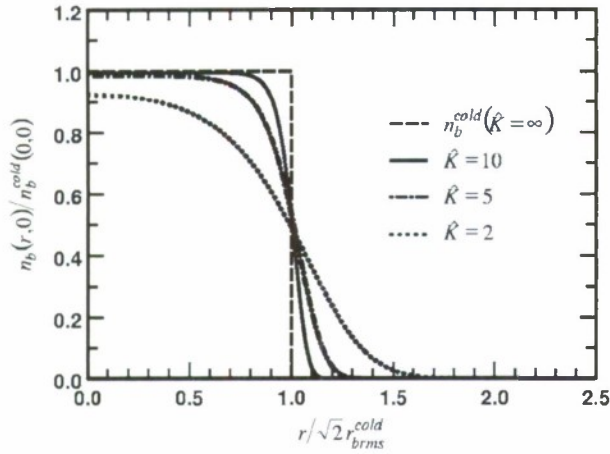


FIG. 4. Plot of the relative density profiles at $s=0$ at several temperatures: $\hat{K}=\infty$ (cold), 10, 5, and 2. The other system parameters are kept the same as in Fig. 1.

malized angular frequency of beam rotation in the Larmor frame, $(S/\sigma_v\beta_b c)(\Omega_b(s) + \Omega_c(s)/2)$, as a function of the effective self-field parameter $\langle s_e \rangle \equiv S^2 \langle \omega_{pb}^2(s) \rangle / 2 \gamma_b^2 \sigma_v^2 \beta_b^2 c^2$ for $\hat{K}=0.1, 0.2, 1$, and 10. The beam propagates in a periodic solenoidal focusing field with $S\sqrt{\kappa_z(s)} = a_0 + a_1 \cos(2\pi s/S)$, where $a_0 = a_1 = 1.14$. The beam current is kept the same while the rms thermal emittance ϵ_{th} of the beam decreases. Here, $\omega_{pb}(s) \equiv (4\pi q^2 n_b(0,s) / \gamma_b m)^{1/2}$ is the plasma frequency, $\sigma_v \equiv \int_0^S w_0^2(s) ds$ is the vacuum phase advance over one axial period S , the amplitude function $w_0(s)$ satisfies the following equation (see, for example, Ref. 11):

$$w_0''(s) + \kappa_z(s)w_0(s) = \frac{1}{w_0^3(s)}, \quad (29)$$

and $\langle f(s) \rangle = S^{-1} \int_0^S f(s) ds$ denotes the average of the function $f(s)$ over one axial period of the system.

While Fig. 5 is computed for the specific periodic solenoidal focusing field with $S\sqrt{\kappa_z(s)} = a_0 + a_1 \cos(2\pi s/S)$,

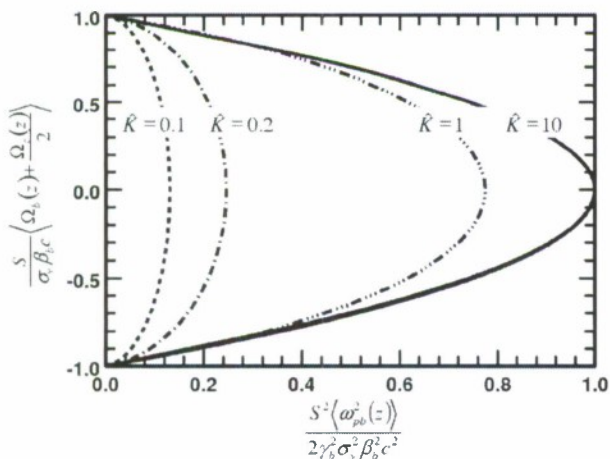


FIG. 5. Plot of the normalized angular frequency of beam rotation in the Larmor frame as a function of the effective self-field parameter for normalized perveances $\hat{K}=0.1, 0.2, 1$, and 10.

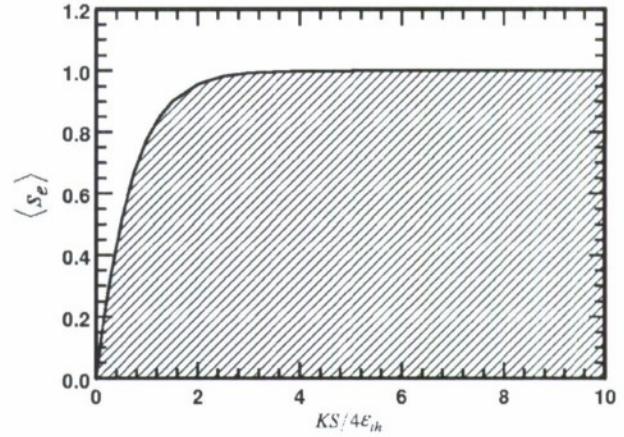


FIG. 6. Plot of the critical effective self-field parameter $\langle s_e \rangle$ as a function of $\hat{K} \equiv KS/4\epsilon_{th}$. The shaded region gives the parameter space for radial beam confinement.

where $a_0 = a_1 = 1.14$, we observe no change in Fig. 4 if we vary the values of a_0 and a_1 , provided that the vacuum phase advance σ_v of the magnetic field does not change. For $a_1 = 0$, Fig. 5 recovers the thermal beam equilibrium in a uniform magnetic focusing field (see Ref. 5).

As shown in Fig. 5, each curve at a particular value of \hat{K} has two branches. For any value of the effective self-field parameter $\langle s_e \rangle$ below a critical value, a confined beam can rotate at two angular frequencies, either positive or negative relative to the Larmor frame. For each value of \hat{K} , the maximum (critical) value of the effective self-field parameter for a confined beam is reached when the beam does not rotate relative to the Larmor frame. In Fig. 6, the critical effective self-field parameter $\langle s_e \rangle$ is plotted as a function of $\hat{K} \equiv KS/4\epsilon_{th}$. The parameter space for radial beam confinement is indicated by the shaded region in Fig. 6.

IV. CONCLUSIONS

We presented a warm-fluid equilibrium beam theory of a new thermal charged-particle beam propagating through a periodic solenoidal focusing field. We solved the warm-fluid beam equations in the paraxial approximation. We derived the rms beam envelope equation and solved it numerically. We also derived the self-consistent Poisson equation, governing the beam density and potential distributions. We computed the density profiles numerically for high-intensity and low-intensity beams. We investigated the temperature effects in such beams. We found that the thermal beam equilibrium has a density profile with a smooth edge and a uniform temperature profile across the beam cross section. Finally, we discussed the radial confinement of the beam.

ACKNOWLEDGMENTS

The authors would like to thank Dr. Ronak Bhatt for helpful discussions.

This research was supported by the U.S. Department of Energy, Office of High-Energy Physics, Grant No. DE-

FG02-95ER40919, and Air Force Office of Scientific Research, Grant No. FA9550-06-1-0269.

- ¹I. M. Kapchinsky and V. V. Vladimirovsky, in *Proceedings of the Conference on High Energy Accelerators and Instrumentation* (CERN, Geneva, 1959), p. 274.
- ²C. Chen, R. Pakter, and R. C. Davidson, *Phys. Rev. Lett.* **79**, 225 (1997).
- ³R. C. Davidson and C. Chen, *Part. Accel.* **59**, 175 (1998).
- ⁴R. C. Davidson and H. Qin, *Physics of Intense Charged Particle Beams* (Imperial College Press, Singapore, 2001), p. 242.
- ⁵R. C. Davidson, *Physics of Nonneutral Plasmas* (Addison-Wesley, Reading, 1990).
- ⁶J. Zhou, K. R. Samokhvalova, and C. Chen, *AIP Conf. Proc.* **877**, 489 (2006).
- ⁷J. Zhou, K. R. Samokhvalova, and C. Chen, "Adiabatic thermal equilibrium theory for periodically focused axisymmetric intense beam propagation," *Phys. Plasmas* (to be published).
- ⁸R. C. Davidson, P. Stoltz, and C. Chen, *Phys. Plasmas* **4**, 3710 (1997).
- ⁹K. R. Samokhvalova, J. Zhou, and C. Chen, *AIP Conf. Proc.* **877**, 445 (2006).
- ¹⁰F. J. Sacherer, *IEEE Trans. Nucl. Sci.* **18**, 1105 (1971).
- ¹¹M. Reiser, *Theory and Design of Charged Particle Beams* (Wiley, New York, 1994), p. 223.

A high-brightness circular charged-particle beam system

T. Bemis,^{a)} R. Bhatt,^{b)} C. Chen, and J. Zhou^{c)}

Plasma Science and Fusion Center, Massachusetts Institute of Technology, Cambridge, Massachusetts 02139, USA

(Received 21 September 2007; accepted 31 October 2007; published online 15 November 2007)

A method is presented for the design of a high-brightness nonrelativistic circular beam system including a charged-particle emitting diode, a diode aperture, a circular beam tunnel, and a focusing magnetic field that matches the beam from the emitter to the beam tunnel. The applied magnetic field is determined by balancing the forces throughout the gun and transport sections of the beam system. The method is validated by three-dimensional simulations. © 2007 American Institute of Physics. [DOI: 10.1063/1.2815938]

High-brightness, space-charge-dominated charged-particle beams are of great interest because of their applications in particle accelerators, x-ray sources, vacuum electron devices, and material processing such as ion implantation. When the beam brightness increases, the beam becomes space-charge dominated. In the space-charge-dominated regime, the beam equilibrium is characterized by a beam core with a transversely uniform density distribution and a sharp edge where the beam density falls rapidly to zero in a few Debye lengths. For particle accelerators, high-brightness, space-charge-dominated charged-particle beams provide high beam intensities. For medical accelerators and x-ray sources, they provide higher and more precise radiation dosage. For ion implantation, they improve deposition uniformity and speed. For vacuum electron devices, they permit high-efficiency, low-noise operation with depressed collectors.

An essential component of charged-particle beam systems is the beam generation and acceleration diode, consisting of a charged-particle emitter and a gap across which one or more electrostatic potential differences are maintained. Conventionally, Pierce-type diodes¹ with or without a grid are employed to produce the Child-Langmuir emission.^{2,3} Compression is often used in Pierce-type diodes in order to generate the desired beam radius. Scrapers are often used also to chop off the nonuniform beam edges.⁴ The grid, compression, and scrapers introduce a mismatch into the beam systems and degrade beam brightness. An important aspect of charged-particle beam system design is the transition from the diode to the beam focusing tunnel. While the rigid-rotor equilibrium is well known for a uniform solenoidal focusing field,⁵ a perfect matching of a circular beam from a Pierce-type diode into the rigid-rotor equilibrium has not been reported until this letter.

In this letter, a method is presented for the generation, acceleration, focusing, and collection of a high-brightness, space-charge-dominated circular charged-particle beam. As illustrated in a cross sectional view shown in Fig. 1, the beam system comprises⁶

- (1) a flat circular emitter which emits charged particles,

- (2) a diode with one electrode at the emitter and at least one additional electrode which accelerates the charged particles,
- (3) a beam tunnel which is connected electrically to at least one of the additional electrodes,
- (4) an applied axisymmetric magnetic field for charged-particle beam focusing, and
- (5) a depressed collector which collects the charged-particle beam.

The emitter consists of a flat, circular disk. A circular charged-particle beam is emitted from the emitter with a uniform density. The current emission is space-charge limited, obeying the Child-Langmuir law. The electrodes and applied axisymmetric magnetic field are designed to preserve the beam cross section in the accelerating section. The method for designing the required electrodes and applied axisymmetric magnetic field is described as follows.

As a first step, the beam dynamics is modeled with a three-dimensional OMNITRAK simulation with no applied magnetic field. This provides the electric field database which is used to compute iteratively the applied magnetic field required to preserve the cross section of the charged-particle beam at the accelerating and transport sections.

As a second step, an estimate of the required applied magnetic field is obtained by balancing all of the radial forces on the charged particles on a line whose radius corresponds to the root-mean-square (rms) radius of the emitter. The line starts at the cathode disk and continues through the anode aperture.

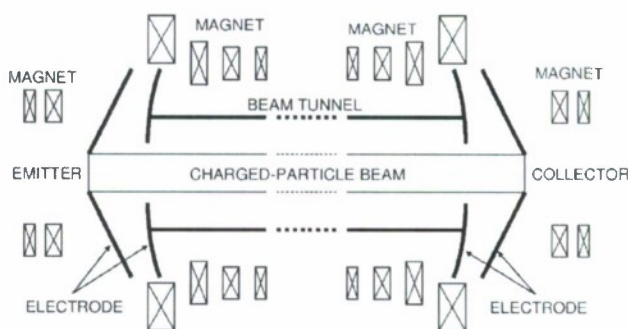


FIG. 1. Cross sectional view of a high-brightness circular charged-particle beam system.

^{a)}Present address: Beam Power Technology, Inc., 150 Lincoln Street, Suite 3C, Boston, MA 02111.

^{b)}Present address: 18115 Tawnas Way Lane, Cypress, TX 77429.

^{c)}Electronic mail: jea_zhou@psfc.mit.edu

For a thin charged-particle beam, all forces are proportional to the radial displacement, and an expression for the required magnetic field can be derived to achieve the radial force balance at any radius in the beam core. An applied axisymmetric magnetic field is expressed in terms of the vector potential in a cylindrical coordinate system as

$$\mathbf{B} = \hat{\mathbf{e}}_z \frac{1}{r} \frac{\partial}{\partial r} (r A_\theta) - \hat{\mathbf{e}}_r \frac{\partial A_\theta}{\partial z}. \quad (1)$$

In the thin-beam approximation,

$$\mathbf{B} = B_z(0, z) \hat{\mathbf{e}}_z - \frac{1}{2} \frac{\partial B_z(0, z)}{\partial z} r \hat{\mathbf{e}}_r. \quad (2)$$

Inspection of Eqs. (1) and (2) gives

$$A_\theta(r, z) = \frac{r}{2} B_z(0, z). \quad (3)$$

The conservation of canonical angular momentum yields the expression for the azimuthal velocity

$$v_\theta(r, z) = -\frac{q}{2m} [B_z(0, z) - B_z(0, 0)] r, \quad (4)$$

where use has been made of $v_\theta(r, 0) = 0$ at the emitter, and q and m are the particle charge and rest mass, respectively. The radial force balance equation is

$$\frac{q E_r(r, z)}{m} = -\frac{v_\theta^2(r, z)}{r} - \frac{q}{m} v_\theta(r, z) B_z(r, z). \quad (5)$$

Substituting Eq. (4) into Eq. (5) yields

$$\frac{q E_r(r, z)}{m} = \frac{q^2 r}{4m^2} B_z^2(0, z), \quad (6)$$

where use has been made of the approximation $B_z(r, z) = B_z(0, z)$ and the boundary condition $B_z(0, 0) = 0$. Equation (6) produces a relationship between E_r/r and $B_z(0, z)$.

By iterating the second step described above, better estimates of the required magnetic field are obtained. Typically, results converge after two or three iterations. As an illustrative example, Fig. 2 shows the final results of OMNITRAK simulations with a grid with $\Delta x = \Delta y = 0.05$ mm and $\Delta z = 0.1$ mm for a circular electron beam which is emitted from an emitter (cathode) with a radius of 1.52 mm, a current of 0.11 A, a cathode-to-anode distance of 4.11 mm at radius $r = 1.52$ mm. The diode voltage is 2300 V. In Fig. 2, the electrodes at the cathode and the anode are equipotential surfaces which are analytically computed⁷⁻⁹ to yield a Child-Langmuir flow^{2,3} in the absence of the anode aperture. A circular aperture at the anode is chosen, and it has a radius of 1.8 mm. A larger circular beam tunnel with a radius of 6.0 mm is connected to the anode. The total axial length of the system is 10 mm.

Figure 3 shows plots of E_r vs z at $r = 1.0$ mm and $B_z(0, z)$ vs z from the OMNITRAK simulations after two iterations. The radial electric field vanishes at the emitter (i.e., at $z = 0$), achieves a maximum magnitude at $z = 4.11$ mm, and then approaches to a constant value well inside the beam tunnel. The applied axial magnetic field at the emitter vanishes, increases to 640 G at the aperture, and then falls to about 160 G well inside the beam tunnel. In the simulation, Eq. (6) is exactly satisfied for all the electrons on the rms beam radius, and approximately satisfied for the electrons not at the rms beam

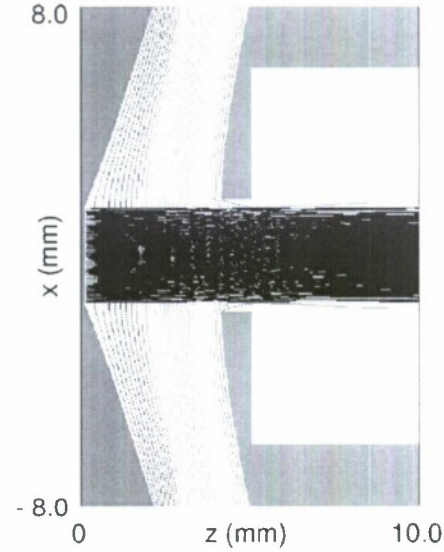


FIG. 2. (Color online) OMNITRAK simulation of the dynamics of an electron beam emitted from a flat circular cathode with a radius of 1.52 mm and a current of 0.11 A in an optimized magnetic field. Here, the cathode-to-anode distance is 4.11 mm at $r = 1.52$ mm, the circular anode aperture has a radius of 1.8 mm, and the beam tunnel has a radius of 6.0 mm. The diode voltage is 2300 V.

radius. The difference in the electric and applied magnetic forces in Eq. (6) results in less than 2% deviations of the electron radii from their initial values. Figure 4 shows the electron distribution in the phase plane (x, y) at $z = 8$ mm. The beam distribution maintains transverse uniformity. Indeed, the normalized fourth moment $\langle r^4 \rangle / \langle r^2 \rangle^2$ which is equal to 4/3 for a transversely uniform density distribution, remains 4/3 within $\pm 1\%$. The outer beam radius remains the same as the emitter radius within 1%–3%. At $z = 8$ mm, the normalized angular rotation velocity is $\omega_b = \langle x'y' \rangle / \langle y^2 \rangle = -0.0244$ rad/mm, and the unnormalized rms thermal emittances in the x - and y -directions are $\epsilon_x^{\text{th}} \equiv \sqrt{\langle x^2 \rangle \langle (x' - \omega_b y)^2 \rangle} = 1.96$ mm mrad and $\epsilon_y^{\text{th}} \equiv \sqrt{\langle y^2 \rangle \langle (y' + \omega_b x)^2 \rangle} = 1.96$, respectively, which correspond to a normalized rms thermal emittance of $\epsilon_n^{\text{th}} \equiv \gamma_b \beta_b \epsilon_x^{\text{th}} \equiv \beta_b \epsilon_x^{\text{th}} = 0.186$ mm mrad. Adding this (numerical) emittance to the intrinsic normalized rms emittance of 0.33 mm mrad for a thermionic cathode of radius 1.52 mm predicts a normalized thermal emittance of $\epsilon_n^{\text{actual}} \leq 0.38$ mm mrad for the actual electron beam.

Because the beam is in laminar flow, a depressed collector is designed using the same geometry as the charged-particle emitting diode, where the circular emitting disk is

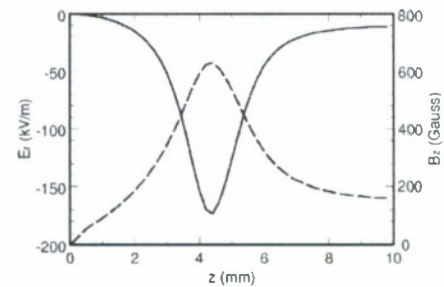


FIG. 3. Plots of E_r vs z at $r = 1$ mm (solid curve) and $B_z(0, z)$ vs z (dashed curve) from the OMNITRAK simulations after two iterations.

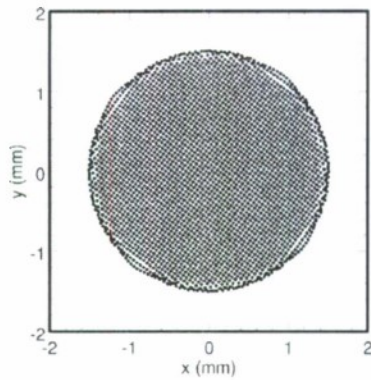


FIG. 4. Plot of the electron distribution at $z=8$ mm in the phase plane (x,y) .

the beam collecting surface, and diode voltage is slightly lower (i.e., a fraction of a percent lower) than the diode voltage but has a negative bias. Such a depressed collector yields a collection efficiency of nearly 100%.

To summarize, a high-brightness, space-charge-dominated circular charged-particle beam system was de-

scribed. The method was presented for the system, including the beam generation, acceleration, focusing, and collection processes. The method was validated by three-dimensional simulations.

This research was supported by MIT Deshpande Center of Technological Innovations, Department of Energy, Grant No. DE-FG02-95-ER40919, and Air Force Office of Scientific Research, Grant No. FA9550-06-1-0269.

¹J. R. Pierce, *Theory and Design of Electron Beams*, 2nd ed. (Van Nostrand, New York, 1954), p. 157.

²C. D. Child, *Phys. Rev.* **32**, 492 (1911).

³L. Langmuir, *Phys. Rev.* **21**, 419 (1923).

⁴E. Henestroza, S. Eylon, P. K. Roy, S. S. Yu, F. M. Bieniosek, D. B. Shuman, and W. L. Waldron, *Phys. Rev. ST Accel. Beams* **8**, 052801 (2005).

⁵R. C. Davidson, *Physics of Nonneutral Plasmas* (Addison-Wesley, Reading, MA, 1990), p. 37.

⁶T. Bemis, R. J. Bhatt, C. Chen, and J. Zhou, U.S. Patent Application No. 60/865,895 (15 November 2006).

⁷D. E. Radley, *J. Electron. Control* **4**, 125 (1957).

⁸R. Bhatt and C. Chen, *Phys. Rev. ST Accel. Beams* **8**, 014201 (2005).

⁹R. Bhatt, T. Bemis, and C. Chen, *IEEE Trans. Plasma Sci.* **34**, 187 (2006).

Adiabatic thermal equilibrium theory for periodically focused axisymmetric intense beam propagation

Jing Zhou, Ksenia R. Samokhvalova, and Chiping Chen
*Plasma Science and Fusion Center, Massachusetts Institute of Technology,
 Cambridge, Massachusetts 02139, USA*

(Received 22 August 2007; accepted 7 January 2008; published online 7 February 2008)

An adiabatic equilibrium theory is presented for an intense, axisymmetric charged-particle beam propagating through a periodic solenoidal focusing field. The thermal beam distribution function is constructed based on the approximate and exact invariants of motion, i.e., a scaled transverse Hamiltonian and the angular momentum. The approximation of the scaled transverse Hamiltonian as an invariant of motion is validated analytically for highly emittance-dominated beams and highly space-charge-dominated beams, and numerically tested to be valid for cases in between with moderate vacuum phase advances ($\sigma_v < 90^\circ$). The beam root-mean-square (rms) envelope equation is derived, and the self-consistent nonuniform density profile is determined. Other statistical properties such as flow velocity, temperature, total emittance and rms thermal emittance, equation of state, and Debye length are discussed. Numerical examples are presented, illustrating the effects of the beam perveance, emittance, and rotation on the beam envelope and density distribution. Good agreement is found between theory and a recent high-intensity beam experiment performed at the University of Maryland Electron Ring [S. Bernal, B. Quinn, M. Reiser, and P. G. O'Shea, *Phys. Rev. ST Accel. Beams* **5**, 064202 (2002)]. © 2008 American Institute of Physics.
 [DOI: 10.1063/1.2837891]

I. INTRODUCTION

A fundamental understanding of the kinetic equilibrium and stability properties of high-intensity electron and ion beams in periodic focusing fields plays a central role in high energy density physics research, in the design and operation of particle accelerators, such as storage rings, rf and induction linacs, and high-energy colliders, as well as in the design and operation of vacuum electron devices, such as klystrons and traveling-wave tubes with periodic permanent magnet (PPM) focusing. For such systems, beams of high quality (i.e., low emittance, high current, small energy spread, and low beam loss) are required. Exploration of equilibrium states of charged-particle beams and their stability properties is critical to the advancement of basic particle accelerator physics.

Several kinetic equilibria have been discovered for periodically focused intense charged-particle beams. Well-known equilibria for periodically focused intense beams include the Kapchinskij–Vladimirskij (KV) equilibrium^{1–3} in an alternating-gradient quadrupole magnetic focusing field and the periodically focused rigid-rotor Vlasov equilibrium⁴ in a periodic solenoidal magnetic focusing field. Both beam equilibria^{1–4} have a singular (δ -function) distribution in the four-dimensional phase space. Such a δ -function distribution gives a uniform density profile across the beam in the transverse directions, and a transverse temperature profile that peaks on axis and decreases quadratically to zero on the edge of the beam. Because of the singularity in the distribution functions, both equilibria are not likely to occur in real physical systems and cannot provide realistic models for theoretical and experimental studies and simulations except for the zero-temperature limit. For example, the KV equilibrium

model cannot be used to explain the beam tails in the radial distributions observed in recent high-intensity beam experiments.⁵

In general, beams tend to relax to a thermal equilibrium in the transverse plane such that the temperature across the transverse beam cross section is uniform. A theoretical understanding of thermal equilibrium and stable transport is desirable. Kinetic and warm-fluid theories of a thermal equilibrium in a uniform magnetic focusing field have been studied in Ref. 3. A formal multiple scale analysis (a third-order averaging technique) has been applied to obtain an approximate periodically focused thermal equilibrium in periodic solenoidal and periodic quadrupole magnetic fields.⁶ Such an averaging procedure is expected to be valid for sufficiently small vacuum phase advances. The concept of adiabatic breathing of high-intensity charged-particle beam was proposed in Ref. 7. Recently, a warm-fluid equilibrium theory of a periodically focused intense charge-particle beam⁸ has been developed under the assumption of the adiabatic equation of state. In this paper, a kinetic thermal equilibrium in a periodic magnetic focusing field is developed to provide more insight into the equilibrium properties of a periodically focused thermal beam.

We present a kinetic theory describing an adiabatic thermal equilibrium of an intense charged-particle beam propagating through a periodic solenoidal magnetic focusing field. For continuous beams with long pulses, the longitudinal energy spread is small such that the longitudinal motion can be treated as “cold” and decoupled from the transverse motion, which is kept nonrelativistic. The beam pulsates in transverse directions adiabatically like an ideal gas in an adiabatic process, in which the invariant is the product of the transverse

temperature and an effective beam area. It differs from the usual thermal equilibrium in which the temperature is kept constant.^{9,10} In the present work, the Hamiltonian for single-particle motion is analyzed to find the approximate and exact invariants of motion, i.e., a scaled transverse Hamiltonian (nonlinear space charge included) and the angular momentum, from which the beam equilibrium distribution is constructed. The approximation of the scaled transverse Hamiltonian as an invariant of motion is validated analytically for highly emittance-dominated beams and highly space-charge-dominated beams, and numerically tested to be valid for cases in between with moderate vacuum phase advances ($\sigma_v < 90^\circ$). The beam envelope and emittances are determined self-consistently with the beam equilibrium distribution. Because the distribution function has a Maxwell-Boltzmann form, it solves not only the Vlasov equation but also the Fokker-Planck equation. It is expected to be stable in a similar manner as the beam thermal equilibrium in a smooth-focusing approximation.^{9,10}

The paper is organized as follows. In Sec. II, the theoretical model is introduced. Exact and approximate constants of motion are found for the single-particle Hamiltonian in the paraxial approximation, and the equilibrium distribution is constructed. In Sec. III, the statistical properties of the beam equilibrium, such as the beam envelope equation, emittances, and beam temperature, are discussed. In Sec. IV, the numerical calculations of the beam density and potential are presented. In Sec. V, the comparison between our theory and a recent experiment from University of Maryland Electron Ring (UMER)⁵ is discussed. Finally, the paper is concluded in Sec. VI.

II. BEAM EQUILIBRIUM DISTRIBUTION

We consider a continuous, intense charged-particle beam propagating with constant axial velocity $\beta_b c \mathbf{e}_z$ through an applied periodic solenoidal magnetic focusing field. The periodic solenoidal magnetic focusing field is described by

$$\mathbf{B}^{\text{ext}} = B_z(s) \mathbf{e}_z - \frac{1}{2} \frac{dB_z(s)}{ds} (x \mathbf{e}_x + y \mathbf{e}_y), \quad (1)$$

where $s=z$ is the axial coordinate, $B_z(s)=B_z(s+S)$ is the axial magnetic field, and S is the fundamental periodicity length of the focusing field. The condition $S \gg r_{\text{brms}}$ is assumed, where r_{brms} is the characteristic radius of the rms beam envelope.

The single-particle Hamiltonian can be written as $H = [m^2 c^4 + (c\mathbf{P} - q\mathbf{A})^2]^{1/2} + q\phi^{\text{self}}$, where the canonical momentum \mathbf{P} is related to the mechanical momentum \mathbf{p} by $\mathbf{P} = \mathbf{p} + q\mathbf{A}/c$, $\mathbf{A} = \mathbf{A}^{\text{ext}} + \mathbf{A}^{\text{self}}$ is the vector potential for the total magnetic field, \mathbf{A}^{self} is the vector potential for the self-magnetic field, $\mathbf{A}^{\text{ext}}(x, y, s) = B_z(s)(-y \mathbf{e}_x + x \mathbf{e}_y)/2$ is the vector potential for the applied magnetic field, ϕ^{self} is the scalar potential for self-electric field, m and q are particle rest mass and charge, and c is the speed of light in vacuum.

In the paraxial approximation, we assume $\nu/\gamma_b^3 \beta_b^2 \ll 1$, where $\nu \equiv q^2 N_b / mc^2$ is the Budker parameter³ of the beam, $N_b = \int^\infty n_b(x, y) dx dy = \text{const}$ is the number of particles per unit axial length, and $\gamma_b = (1 - \beta_b^2)^{-1/2}$ is the relativistic mass factor. The axial energy is approximately $\gamma_b mc^2$

$\equiv (m^2 c^4 + c^2 P_z^2)^{1/2}$. Because $\nu/\gamma_b^3 \beta_b^2 \ll 1$, the longitudinal particle motion can be decoupled from the transverse particle motion, and the total Hamiltonian for single-particle motion is approximated by $H \approx \gamma_b mc^2 + H_\perp$. Here, the longitudinal Hamiltonian $H_\parallel = \gamma_b mc^2$ is a constant and the normalized transverse Hamiltonian $\hat{H}_\perp = H_\perp / \gamma_b m \beta_b^2 c^2$ is expressed as

$$\hat{H}_\perp(x, y, P_x, P_y, s) = \frac{1}{2} \{ [\hat{P}_x + \sqrt{\kappa_z(s)} y]^2 + [\hat{P}_y - \sqrt{\kappa_z(s)} x]^2 \} + \hat{\phi}^{\text{self}}, \quad (2)$$

where $\sqrt{\kappa_z(s)} \equiv q B_z(s) / 2 \gamma_b m \beta_b c^2$ is a measure of the strength of periodic solenoidal magnetic field, $\hat{\mathbf{P}}_\perp = \mathbf{P}_\perp / \gamma_b m \beta_b c$, $\hat{\phi}^{\text{self}} = q \phi^{\text{self}} / \gamma_b^3 m \beta_b^2 c^2 = K \phi^{\text{self}} / 2 q N_b$, and $K \equiv 2 q^2 N_b / \gamma_b^3 m \beta_b^2 c^2$ is the beam perveance. The scalar and vector potentials for the self-electric and self-magnetic fields satisfy $\nabla_\perp^2 \phi^{\text{self}} = -4 \pi q n_b(x, y, s)$, $\nabla_\perp^2 \mathbf{A}^{\text{self}} = -4 \pi \beta_b c q n_b(x, y, s) \mathbf{e}_z$, and $\mathbf{A}^{\text{self}} = A_z^{\text{self}} \mathbf{e}_z = \beta_b \phi^{\text{self}} \mathbf{e}_z$. The associated equations of motion with the Hamiltonian Eq. (2) are

$$\frac{d^2 x}{ds^2} - 2 \sqrt{\kappa_z(s)} \frac{dy}{ds} - \frac{d \sqrt{\kappa_z(s)}}{ds} y + \frac{\partial \hat{\phi}^{\text{self}}}{\partial x} = 0, \quad (3)$$

$$\frac{d^2 y}{ds^2} + 2 \sqrt{\kappa_z(s)} \frac{dx}{ds} + \frac{d \sqrt{\kappa_z(s)}}{ds} x + \frac{\partial \hat{\phi}^{\text{self}}}{\partial y} = 0. \quad (4)$$

In order to simplify the transverse Hamiltonian $\hat{H}_\perp(x, y, P_x, P_y, s)$, we perform a two-step canonical transformation. The first step is to transform from the Cartesian coordinates into the Larmor frame which rotates with one-half of the cyclotron frequency relative to the laboratory frame. The second step is a Courant-Snyder type of transformation. The first transformation uses the second type of the generating function

$$\tilde{F}_2(x, y; \tilde{P}_x, \tilde{P}_y, s) = [x \cos \varphi(s) - y \sin \varphi(s)] \tilde{P}_x + [x \sin \varphi(s) + y \cos \varphi(s)] \tilde{P}_y, \quad (5)$$

where $\varphi(s) = \int_0^s \sqrt{\kappa_z(s)} ds$. The transformation is

$$\tilde{x} = \frac{\partial \tilde{F}_2}{\partial \tilde{P}_x} = x \cos \varphi(s) - y \sin \varphi(s), \quad (6)$$

$$\tilde{y} = \frac{\partial \tilde{F}_2}{\partial \tilde{P}_y} = x \sin \varphi(s) + y \cos \varphi(s), \quad (7)$$

$$P_x = \frac{\partial \tilde{F}_2}{\partial x} = \tilde{P}_x \cos \varphi(s) + \tilde{P}_y \sin \varphi(s), \quad (8)$$

$$P_y = \frac{\partial \tilde{F}_2}{\partial y} = -\tilde{P}_x \sin \varphi(s) + \tilde{P}_y \cos \varphi(s). \quad (9)$$

The transverse Hamiltonian after the first transformation is expressed as

$$\begin{aligned}\bar{H}_\perp(\bar{x}, \bar{y}, \bar{P}_x, \bar{P}_y, s) &= \hat{H}_\perp(x, y, P_x, P_y, s) + \frac{\partial \bar{F}_2}{\partial s} \\ &= \frac{1}{2}[\bar{P}_x^2 + \bar{P}_y^2 + \kappa_z(s)(\bar{x}^2 + \bar{y}^2)] + \hat{\phi}^{\text{self}}(\bar{x}, \bar{y}, s).\end{aligned}\quad (10)$$

Note that $(\partial^2/\partial x^2 + \partial^2/\partial y^2)\hat{\phi}^{\text{self}}(x, y, s) = (\partial^2/\partial \bar{x}^2 + \partial^2/\partial \bar{y}^2)\hat{\phi}^{\text{self}}(\bar{x}, \bar{y}, s)$. The equation of motion associated with the transverse Hamiltonian in Eq. (10) is

$$\frac{d^2 \bar{x}}{ds^2} + \kappa_z(s)\bar{x} + \frac{\partial \hat{\phi}^{\text{self}}}{\partial \bar{x}} = 0, \quad (11)$$

$$\frac{d^2 \bar{y}}{ds^2} + \kappa_z(s)\bar{y} + \frac{\partial \hat{\phi}^{\text{self}}}{\partial \bar{y}} = 0. \quad (12)$$

The second canonical transformation uses the second type of the generating function

$$\begin{aligned}\bar{F}_2(\bar{x}, \bar{y}; \bar{P}_x, \bar{P}_y, s) &= \frac{\bar{x}}{w(s)} \left[\bar{P}_x + \frac{1}{2} \frac{dw(s)}{ds} \bar{x} \right] \\ &+ \frac{\bar{y}}{w(s)} \left[\bar{P}_y + \frac{1}{2} \frac{dw(s)}{ds} \bar{y} \right],\end{aligned}\quad (13)$$

where $w(s)$ satisfies the differential equation

$$\frac{d^2 w(s)}{ds^2} + \kappa_z(s)w(s) - \frac{K}{2r_{\text{brms}}^2(s)}w(s) = \frac{1}{w^3(s)}, \quad (14)$$

and $r_{\text{brms}}(s)$ is the rms beam radius. It will be shown in Sec. III that the function $w(s)$ is related to the rms beam radius [see Eq. (29)]. The transformation is

$$\bar{x} = \frac{\partial \bar{F}_2}{\partial \bar{P}_x} = \frac{\bar{x}}{w(s)}, \quad (15)$$

$$\bar{y} = \frac{\partial \bar{F}_2}{\partial \bar{P}_y} = \frac{\bar{y}}{w(s)}, \quad (16)$$

$$\bar{P}_x = \frac{\partial \bar{F}_2}{\partial \bar{x}} = \frac{1}{w(s)} \left[\bar{P}_x + \bar{x} \frac{dw(s)}{ds} \right], \quad (17)$$

$$\bar{P}_y = \frac{\partial \bar{F}_2}{\partial \bar{y}} = \frac{1}{w(s)} \left[\bar{P}_y + \bar{y} \frac{dw(s)}{ds} \right]. \quad (18)$$

Using Eqs. (15)–(18), the transverse Hamiltonian is transformed into

$$\begin{aligned}\bar{H}_\perp(\bar{x}, \bar{y}, \bar{P}_x, \bar{P}_y, s) &= \frac{1}{2w^2(s)}[\bar{P}_x^2 + \bar{P}_y^2 + \bar{x}^2 + \bar{y}^2] + \hat{\phi}^{\text{self}}(\bar{x}, \bar{y}, s) \\ &+ \frac{K}{4r_{\text{brms}}^2(s)}w^2(s)(\bar{x}^2 + \bar{y}^2).\end{aligned}\quad (19)$$

The equations of motion associated with the Hamiltonian in Eq. (19) are

$$\frac{d\bar{x}}{ds} = \frac{\partial \bar{H}_\perp}{\partial \bar{P}_x} = \frac{\bar{P}_x}{w^2(s)}, \quad (20)$$

$$\frac{d\bar{y}}{ds} = \frac{\partial \bar{H}_\perp}{\partial \bar{P}_y} = \frac{\bar{P}_y}{w^2(s)}, \quad (21)$$

$$\frac{d\bar{P}_x}{ds} = -\frac{\partial \bar{H}_\perp}{\partial \bar{x}} = -\frac{\bar{x}}{w^2(s)} - \frac{\partial \hat{\phi}^{\text{self}}}{\partial \bar{x}} - \frac{K}{2r_{\text{brms}}^2(s)}w^2(s)\bar{x}, \quad (22)$$

$$\frac{d\bar{P}_y}{ds} = -\frac{\partial \bar{H}_\perp}{\partial \bar{y}} = -\frac{\bar{y}}{w^2(s)} - \frac{\partial \hat{\phi}^{\text{self}}}{\partial \bar{y}} - \frac{K}{2r_{\text{brms}}^2(s)}w^2(s)\bar{y}. \quad (23)$$

In order to construct a beam equilibrium distribution, we need to find constants of motion of the system. Two constants of motion can be found using the transverse Hamiltonian in Eq. (19). It is readily shown that the angular momentum P_θ is a constant of motion, i.e.,

$$\frac{dP_\theta}{ds} = 0. \quad (24)$$

In deriving Eq. (24), we have used Eqs. (20)–(23), and the axial symmetry property of the self-field potential, i.e., $\hat{\phi}^{\text{self}}$ is only a function of $\bar{r} = \sqrt{\bar{x}^2 + \bar{y}^2}$ and s .

We also find that the scaled transverse Hamiltonian for single-particle motion,

$$\bar{E} \equiv w^2(s)\bar{H}_\perp(\bar{x}, \bar{y}, \bar{P}_x, \bar{P}_y, s), \quad (25)$$

is an approximate invariant. The transverse Hamiltonian is a highly oscillating function. We use the periodic function $w^2(s)$ to scale the transverse Hamiltonian and to eliminate the oscillations such that the scaled transverse Hamiltonian is an approximate invariant with small residual oscillations. As will be discussed in Sec. IV, the small residual oscillations are numerically estimated to be a few percent. Using Eqs. (20)–(23), the derivative of the scaled transverse Hamiltonian can be evaluated, using

$$\begin{aligned}\frac{d\bar{E}}{ds} &= \frac{d}{ds} \left\{ \frac{1}{2}(\bar{x}^2 + \bar{y}^2 + \bar{P}_x^2 + \bar{P}_y^2) + w^2(s)\hat{\phi}^{\text{self}}(\bar{r}, s) \right. \\ &\quad \left. + \frac{Kw^4(s)}{4r_{\text{brms}}^2(s)}\bar{r}^2 \right\} \\ &= \frac{\partial}{\partial s} \left[w^2(s)\hat{\phi}^{\text{self}}(\bar{r}, s) + \frac{Kw^4(s)}{4r_{\text{brms}}^2(s)}\bar{r}^2 \right].\end{aligned}\quad (26)$$

It is readily shown that $d\bar{E}/ds$ is approximately zero in two limiting cases: (a) a highly space-charge-dominated beam with $SK/\epsilon_{\text{th}} \gg 1$ and (b) a highly emittance-dominated beam with $SK/\epsilon_{\text{th}} \rightarrow 0$, where ϵ_{th} is the thermal beam emittance defined later in Eq. (35). For a highly space-charge-dominated beam with $SK/\epsilon_{\text{th}} \gg 1$,

$$\phi_{\text{cold}}^{\text{self}}(\bar{r}, s) \equiv -\frac{Kw^2(s)}{4r_{\text{brms}}^2(s)}\bar{r}^2, \quad \text{for } r < \sqrt{2}r_{\text{brms}} \quad (27)$$

and $d\bar{E}/ds \equiv 0$. For a highly emittance-dominated beam with $SK/\varepsilon_{\text{th}} \rightarrow 0$, $\phi_{\text{emit}}^{\text{self}} \equiv 0$ and $d\bar{E}/ds = 0$. For cases in which the space-charge effect is comparable to the emittance effect, we will demonstrate $d\bar{E}/ds \equiv 0$ numerically in Sec. IV.

We choose the beam equilibrium distribution in the form similar to the Maxwell-Boltzmann distribution, i.e.,

$$f_b = C \exp[-\beta(\bar{E} - \omega_b \bar{P}_\theta)], \quad (28)$$

where C , β , and ω_b are constants. C is an integration constant, β is related to the beam emittance, and ω_b is the rotation frequency relative to the Larmor frame. Note that $\omega_b = 0$ for Brillouin flow and $\omega_b \neq 0$ for general flows in which there is magnetic flux on the emitter. Since \bar{P}_θ and \bar{E} are the constants of motion, the distribution function f_b defined in Eq. (28) is indeed a Vlasov equilibrium, i.e., $\partial f_b / \partial s = 0$.

III. STATISTICAL PROPERTIES

In this section, we will discuss the statistical properties of the thermal equilibrium developed in Sec. II, including the rms beam radius, rms emittance and thermal emittance, flow velocity, beam temperature, and beam density profile.

The distribution function described in Eq. (28) has the following statistical properties. First, the rms beam radius $r_{\text{brms}}^2(s) \equiv \langle x^2 + y^2 \rangle = N_b^{-1} \iint (x^2 + y^2) f_b d\bar{x} d\bar{y} d\bar{P}_x d\bar{P}_y$ can be evaluated to yield

$$r_{\text{brms}}^2(s) = \frac{2}{\beta(1 - \omega_b^2)} w^2(s) \equiv \frac{\varepsilon_T}{2} w^2(s), \quad (29)$$

where we have introduced the concept of the total emittance $\varepsilon_T \equiv 4\beta^{-1}(1 - \omega_b^2)^{-1}$. Substituting Eq. (29) into Eq. (14), we arrive at the rms envelope equation,

$$\frac{d^2 r_{\text{brms}}}{ds^2} + \kappa_z(s) r_{\text{brms}} - \frac{K}{2r_{\text{brms}}} = \frac{\varepsilon_T}{4r_{\text{brms}}^3}. \quad (30)$$

Second, the rms beam emittance of the beam equilibrium described in Eq. (28) is given in the Larmor frame by

$$\varepsilon_{\bar{x}\text{rms}} = \sqrt{\langle \bar{x}^2 \rangle \langle \bar{x}'^2 \rangle - \langle \bar{x} \bar{x}' \rangle^2} = \varepsilon_T / 4 = \text{const.} \quad (31)$$

Similarly, $\varepsilon_{\bar{y}\text{rms}} = \varepsilon_T / 4 = \text{const.}$ Note that Eq. (30) agrees with the well-known rms envelope equation in Ref. 10 with the interpretation of the total emittance in Eq. (29). As a third statistical property, in dimensional units, the average (macroscopic flow) transverse velocity of the beam equilibrium is given in the Larmor frame by

$$\begin{aligned} \mathbf{V}_\perp(r, s) &= [n_b w^2(s)]^{-1} \iint \mathbf{v}_\perp f_b d\bar{P}_x d\bar{P}_y \\ &= \frac{r'_{\text{brms}}(s)}{r_{\text{brms}}(s)} \beta_b c \mathbf{e}_r + \left[\frac{\varepsilon_T \omega_b}{2r_{\text{brms}}^2(s)} - \sqrt{\kappa_z(s)} \right] \beta_b c \mathbf{e}_\theta. \end{aligned} \quad (32)$$

As the fourth property, the beam equilibrium described by Eq. (28) has the transverse temperature profile (in dimensional units)

$$\begin{aligned} k_B T_\perp(s) &= [n_b w^2(s)]^{-1} \frac{m \gamma_b}{2} \int (\mathbf{v}_\perp - \mathbf{V}_\perp)^2 f_b d\bar{P}_x d\bar{P}_y \\ &= \frac{(1 - \omega_b^2) m \gamma_b \beta_b^2 c^2 \varepsilon_T^2}{8r_{\text{brms}}^2(s)}, \end{aligned} \quad (33)$$

where k_B is the Boltzmann constant. Note from Eq. (33) that the product $T_\perp(s) r_{\text{brms}}^2(s)$ is a conserved quantity ($d/ds = 0$) as the beam pulsates transversely; that is, the equation of state is

$$T_\perp(s) r_{\text{brms}}^2(s) = \text{const.} \quad (34)$$

Since $2\pi r_{\text{brms}}^2$ is a measure of the effective area of the beam, Eq. (34) is analogous to the equation of state for a two-dimensional adiabatic plasma.¹² As the fifth property, the thermal beam emittance in the Larmor frame is

$$\varepsilon_{\text{th}}^2 \equiv \frac{1}{\beta_b^2 c^2} \langle x^2 \rangle \langle (v_x - V_x)^2 \rangle = \frac{k_B T_\perp(s) r_{\text{brms}}^2(s)}{2 \gamma_b m \beta_b^2 c^2} = \text{const.} \quad (35)$$

It follows from Eqs. (31) and (35) that $\varepsilon_T^2 = 16\varepsilon_{\text{th}}^2 + 16\omega_b^2 \varepsilon_{\bar{x}\text{rms}}^2$, where the term $16\omega_b^2 \varepsilon_{\bar{x}\text{rms}}^2$ corresponds to the contribution from the average azimuthal motion in the Larmor frame to the total emittance. The rms envelope equation (30) can also be expressed as

$$\begin{aligned} \frac{d^2 r_{\text{brms}}(s)}{ds^2} - \frac{\Omega_b(s)}{\beta_b^2 c^2} [\Omega_b(s) + \Omega_c(s)] r_{\text{brms}}(s) - \frac{K}{2r_{\text{brms}}(s)} \\ = \frac{4\varepsilon_{\text{th}}^2}{r_{\text{brms}}^3(s)}, \end{aligned} \quad (36)$$

where $\Omega_b(s) = \omega_b \varepsilon_T \beta_b c / 2r_{\text{brms}}^2(s) - \Omega_c(s)/2$ and $\Omega_c(s) = qB_z(s) / \gamma_b m c$. Finally, the beam density profile is

$$\begin{aligned} n_b(r, s) &= w^{-2}(s) \iint f d\bar{P}_x d\bar{P}_y \\ &= \frac{4\pi C \varepsilon_{\text{th}}^2}{r_{\text{brms}}^2(s)} \exp \left\{ - \left[\frac{K}{2} + \frac{4\varepsilon_{\text{th}}^2}{r_{\text{brms}}^2(s)} \right] \frac{r^2}{4\varepsilon_{\text{th}}^2} \right. \\ &\quad \left. - \frac{q}{\gamma_b^2 k_B T_\perp(s)} \phi^{\text{self}}(r, s) \right\}, \end{aligned} \quad (37)$$

where the scalar potential for the self-electric field is determined by the Poisson equation

$$\frac{1}{r} \frac{\partial}{\partial r} \left(r \frac{\partial \phi^{\text{self}}}{\partial r} \right) = -4\pi q n_b(r, s). \quad (38)$$

It is worth noting that in the paraxial approximation, the total number of particles per unit length is kept constant, i.e., $N_b = \int_0^\infty n_b(r, s) 2\pi r dr$. This requires the on-axis self-electric potential $\phi^{\text{self}}(r=0, s)$ to vary as a function of the longitudinal distance, which will be determined numerically in Sec. IV.

It is readily shown that the thermal equilibrium distribution in Eq. (37) recovers the well-known thermal rigid-rotor equilibrium in a constant magnetic focusing field^{3,9} by setting $d^2 r_{\text{brms}} / ds^2 = 0$ in Eq. (36).

It is worth pointing out that because the derivation of the theory does not assume specific magnetic profile as defined

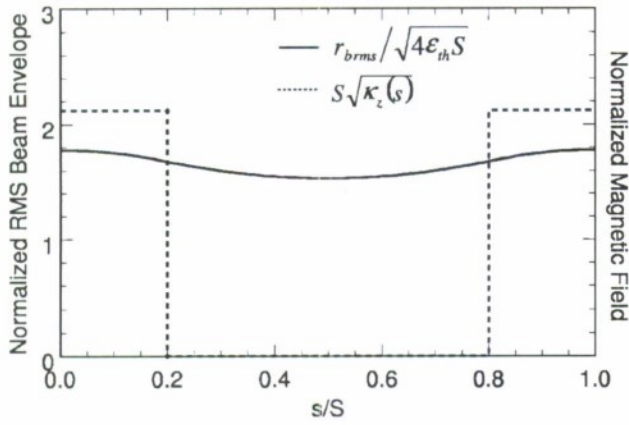


FIG. 1. Plots of the normalized axial magnetic field $S\sqrt{\kappa_z(s)}$ (dashed curve) and beam rms envelope $r_{\text{brms}}/\sqrt{4\epsilon_{\text{th}}S}$ (solid curve) versus the axial propagation distance s/S for a periodically focused adiabatic thermal beam equilibrium in an applied magnetic field described by the periodic step-function lattice in Eq. (39). Here, the choice of system parameters corresponds to $S\sqrt{\kappa_z(0)}=2.12$, $\eta=0.4$ ($\sigma_0=80^\circ$), $SK/4\epsilon_{\text{th}}=10.0$, and $\omega_b=0$.

in Eq. (1), it is valid not only for the periodic solenoid magnetic field but also for arbitrary varying solenoid magnetic field. Therefore, our results apply for the periodic focusing channel as well as for the matching section between the source and the periodic focusing channel. We will discuss numerical examples in a periodic focusing channel in Sec. IV and compare the theoretical results with the UMER⁵ experimental measurements in a short matching solenoid channel in Sec. V.

IV. NUMERICAL CALCULATIONS

In this section, we illustrate examples of adiabatic thermal beam equilibria in a periodic solenoidal focusing field and the temperature and beam rotation effects with numerical calculations. We also demonstrate numerically that $d\bar{E}/ds \approx 0$, as promised in Sec. II. A numerical module has been added to the PFB2D code¹³ to solve the rms envelope equation, (36) which determines the rms beam radius given the periodic solenoidal magnetic field and beam perveance, and Eqs. (37) and (38), which determine the beam density and scalar potential for the self-electric field.

We consider a thermal beam focused by a periodical solenoidal focusing magnetic field defined by the ideal periodic step function $\kappa_z(s)=\kappa_z(s+S)$ with

$$\sqrt{\kappa_z(s)} = \begin{cases} \sqrt{\kappa_{z0}} = \text{const}, & -\eta/2 < s/S < \eta/2, \\ 0, & \eta/2 < s/S < 1 - \eta/2, \end{cases} \quad (39)$$

where η is the filling factor of the solenoid magnetic field. In Fig. 1, the profile of the normalized axial magnetic field $S\sqrt{\kappa_z(s)}$ is plotted as a dashed curve, and the normalized rms beam envelope $\hat{r}_{\text{brms}} \equiv r_{\text{brms}}/\sqrt{4\epsilon_{\text{th}}S}$ for the thermal beam is plotted as a solid curve. The system parameters are $S\sqrt{\kappa_z(0)}=2.12$, $\eta=0.4$, $\hat{K} \equiv SK/4\epsilon_{\text{th}}=10$, and $\omega_b=0$. The vacuum and space-charge-depressed phase advances of the particle betatron oscillations over one lattice period are evaluated to be $\sigma_0 \equiv \epsilon_T \int_0^S ds/2r_{\text{brms0}}^2 = 78.9^\circ$ and σ

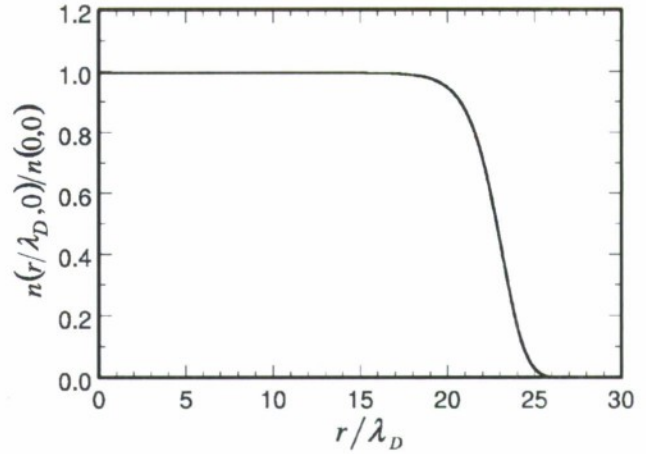


FIG. 2. Plot of the relative beam density versus r/λ_D at $s=0$ for the same beam and focusing field as in Fig. 1. Here, $r_{\text{brms}}=16.1\lambda_D$ and the beam densities are normalized to the peak density.

$=\epsilon_T \int_0^S ds/2r_{\text{brms}}^2 = 10.7^\circ$, respectively. Here, r_{brms0} is the rms equilibrium beam envelope when $K=0$.

In Fig. 2, the beam density relative to the peak density $n(r,s)/n(0,s)$ is plotted as a function of the radius relative to the Debye length at $s=0$ for the same beam as in Fig. 1. Here, the Debye length is defined as $\lambda_D \equiv \sqrt{\gamma_b^2 k_B T_\perp(0)/4\pi q^2 n_b(0,0)}$. The density has a flat top near the center of the beam and drops to zero within a few Debye lengths near the edge of the beam.

In Fig. 3, thermal beam density profiles are plotted for $\hat{K}=0.1, 1.0, 3.0$, and 10.0 with the focusing field in Eq. (39), $S\sqrt{\kappa_z(0)}=2.12$, and no beam rotation in the Larmor frame (i.e., $\omega_b=0$). Here, the beam density is normalized to the peak density n_0 of the beam with $SK/4\epsilon_{\text{th}}=10$. The beam density becomes a flat profile near the beam axis as the normalized perveance $\hat{K} \equiv SK/4\epsilon_{\text{th}}$ increases, i.e., as the beam current increases or the temperature decreases.

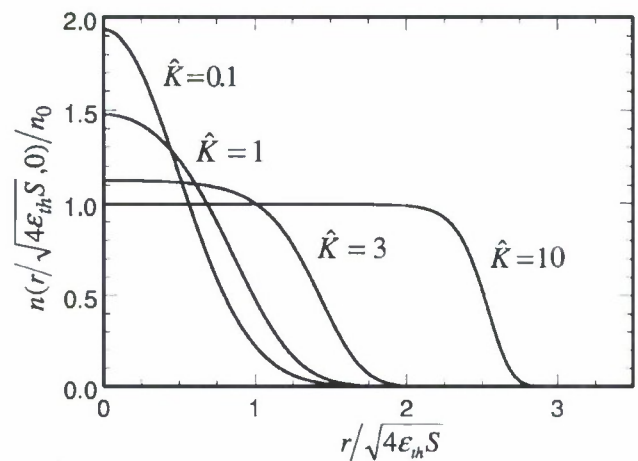


FIG. 3. Plot of the relative beam density versus $r/\sqrt{4\epsilon_{\text{th}}S}$ for several beams with $SK/4\epsilon_{\text{th}}=0.1, 1.0, 3.0$, and 10.0 , and other system parameters the same as in Fig. 1. Here, the beam densities are normalized to the peak density of the beam with $SK/4\epsilon_{\text{th}}=10.0$.

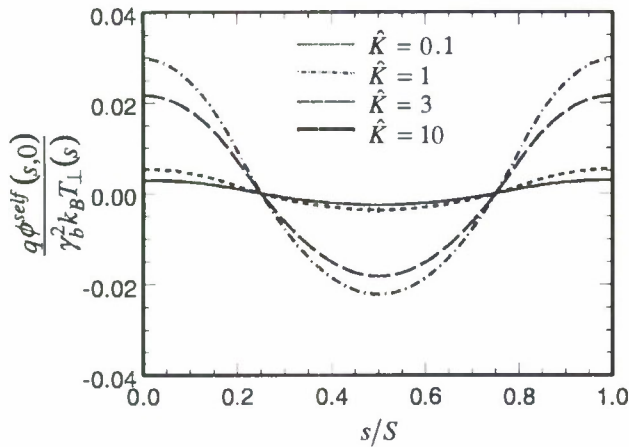


FIG. 4. Plot of the on-axis self-electric potential relative to the beam transverse thermal energy as a function of the propagation distance s/S for several beams with $SK/4\epsilon_{th}=0.1, 1.0, 3.0$, and 10.0 , and other system parameters the same as in Fig. 1.

The on-axis self-electric potential is determined numerically, requiring the total number of particles per unit length to be constant. For the detailed numerical method, please refer to Ref. 8. In Fig. 4, the computed on-axis self-electric potential energy relative to the beam transverse thermal energy, $q\phi^{self}(0,s)/\gamma_b^2 k_B T_{\perp}(s)$, is plotted as a function of s/S for $SK/4\epsilon_{th}=0.1, 1.0, 3.0$, and 10.0 , and other system parameters the same as in Fig. 1. The variation of the on-axis self-electric potential, i.e., the axial electric field, is indeed small.

To illustrate the influence of the beam rotation rate in the Larmor frame on the periodically focused thermal beam equilibrium, we plot the relative beam density profiles for three choices of the rotation parameter: $\omega_b=0, 0.9$, and 0.99 in Fig. 5. The system parameters are $S\sqrt{\kappa_z(0)}=2.12$ and $\hat{K}=10$. As the beam rotation increases, the beam radius in-

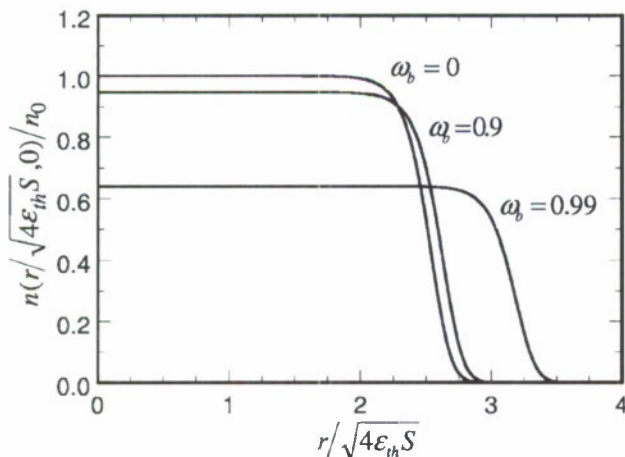


FIG. 5. Plot of the relative beam density versus $r/\sqrt{4\epsilon_{th}S}$ for several beams with $SK/4\epsilon_{th}=10.0$, $\omega_b=0, 0.9$, and 0.99 , and other system parameters the same as in Fig. 1. Here, the beam densities are normalized to the peak density of the beam with $\omega_b=0$.

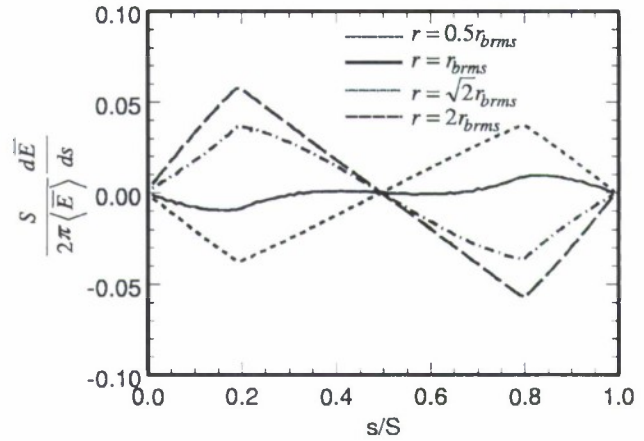


FIG. 6. Plot of the quantity $(S/2\pi\langle\bar{E}\rangle)d\bar{E}/ds$ versus s/S for the four radial displacements of the beam with system parameters $S\sqrt{\kappa_z(0)}=2.12$, $\eta=0.4$ ($\sigma_0=80^\circ$), $SK/4\epsilon_{th}=1.0$, and $\omega_b=0$.

creases, and the peak density at the beam axis decreases. However, the Debye length is intact as the beam rotation rate varies.

Finally, we demonstrate the approximate invariant of the scaled transverse Hamiltonian as defined in Eq. (25) for the cases $SK/\epsilon_T \rightarrow 1$. Instead of showing $d\bar{E}/ds \approx 0$ for each single particle, which requires very intensive numerical calculations, we demonstrate, by numerical calculations, that the scaled transverse Hamiltonian \bar{E} is slowly varying at a few radial displacements. In Fig. 6, the quantity $(S/2\pi\langle\bar{E}\rangle)d\bar{E}/ds$ is plotted as a function of s for various radial displacements $r=0.5r_{brms}$, r_{brms} , $\sqrt{2}r_{brms}$, and $2r_{brms}$ with other system parameters $\sigma_0=80^\circ$, $\hat{K}=1$, and $\omega_b=0$. Here, $\langle\bar{E}\rangle \equiv n_b^{-1} \iint \bar{E} f_b d\bar{P}_x d\bar{P}_y = \frac{1}{2}(\bar{r}^2 + \epsilon_T/2) + w^2(s)\phi^{self}(\bar{r}, s) + [Kw^4(s)/4r_{brms}^2(s)]\bar{r}^2$ is the scaled transverse Hamiltonian averaged over the particles located at the same radial displacement. Indeed, a maximum value of $|(S/2\pi\langle\bar{E}\rangle)d\bar{E}/ds| = 0.06$, which is achieved at $s/S=0.2$ and 0.8 , assures that $d\bar{E}/ds \approx 0$ in the paraxial approximation.

V. COMPARISON BETWEEN THEORY AND EXPERIMENT

In this section, we compare the present adiabatic thermal beam equilibrium theory with experimental measurements. The system is a 5 keV electron beam focused by a short solenoid magnetic in one of the experiments of UMER.⁵ In Ref. 5, the electron beam was generated by a gridded gun and exited the gun through an anode aperture at $s=0$. Bell-shaped beam density profiles were imaged by a fluorescent screen while the detailed velocity space distribution was not accessible. The bell-shaped beam density profile and the change of the beam density shape as the beam propagates have not been well understood theoretically using previous equilibrium theories, such as the KV beam equilibrium.

Using our adiabatic thermal beam equilibrium theory, we replicate the beam density profiles at different axial distances in good agreement with the experimental measurements. Our

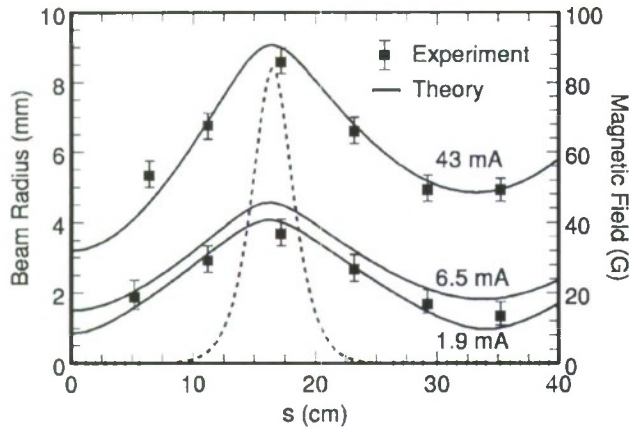


FIG. 7. Plots of calculated beam radius $R \equiv \sqrt{2}r_{\text{brms}}$ (solid curves) for three 5 keV electron beams with currents (emittances): 43 mA ($4\epsilon_{\text{rms}} = 71$ mm-mrad), 6.5 mA ($4\epsilon_{\text{rms}} = 30$ mm-mrad), and 1.9 mA ($4\epsilon_{\text{rms}} = 20$ mm-mrad). The dotted curves are the available experimental measurement for two beams: 43 mA ($4\epsilon_{\text{rms}} = 71$ mm-mrad) and 1.9 mA ($4\epsilon_{\text{rms}} = 20$ mm-mrad). The on-axis magnetic field is shown as a dashed curve.

equilibrium theory is applicable to this experiment from the anode aperture to a distance prior to wave breaking initiated by high-order density distribution fluctuations induced by a pressure force at the anode aperture. Wave breaking¹⁴ occurs at about one-quarter of plasma wavelength, which is about 30 cm in this example. Our equilibrium theory cannot explain the density distribution distortion in the present form, but it will be possible to develop a perturbation theory based on the equilibrium in the future.

The calculated rms beam radii by solving Eq. (30) are shown to agree with the available experimental rms beam radius measurements.⁵ In Fig. 7, the calculated beam radii $R \equiv \sqrt{2}r_{\text{brms}}$ are plotted as solid curves by solving Eq. (30) for three 5 keV electron beams with currents (emittances), 43 mA ($4\epsilon_{\text{rms}} = 71$ mm-mrad), 6.5 mA ($4\epsilon_{\text{rms}} = 30$ mm-mrad), and 1.9 mA ($4\epsilon_{\text{rms}} = 20$ mm-mrad). The three beams are focused by a short solenoid magnet whose on-axis magnetic field is shown as a dashed curve. The calculated beam radii for the two beams with currents 43 and 1.9 mA agree with the previous experiment measurements (dotted curves) and calculations in Ref. 5, as expected. The calculated beam radius for the 6.5 mA beam will be used for the following density calculations.

By solving Eqs. (37) and (38), we calculate the beam transverse density profiles of the UMER 5 keV, 6.5 mA electron beam at three axial distances: $s = 6.4$, 11.2, and 17.2 cm, as shown by the solid curves in Fig. 8. The dashed curves are the equivalent KV beam density profiles.^{5,11} Compared with the experimental measurements (dotted curves),⁵ the calculated beam density profiles are in good agreement. As the beam radius increases, the beam density profile approaches the KV (uniform) beam density profile, because the beam temperature must decrease in order to keep $T_{\perp}(s)r_{\text{brms}}^2(s)$ at a constant. In this adiabatic process, the Debye length $\lambda_D \equiv \sqrt{\gamma_b k_B T_{\perp}(s) / 4\pi q^2 n_b(0, s)} = 0.54$ mm is constant.

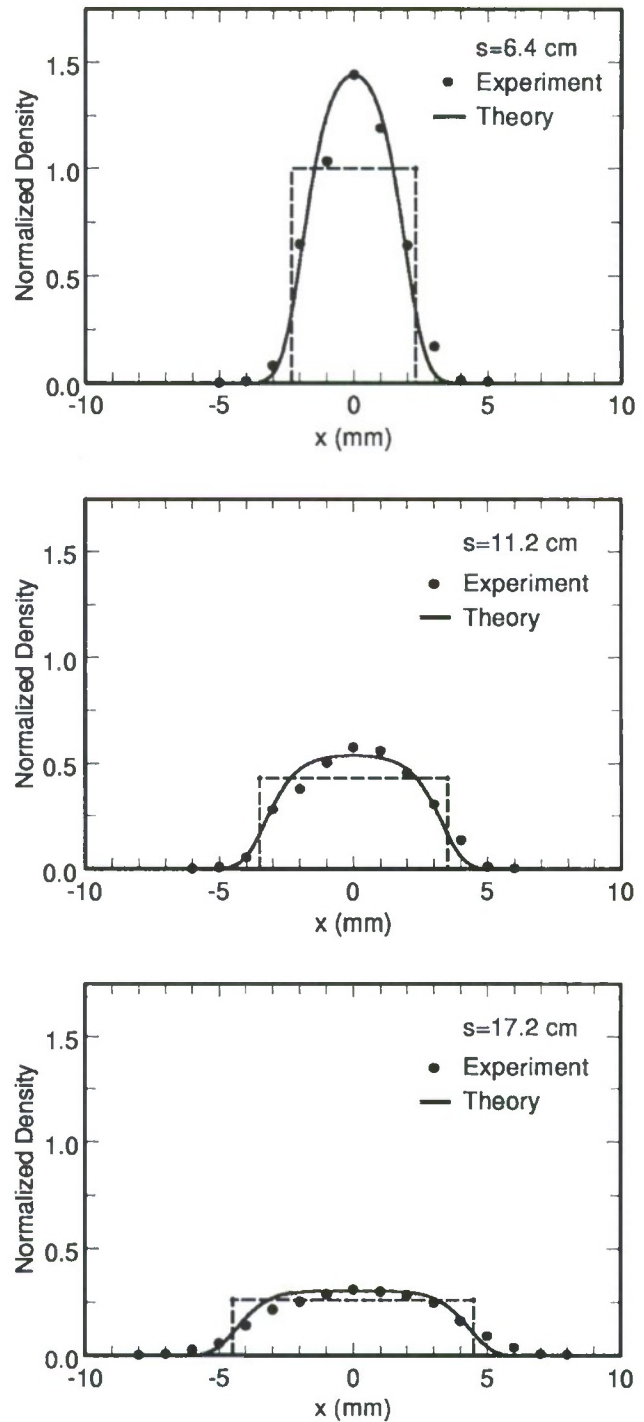


FIG. 8. Normalized transverse beam density profiles of a 5 keV, 6.5 mA ($4\epsilon_{\text{rms}} = 30$ mm-mrad) electron beam at three axial distances: $s = 6.4$, 11.2, and 17.2 cm. The solid curves are from theory, the dotted curves are the experimental measurements, and the dashed lines are the equivalent KV beam density distributions. The densities are normalized to the equivalent KV beam density at $s = 6.4$ cm.

VI. CONCLUSION

In conclusion, an adiabatic thermal equilibrium was discovered for an intense, axisymmetric charged-particle beam propagating through a periodic solenoidal focusing field. The

thermal beam distribution function was constructed. The beam rms envelope equation was derived, and the self-consistent nonuniform density profile was calculated. Other statistic properties such as flow velocity, temperature, total emittance and rms thermal emittance, equation of state, and Debye length were studied. Good agreement was found between the adiabatic thermal equilibrium theory and recent high-intensity beam experimental measurements at the University of Maryland Electron Ring.

ACKNOWLEDGMENTS

This research was supported by the U.S. Department of Energy, Office of High-Energy Physics, Grant No. DE-FG02-95ER40919, Office of Fusion Energy Sciences, Grant No. DE-FG02-05ER54836, and Air Force Office of Scientific Research, Grant No. FA9550-06-1-0269.

¹I. M. Kapchinskij and V. V. Vladimirkij, in *Proceedings of the International Conference on High Energy Accelerators* (CERN, Geneva, 1959), p. 274.

²F. J. Sacherer, "Transverse space-charge effects in circular accelerators," Ph.D. thesis, University of California, Berkeley (1968), pp. 15–19.

³R. C. Davidson, *Physics of Nonneutral Plasmas* (Addison-Wesley, Reading, MA, 1990).

⁴C. Chen, R. Pakter, and R. C. Davidson, *Phys. Rev. Lett.* **79**, 225 (1997).

⁵S. Bernal, B. Quinn, M. Reiser, and P. G. O'Shea, *Phys. Rev. ST Accel. Beams* **5**, 064202 (2002).

⁶R. Davidson, H. Qin, and P. J. Channell, *Phys. Rev. ST Accel. Beams* **2**, 074401 (1999).

⁷M. Reiser, *Theory and Design of Charged Particle Beams* (Wiley, New York, 1994), Chap. 5.

⁸K. Samokhvalova, J. Zhou, and C. Chen, *Phys. Plasmas* **14**, 103102 (2007).

⁹M. Reiser and N. Brown, *Phys. Rev. Lett.* **71**, 2911 (1993).

¹⁰R. C. Davidson, *Phys. Rev. Lett.* **81**, 991 (1998), and references therein.

¹¹F. J. Sacherer, *IEEE Trans. Nucl. Sci.* **18**, 1105 (1971).

¹²G. Schmidt, *Physics of High Temperature Plasmas*, 2nd ed. (Academic, New York, 1979), p. 70.

¹³J. Zhou, B. L. Qian, and C. Chen, *Phys. Plasmas* **10**, 4203 (2003).

¹⁴O. A. Anderson, *Part. Accel.* **21**, 197 (1987).

Small-signal gain theory of a nonrelativistic planar magnetron

Jing Zhou^{a)} and Chiping Chen

Plasma Science and Fusion Center, Massachusetts Institute of Technology, Cambridge, Massachusetts 02139, USA

(Received 16 April 2008; accepted 15 September 2008; published online 16 October 2008)

A small-signal theory of a nonrelativistic magnetron is developed using a planar model with a thin electron cloud. The theory includes both inertial effects and electromagnetic effects in a Floquet expansion. An analytical dispersion relation of such a planar magnetron is derived, and the growth rate is calculated analytically. The found instability involves the resonance between the electron cloud and the magnetron cavity vacuum slow waves. A good agreement is found between the theory and the self-consistent particle-in-cell MAGIC simulations. © 2008 American Institute of Physics. [DOI: 10.1063/1.2996577]

Crossed-field devices, such as magnetrons and crossed-field amplifiers (CFA), are of great interest because of their low cost, high efficiency, compactness, and robustness. They have many civilian, industrial, and military applications.¹⁻³ Such devices generate high power rf radiation via stimulated interactions, as high density electron clouds drift across the crossed electric and magnetic fields in periodic cavities. On the qualitative level, the generation and operation of such high density electron clouds are relatively straightforward following electrostatics and magnetostatics. The mechanisms of the rf wave generation, however, have yet to be fully described due to the complicated processes of the rf interaction.

The onset of the unstable oscillations in magnetrons has not been analytically described although extensive particle-in-cell (PIC) simulations can make good predictions for the instability characteristics.^{4,5} Previous studies included various models utilizing linear theories. Earlier work focused on the diocotron instability in the guiding-center approximation,^{6,7} which ignores inertial effects in the electron cloud. The recent work by Riyopoulos, using a guiding-center model, provided insight into the magnetron instability in the low-space-charge limit.⁸ A linear theory taking a single rf mode in the Floquet expansion was developed to include electromagnetic effects.⁹ Despite these theoretical and PIC simulation efforts, a quantitative agreement between theory and PIC simulations has not been reported until this letter.

In this letter, we develop a small-signal (linear) theory that includes both inertial and electromagnetic effects in a Floquet expansion. We consider a planar magnetron or CFA with the geometry as shown in Fig. 1. The A-K gap of the cylindrical magnetron is assumed to be small compared with the cathode radius. As shown in Fig. 1, the cathode is located at $x=0$ and the anode is a slow-wave structure consisting of a periodic array of vanes and slots. The applied magnetic field points out of the page, which forces the electron drift velocity in the y -direction. In a conventional magnetron or CFA, there is an electron sheath that extends out for some distance from the cathode. However, such a finite electron sheath introduces a problem of multiple poles (singularities) in the theoretical computation of the small-signal gain. To

avoid the singularity problem, we approximate the electron sheath as an infinite thin electron cloud stream, which is located at $x=h$. Because of the resonant interaction, our thin electron cloud stream model captures the basic gain mechanism in the realistic shear flow in a magnetron.

In the small-signal theory, we assume that the system starts from an equilibrium (dc) state and a small oscillation (rf) builds up as the electron cloud drifts in the A-K gap. The general form of any field variable ψ is

$$\psi = \psi_0(x, y) + \delta\psi(x, y, t), \quad (1)$$

where $\psi_0(x, y)$ denotes the equilibrium field variable. Because the magnetron is periodic in the y -direction with periodicity L , all of the perturbations in Eq. (1) must be of the Floquet form,

$$\delta\psi(x, y, t) = \sum_{q=-\infty}^{\infty} \delta\psi_{k_q}(x) e^{i(k_q y - \omega t)}, \quad (2)$$

where $k_q = k_z + 2\pi q/L$. The small-signal theory is valid for the initial growth stage of the magnetron interaction. Near or after saturation, a nonlinear theory is needed.¹⁰

The corrugation on the anode induces a small static periodic perturbation on the equilibrium profile of the electron sheath, as observed in our two-dimensional (2D) MAGIC simulations. In our simplified model, we approximate the thin electron sheath by a number of electron cloud streams with slightly different flow velocities and express the total equilibrium charge and current densities as $\rho(\mathbf{x}) =$

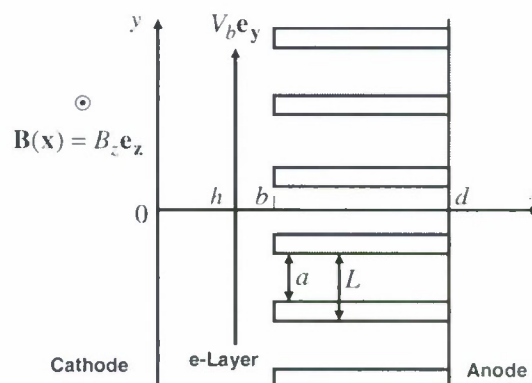


FIG. 1. Schematic of a planar magnetron with a thin electron cloud stream.

^{a)}Electronic mail: jia_zhou@psfc.mit.edu.

$-e\sum_{j=1}^M\sigma_{bj}\delta(x-h)$ and $\mathbf{J}(\mathbf{x})=-e\sum_{j=1}^M\sigma_{bj}V_{bj}\delta(x-h)\mathbf{e}_x$, respectively, where M is the number of electron cloud streams, $-e$ is the electron charge, $\sigma_b=\sum_{j=1}^M\sigma_{bj}$ is the total surface number density of the electron cloud, and $x=h$ specifies the transverse displacement of the electron sheath. The equilibrium flow velocity V_{bj} is determined by adding a small velocity ΔV_{bj} from the averaged flow velocity,

$$\bar{V}_b = \frac{1}{B_0} \left[\frac{V_D}{b} + \frac{e\sigma_b}{\epsilon_0} \left(-\frac{1}{2} + \frac{h}{b} \right) \right], \quad (3)$$

where V_D is the applied A-K gap voltage, B_0 is the applied magnetic field strength, ϵ_0 is the permittivity in vacuum, and b is the A-K gap width, as shown in Fig. 1. Typically, ΔV_{bj} is a few percentage of \bar{V}_b , whose value can be estimated from the 2D MAGIC simulations.

Using the linearized nonrelativistic cold-fluid equations and the linearized Maxwell equations, the eigenvalue equation for δE_{yk_q} is derived to be

$$\begin{aligned} \frac{\partial^2}{\partial x^2} \delta E_{yk_q} + \sum_{j,j'} H_{jj'}^{-1}(\omega, k_q) \frac{\omega_{pj}^2 \omega_c (\omega - k_q V_{bj'})}{(\omega - k_q V_{bj})^2} \\ \times \left(k_q - \frac{\omega V_b}{c^2} \right) \frac{\partial}{\partial x} \delta E_{yk_q} + \left(\frac{\omega^2}{c^2} - k_q^2 \right) \\ \times \left\{ 1 - \sum_{j,j'=1}^M [H_{jj'}^{-1}(\omega, k_q) \omega_c^2 + 1] \frac{\omega_{pj}^2}{(\omega - k_q V_{bj})^2} \right\} \delta E_{yk_q} \\ = 0, \end{aligned} \quad (4)$$

where $\omega_c = eB_0/m$ is the electron cyclotron frequency, $\omega_{pj}^2(x) = e^2 \sigma_{bj} \delta(x-h)/\epsilon_0 m$ is the effective plasma frequency squared of the j th electron cloud stream, and

$$H_{jj'}(\omega, k_q) = \begin{cases} (\omega - k_q V_{bj})^2 \left[1 - \frac{\omega_{pj}^2}{\omega^2 - c^2 k_q^2} \right] - \omega_c^2 \equiv v_{jk_q}^2, & j = j' \\ -\frac{(\omega - k_q V_{bj})^2}{\omega^2 - c^2 k_q^2} \omega_{pj'}^2, & j \neq j', \end{cases} \quad (5)$$

and $H_{jj'}^{-1}(\omega, k_q)$ is the element of the inverse matrix $\mathbf{H}^{-1}(\omega, k_q)$. Here, m is the electron mass and c is the speed of light in vacuum.

The boundary conditions for the electric field δE_{yk_q} are that the electric field vanishes at the cathode $x=0$, and the anode wall $x=d$ and is continuous in the y -direction at the electron cloud layer $x=h$; the admittance¹¹ is continuous at the vane tip $x=b$ and

$$\begin{aligned} \frac{\partial \delta E_{yk_q}}{\partial x} \Big|_{x=h+0} - \frac{\partial \delta E_{yk_q}}{\partial x} \Big|_{x=h-0} \\ = \sum_{j=1}^M \frac{e^2 \sigma_{bj}}{\epsilon_0 m} \frac{(\omega^2 - c^2 k_q^2)}{c^2 (\omega - k_q V_{bj})^2} \delta E_{yk_q}(x=h). \end{aligned} \quad (6)$$

Equation (6) can be derived by integrating Eq. (4) for $x=h-0$ to $x=h+0$ and making use of $\lim_{x \rightarrow h} H_{jj'}^{-1}(\omega, k_q) = \delta_{jj'}/v_{jk_q}^2$.

Solving Eq. (4) in the regions $0 \leq x \leq h$, $h \leq x \leq b$, and $b \leq x \leq d$ and matching the solutions at the boundaries, we arrive at the small-signal gain equation or the loaded dispersion relation

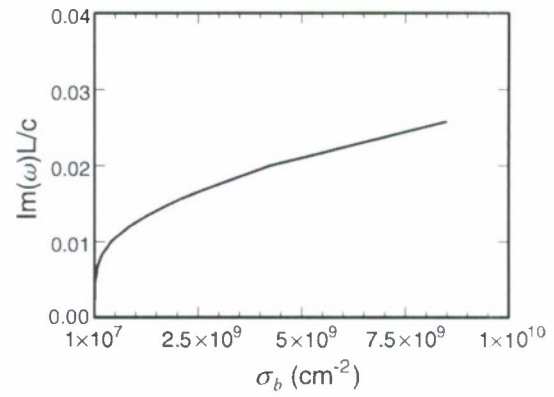


FIG. 2. Plot of the maximum temporal growth rate $\text{Im}(\omega)$ as a function of the surface density σ_b for a single thin electron cloud stream with the structure parameters of $L=0.478$ cm, $a=0.382$ cm, $b=0.478$ cm, and $d=4.25$ cm in a uniform applied magnetic field of $B_z=180$ G and a A-K gap voltage of $V_D=2.52$ kV.

$$\begin{aligned} 0 = D(\omega, k_z) \equiv \cot \left[\frac{\omega}{c} (d-b) \right] + \frac{\omega ab}{cL} \sum_{q=-\infty}^{\infty} \frac{1}{p_q b} \\ \times \left| \frac{\sin(k_q a/2)}{k_q a/2} \right|^2 \frac{\cos(p_q b) + \epsilon_{k_q}(\omega) \cos[p_q(b-h)]}{\sin(p_q b) + \epsilon_{k_q}(\omega) \sin[p_q(b-h)]}, \end{aligned} \quad (7)$$

where

$$\epsilon_{k_q}(\omega) = \sum_{j=1}^M \frac{p_q}{(\omega - k_q V_{bj})^2} \left(\frac{e^2 \sigma_{bj}}{\epsilon_0 m} \right) \sin(p_q h) \quad (8)$$

and $p_q = \sqrt{\omega^2/c^2 - k_q^2}$. Setting $\epsilon_{k_q}=0$, Eq. (7) is the vacuum dispersion relation for the corrugated structure. A numerical code, named crossed-field amplifier system simulator (CFASS), is developed to solve Eq. (7).

To show the dependence of the growth rate of an unstable mode on the electron density, we plot the maximum temporal growth rate as a function of the surface density σ_b in Fig. 2. The parameters of the structure are chosen to be $L=0.478$ cm, $a=0.382$ cm, $b=0.478$ cm, and $d=4.25$ cm in a uniform applied magnetic field of $B_z=180$ G and an A-K gap voltage of $V_D=2.52$ kV. The electron cloud is assumed to be an infinitely long sheet with the surface density σ_b , which propagates at the velocity given by Eq. (3), i.e., the $\mathbf{E} \times \mathbf{B}$ drift velocity, at the location of $h=0.382$ cm. As the surface density is varied, the phase shift of the unstable mode is tuned to achieve the maximum temporal growth rate. As shown in Fig. 2, the maximum growth rate increases as the surface density increases.

To compare our small-signal gain theory with 2D MAGIC simulations, we restrict our discussion to the low-current regime, where the thin-beam equilibrium model is a good approximation to the thin electron cloud in the 2D MAGIC simulations. At high currents, the electron cloud diffuses due to the strong image effects on the corrugated anode, and an improved model of electron cloud equilibrium is needed, which is beyond the scope of this letter.

As an example, we consider the same structure as in Fig. 2. The electron cloud is assumed to be an infinitely long sheet with $\sigma_b=2.12 \times 10^8$ cm⁻², which propagates at the averaged velocity $\bar{V}_b=0.098c$ at $h=0.382$ cm. The lowest un-

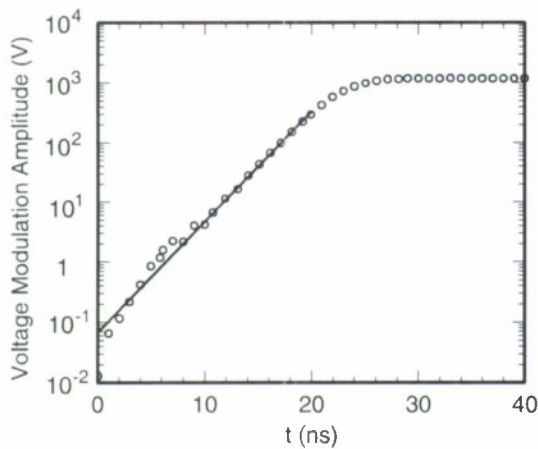


FIG. 3. Plot of the amplitude of oscillating voltage as a function of time as obtained from the MAGIC simulation. Here, the parameters are $L=0.478$ cm, $a=0.382$ cm, $b=0.478$ cm, $d=4.25$ cm, $h=0.382$ cm, $B_z=180$ G, $E_x=-5.27$ kV/cm, $\sigma_b=2.12 \times 10^8$ cm $^{-2}$, and $\bar{V}_b=0.098c$.

stable transverse mode (TM) is calculated to achieve the maximum growth rate at a phase of $2\pi/3$ and a frequency of 1.979 GHz.

The self-consistent PIC code, 2D MAGIC, is used to simulate the planar magnetron system. Because 2D MAGIC can handle only a few vanes, a three-vane slow-wave corrugated structure with the same parameters as in Fig. 2 is used in the simulation. Periodic boundary conditions are used such that the $2\pi/3$ mode is supported by the three-vane structure. The uniform crossed electric and magnetic fields are applied with $B_z=180$ G and $E_x=-5.27$ kV/cm. The electron beam is initialized as an infinitely long slab in the z direction with a width of 0.05 cm in the x direction. The electron beam propagates with an initial velocity of $\bar{V}_b=0.098c$.

As the beam propagates, the instability starts to build up, which is illustrated by the voltage crossing the vane tip of the slow-wave structure. In Fig. 3, the amplitude of the oscillating voltage filtered by a filter that selects the $2\pi/3$ mode is plotted. In the early stage of the instability (e.g., for $t < 15$ ns), the oscillation has a very small amplitude and exhibits a relatively broad frequency spectrum. Starting from $t=10$ ns, the $2\pi/3$ mode grows exponentially. It saturates at about $t=26$ ns. For this MAGIC simulation, the $2\pi/3$ mode is determined to have a frequency of 1.93 GHz and an amplitude growth rate of 3.12 dB/cm, shown as a circle and a cross in Fig. 4, respectively.

To compare the MAGIC simulation results with our theory, we solve the loaded dispersion relation in Eq. (7) to calculate the real frequency and the instability growth rate. Due to the influence of the anode corrugation, the electron cloud velocity prior to the linear growth is observed to vary sinusoidally in the y -direction with a small amplitude around the averaged flow velocity in the MAGIC simulation. To model the velocity variation, we use three electron cloud streams at the same location $x=0.0384$ cm, each with one-third of the total surface density $\sigma_{b1}=\sigma_{b2}=\sigma_{b3}=\sigma_b/3$ and slightly different velocities, i.e., $V_{b1}=0.98\bar{V}_b$, $V_{b2}=\bar{V}_b$, and

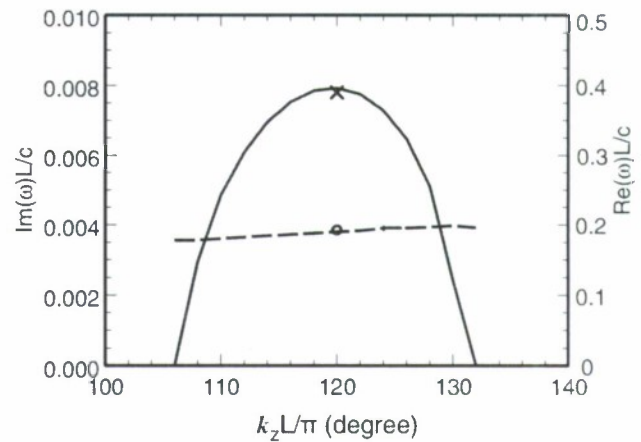


FIG. 4. Plot of the temporal growth rate $\text{Im}(\omega)$ (solid curve) and the real frequency $\text{Re}(\omega)$ (dashed curve) as a function of wave number k_z for the lowest resonant TM mode. The solid and dashed curves are obtained from Eq. (7) using the three electron cloud streams with surface densities $\sigma_{b1}=\sigma_{b2}=\sigma_{b3}=\sigma_b/3=7.07 \times 10^7$ cm $^{-2}$ and flow velocities $V_{b1}=0.98\bar{V}_b$, $V_{b2}=\bar{V}_b=0.098c$, and $V_{b3}=1.02\bar{V}_b$, respectively. The circle and cross are the real frequency and instability growth rate from the MAGIC simulation, respectively. Here, the other parameters are the same as those in Fig. 3.

$V_{b3}=1.02\bar{V}_b$. The theoretical growth rate is in good agreement with the MAGIC simulation, as shown in Fig. 4.

In conclusion, a small-signal theory of a nonrelativistic magnetron was developed using a planar model with a thin electron cloud. The theory includes inertial effects and electromagnetic effects in a Floquet expansion. The present planar model is valid provided that the A-K gap is small compared with the cathode radius. The thin electron cloud avoids the problem of multiple poles (singularities) in the dispersion relation. An analytical dispersion relation of such a planar magnetron was derived, and the growth rate was calculated analytically. 2D MAGIC simulations were performed to verify the theory. A good agreement was found between the theory and MAGIC simulations.

This research was supported by the Air Force Office of Scientific Research (Grant No. FA9550-06-1-0269).

- ¹J. Benford, J. A. Swegle, and E. Schamiloglu, *High Power Microwaves* (Taylor & Francis, New York, 2007).
- ²V. B. Neculaes, Y. Y. Lau, and R. M. Gilgenbach, *Appl. Phys. Lett.* **83**, 1938 (2003).
- ³M. R. Lopez, R. M. Gilgenbach, M. C. Jones, W. M. White, D. W. Jordan, M. D. Johnston, T. S. Strickler, Y. Y. Lau, T. A. Spencer, M. D. Haworth, K. L. Cartwright, P. J. Mardahl, J. W. Luginsland, and D. Price, *IEEE Trans. Plasma Sci.* **32**, 1171 (2004).
- ⁴H.-W. Chan, C. Chen, and R. C. Davidson, *J. Appl. Phys.* **73**, 7053 (1993).
- ⁵R. W. Lemke, T. C. Genoni, and T. A. Spencer, *Phys. Plasmas* **6**, 603 (1999).
- ⁶V. M. Ayres, H. C. Chen, R. A. Stark, H. S. Uhm, and H. E. Brandt, *Phys. Fluids B* **4**, 3396 (1992).
- ⁷R. C. Davidson, H. W. Chan, C. Chen, and S. Lund, *Rev. Mod. Phys.* **63**, 341 (1991).
- ⁸S. Riyopoulos, *Phys. Rev. Lett.* **81**, 3026 (1998).
- ⁹D. J. Kaup, *Phys. Plasmas* **8**, 2473 (2001).
- ¹⁰D. J. Kaup, *Phys. Plasmas* **11**, 3151 (2004).
- ¹¹R. E. Collin, *Foundations for Microwave Engineering* (McGraw-Hill, New York, 1966), p. 90.

Periodic focusing of a high-space-charge elliptic charged-particle beam

Jing Zhou, Ronak J. Bhatt* and Chiping Chen

Plasma Science and Fusion Center

Massachusetts Institute of Technology

Cambridge, Massachusetts 02139

Abstract

A self-consistent solution is developed for the focusing of coasting, sheet-like, space-charge-dominated elliptic beams using a hybrid of non-axisymmetric periodic permanent magnets (PPM) and quadrupole magnets. The beam envelope equations and equilibrium flow profiles are obtained using a paraxial cold-fluid model. Further, a kinetic theory is developed to determine the self-consistent beam distribution and its evolution and to study the temperature effects. Both cold-fluid and kinetic equilibrium theories are validated by two-dimensional (2D) particle-in-cell (PIC) simulations using the 2D Periodically Focused Beam (PFB2D) code, and by three-dimensional (3D) self-consistent trajectory simulations using OMNITRAK. The theories and PFB2D and OMNITRAK simulations are applied to design such high-space-charge elliptic beams for applications in klystrons and vacuum electron devices. Numerical results show that the beam edges in both transverse directions are well confined without twisting and the elliptic beam density profile is well preserved. For space-charge-dominated elliptic beams used in ribbon-beam

klystron applications, the temperature effects are studied using both the kinetic equilibrium theory and PFB2D simulations.

PACS: 29.27.Bd, 52.59.Sa, 47.75.+f, 52.25.Dg

*Present address: 18115 Tawnas Way Lane, Cypress, TX 77429.

I. Introduction

There are vigorous activities in the research and development of elliptic-beam sources, traveling wave amplifiers, klystrons, and accelerator focusing systems. Over 600 high-power, high-efficiency klystrons, for example, may be needed to provide rf power for the acceleration cavities of the proposed TeV International Linear Collider (ILC). The Stanford Linear Accelerator Center (SLAC) has proposed a 10 MW sheet-beam klystron to meet this need [1]. Other groups, such as Los Alamos National Laboratory (LANL) and Scientific Applications International Corporation (SAIC), are also interested in sheet-beam technology for microwave amplifier applications [2, 3]. The LANL team has employed a solenoid/quadrupole magnet combination to transform an incident circular beam into an emergent elliptic beam [4]. The Massachusetts Institute of Technology (MIT) has also initiated an elliptic beam project for communications and accelerator applications [5]. Beam Power Technology, Inc. is developing a ribbon-beam amplifier based on the elliptic beam technology developed at MIT.

Elliptic beams have attracted broad interests because they have the following remarkable properties. First, they can transport large amounts of beam currents at reduced intrinsic space-charge forces and energies. Second, they couple efficiently to rectangular or elliptic rf structures. The combination of the space-charge reduction and efficient coupling allows efficient rf generation in vacuum electronic devices, and efficient acceleration in particle accelerators. Third, elliptic beams provide an additional adjustable parameter (e.g., the aspect ratio) which may be useful for better matching a beam into a non-axisymmetric periodic focusing channel.

Transport and focusing of sheet (ribbon) beams has been discussed in the literature for four decades. Periodic transverse (wiggler) magnetic focusing [6, 7] has been used for free-electron laser applications, but it can lead to excessive centroid motion for space-charge-dominated beams [8]. Promising results have been obtained through recent studies of period-averaged focusing in the periodic cusp magnetic (PCM) field [8, 9] or the hybrid of PCM and the periodic quadrupole magnet (PQM) field [10, 11] for space-charge-dominated and emittance-dominated sheet beams, however, significant envelope oscillations and emittance growth are sometimes seen. They may be rectified by the present thorough treatment which does not employ period-averaging but self-consistently includes the effects of beam flow profiles and evolving self-fields neglected in the period-averaging approximation.

Recent efforts in this vein [5, 12] have led to a deeper understanding of high-space-charge elliptic beam propagation in a non-axisymmetric periodic permanent magnet (PPM) field. Pure non-axisymmetric PPM focusing, however, is unsuited for sheet-like elliptic beams with very large aspect-ratio because the twisting of the beam introduces instabilities, and because the magnetic field nonlinearities in the wide tails of the beam become appreciable.

In this paper, we develop a self-consistent solution for the focusing of coasting, sheet-like, space-charge-dominated elliptic beams using the most general formulation of centroid preserving linear fields – a hybrid of non-axisymmetric PPM and quadrupole magnets [13]. A paraxial cold-fluid model is employed to derive generalized envelope equations that determine the equilibrium flow properties of ellipse-shaped beams with negligibly small emittance. Furthermore, a kinetic analysis is developed to determine the

beam distribution consistent with the equilibrium flow properties of a uniform ellipse-shaped beam. In the kinetic model, the emittances are taken into account. A matched envelope solution is obtained numerically from the generalized envelope equations, and the results show that the beam edges in both transverse directions are well confined without twisting. Two dimensional (2D) particle-in-cell (PIC) simulations with our Periodic Focused Beam 2D (PFB2D) code and 3D Omnitrak simulations show good agreement with the predictions of equilibrium theory as well as beam stability. For space-charge-dominated elliptic beams used in ribbon-beam klystron applications, the temperature effects are studied using both the kinetic equilibrium theory and PFB2D simulations.

The organization of the present paper is as follows. In Sec. II, the cold-fluid equilibrium theory is used to derive the generalized envelope equations for a high-space-charge elliptic beam. In Sec. III, the kinetic equilibrium theory of a large-aspect-ratio ellipse-shaped charged-particle beam is presented following Sacherer's matrix method [14], and the generalized envelope equations which include the emittances are derived. In Sec. IV, PIC PFB2D simulations are used to verify the theoretical results and examples of large-aspect-ratio elliptic beams are discussed. Conclusions are presented in Sec. V.

II. Cold-fluid equilibrium theory

We consider a high-intensity, space-charge-dominated beam, in which kinetic (thermal emittance) effects are negligibly small. The beam can be adequately described by cold-fluid equations. In the paraxial approximation, the steady-state cold-fluid equations for time-stationary flow ($\partial/\partial t = 0$) in cgs units are [15, 16]

$$\beta_b c \frac{\partial}{\partial s} n_b + \nabla_{\perp} \cdot (n_b \mathbf{V}_{\perp}) = 0, \quad (1)$$

$$\nabla_{\perp}^2 \phi^s = \beta_b^{-1} \nabla_{\perp}^2 A_z^s = -4\pi q n_b, \quad (2)$$

$$n_b \left(\beta_b c \frac{\partial}{\partial s} + \mathbf{V}_{\perp} \cdot \nabla_{\perp} \right) \mathbf{V}_{\perp} = \frac{q n_b}{\gamma_b m} \left[-\frac{1}{\gamma_b^2} \nabla_{\perp} \phi^s + \beta_b \hat{\mathbf{e}}_z \times \mathbf{B}_{\perp}^{ext} + \frac{\mathbf{V}_{\perp}}{c} \times B_z^{ext}(s) \hat{\mathbf{e}}_z \right], \quad (3)$$

where $s = z$, $\mathbf{x}_{\perp} = x\hat{\mathbf{e}}_x + y\hat{\mathbf{e}}_y$, $\nabla_{\perp} = \partial/\partial \mathbf{x}_{\perp}$, q and m are the particle charge and rest mass, respectively, n_b is the particle density, \mathbf{V}_{\perp} is the transverse flow velocity, $\gamma_b = (1 - \beta_b^2)^{-1/2}$ is the relativistic mass factor, use has been made of $\beta_z = V_z/c \cong \beta_b = \text{const}$, c is the speed of light in vacuum, and the self-electric field \mathbf{E}^s and self-magnetic field \mathbf{B}^s are determined from the scalar potential ϕ^s and vector potential $A_z^s \hat{\mathbf{e}}_z$, i.e., $\mathbf{E}^s = -\nabla_{\perp} \phi^s$ and $\mathbf{B}^s = \nabla_{\perp} \times A_z^s \hat{\mathbf{e}}_z$.

We use the combination of a periodic non-axisymmetric magnetic field and a quadrupole magnetic field to focus a nearly straight large-aspect-ratio elliptic beam, whose twist angle is minimized. For the beam dimensions small relative to the characteristic scale of magnetic variations, i.e., $(k_{0x}x)^2/6 \ll 1$ and $(k_{0y}y)^2/6 \ll 1$, the combined magnetic field can be described to the lowest order in the transverse dimensions as

$$\mathbf{B}^{ext} = B_z(s)\mathbf{e}_z - \frac{dB_z(s)}{ds} \left[\frac{k_{0x}^2}{k_0^2} x\mathbf{e}_x + \frac{k_{0y}^2}{k_0^2} y\mathbf{e}_y \right] + B'_q(s)[y\mathbf{e}_x + x\mathbf{e}_y]. \quad (4)$$

where $k_0 = 2\pi/S$, $k_{0x}^2 + k_{0y}^2 = k_0^2$, S is the axial periodicity length, and

$$B'_q(s) \equiv \partial B_x^q / \partial y \Big|_{(s,0,0)} = \partial B_y^q / \partial x \Big|_{(s,0,0)}.$$

We seek solutions to Eqs. (1)-(3) of the form

$$n_b(\mathbf{x}_\perp, s) = \frac{N_b}{\pi a(s)b(s)} \Theta \left[1 - \frac{\tilde{x}^2}{a^2(s)} - \frac{\tilde{y}^2}{b^2(s)} \right], \quad (5)$$

$$\mathbf{V}_\perp(\mathbf{x}_\perp, s) = [\mu_x(s)\tilde{x} - \alpha_x(s)\tilde{y}] \beta_b c \hat{\mathbf{e}}_{\tilde{x}} + [\mu_y(s)\tilde{y} + \alpha_y(s)\tilde{x}] \beta_b c \hat{\mathbf{e}}_{\tilde{y}}. \quad (6)$$

In Eqs. (5) and (6), $\mathbf{x}_\perp = \tilde{x}\hat{\mathbf{e}}_{\tilde{x}} + \tilde{y}\hat{\mathbf{e}}_{\tilde{y}}$ is a transverse displacement in the twisted coordinate system illustrated in Fig. 1; $\theta(s)$ is the twist angle of the ellipse; $\Theta(x) = 1$ if $x > 0$ and $\Theta(x) = 0$ if $x < 0$; and the functions $a(s)$, $b(s)$, $\mu_x(s)$, $\mu_y(s)$, $\alpha_x(s)$, $\alpha_y(s)$ and $\theta(s)$ are to be determined self-consistently [see Eqs. (8)-(12)]. We carry the twist angle $\theta(s)$ in our calculation for the purpose of generalization, and we will take $\theta(s) = 0$ later to obtain the solution for a nearly straight elliptic beam.

The self-electric and self-magnetic fields are well known for an elliptical beam with density distribution specified in Eq. (5) [17], i.e.,

$$\phi^s = \beta_b^{-1} A_z^s = -\frac{2qN_b}{a+b} \left(\frac{\tilde{x}^2}{a} + \frac{\tilde{y}^2}{b} \right). \quad (7)$$

Using the expressions in Eqs. (4)-(7), it can be shown that both the equilibrium continuity equation (1) and force equation (3) are satisfied if the dynamical variables $a(s)$, $b(s)$, $\mu_x(s) \equiv a^{-1} da/ds$, $\mu_y(s) \equiv b^{-1} db/ds$, $\alpha_x(s)$, $\alpha_y(s)$ and $\theta(s)$ obey the generalized beam envelope equations (see Appendix A for the derivation)

$$\begin{aligned} \frac{d^2 a}{ds^2} - \frac{b^2(\alpha_x^2 - 2\alpha_x\alpha_y) + a^2\alpha_y^2}{a^2 - b^2} a - \frac{2K}{(a+b)} - 2\sqrt{\kappa_z(s)}\alpha_y a \\ + \left[\frac{k_{0x}^2 - k_{0y}^2}{k_0^2} \frac{d\sqrt{\kappa_z(s)}}{ds} \sin(2\theta) + \kappa_q(s)\cos(2\theta) \right] a = 0, \end{aligned} \quad (8)$$

$$\begin{aligned} \frac{d^2 b}{ds^2} + \frac{a^2(\alpha_y^2 - 2\alpha_x\alpha_y) + b^2\alpha_x^2}{a^2 - b^2} b - \frac{2K}{(a+b)} - 2\sqrt{\kappa_z(s)}\alpha_x b \\ - \left[\frac{k_{0x}^2 - k_{0y}^2}{k_0^2} \frac{d\sqrt{\kappa_z(s)}}{ds} \sin(2\theta) + \kappa_q(s)\cos(2\theta) \right] b = 0, \end{aligned} \quad (9)$$

$$\begin{aligned} \frac{d}{ds}(a^2\alpha_y) - \frac{ab^3(\alpha_x - \alpha_y)}{a^2 - b^2} \frac{d}{ds}\left(\frac{a}{b}\right) + 2a'a\sqrt{\kappa_z(s)} \\ + a^2 \left[2 \frac{k_{0x}^2 \cos^2 \theta + k_{0y}^2 \sin^2 \theta}{k_0^2} \frac{d\sqrt{\kappa_z(s)}}{ds} - \kappa_q(s)\sin(2\theta) \right] = 0, \end{aligned} \quad (10)$$

$$\begin{aligned} \frac{d}{ds}(b^2\alpha_x) - \frac{a^3b(\alpha_x - \alpha_y)}{a^2 - b^2} \frac{d}{ds}\left(\frac{b}{a}\right) + 2b'b\sqrt{\kappa_z(s)} \\ + b^2 \left[2 \frac{k_{0x}^2 \sin^2 \theta + k_{0y}^2 \cos^2 \theta}{k_0^2} \frac{d\sqrt{\kappa_z(s)}}{ds} + \kappa_q(s)\sin(2\theta) \right] = 0, \end{aligned} \quad (11)$$

$$\frac{d\theta}{ds} = \frac{a^2\alpha_y - b^2\alpha_x}{a^2 - b^2}, \quad (12)$$

where

$$\sqrt{\kappa_z(s)} \equiv \frac{qB_z(s)}{2\gamma_b\beta_b mc^2}, \quad \kappa_q(s) \equiv \frac{qB'_q(s)}{\gamma_b\beta_b mc^2} \quad \text{and} \quad K \equiv \frac{2q^2 N_b}{\gamma_b^3 \beta_b^2 mc^2}. \quad (13)$$

Equations (8)-(12) have “time” reversal symmetry under the transformation $(s, a, b, a', b', \alpha_x, \alpha_y, \theta) \rightarrow (-s, a, b, -a', -b', -\alpha_x, -\alpha_y, \theta)$. This implies that the dynamical system described by Eqs. (8)-(12) has the hyper symmetry plane $(a', b', \alpha_x, \alpha_y)$.

We look for a solution that has negligible twisting, i.e., $\theta(s) = 0$. In such a case, equation (12) leads to

$$\frac{\alpha_x(s)}{\alpha_y(s)} = \frac{a^2(s)}{b^2(s)}. \quad (14)$$

Correspondingly, the generalized envelope equations (8)-(11) become

$$\frac{d^2 a(s)}{ds^2} + \kappa_q(s)a(s) - 2\sqrt{\kappa_z(s)}\alpha_y(s)a(s) - \alpha_x(s)\alpha_y(s)a(s) - \frac{2K}{a(s)+b(s)} = 0, \quad (15)$$

$$\frac{d^2 b(s)}{ds^2} - \kappa_q(s)b(s) - 2\sqrt{\kappa_z(s)}\alpha_x(s)b(s) - \alpha_x(s)\alpha_y(s)b(s) - \frac{2K}{a(s)+b(s)} = 0, \quad (16)$$

$$\frac{d\alpha_x(s)}{ds} + \left[\frac{a'(s)}{a(s)} + \frac{b'(s)}{b(s)} \right] \alpha_x(s) + 2\sqrt{\kappa_z(s)} \frac{b'(s)}{b(s)} + 2 \frac{k_{0y}^2}{k_0^2} \frac{d\sqrt{\kappa_z(s)}}{ds} = 0, \quad (17)$$

$$\frac{d\alpha_y(s)}{ds} + \left[\frac{a'(s)}{a(s)} + \frac{b'(s)}{b(s)} \right] \alpha_y(s) + 2\sqrt{\kappa_z(s)} \frac{a'(s)}{a(s)} + 2 \frac{k_{0x}^2}{k_0^2} \frac{d\sqrt{\kappa_z(s)}}{ds} = 0. \quad (18)$$

The cold-fluid equilibrium provides a set of envelope equations, i.e., Eqs. (15)-(18) which determines the semi-axes of the elliptic beam and the flow velocity profile. The set of envelope equations is convenient to use for design of an elliptic focusing system. Normally, for given periodic lattice parameters, we solve Eq. (15)-(18) to obtain the matched solution of beam envelopes using periodic boundary conditions, which is a forward problem. On the other hand, for given beam envelope dimensions, we can solve Eq. (15)-(18) to determine the required lattice parameters, which is an inverse problem. As will be discussed in Sec. IV, we use the set of envelope equations to design two periodic lattice systems for two examples of elliptic beams given the beam parameters in Table 1. However, the cold-fluid theory does not provide detailed information of the

beam distribution and it does not take the emittance and temperature effects into account, which might be important in practical devices. The kinetic treatment required to address the emittance and temperature effects is discussed in Sec. III.

III. Kinetic Equilibrium Theory

In this section, we develop the kinetic equilibrium of the periodic focused large-aspect-ratio elliptic beams when the emittance is no longer small and the cold-fluid theory presented in Sec. II is no longer valid. Following Sacherer's theory [14, 18] that there exists a self-consistent uniformly charged beam in situations where both external forces and self forces acting on the charged particles are linear, we can construct the beam distribution and find the self-consistent envelope equations for the applied magnetic field configuration in Eq. (4). For simplicity, we consider the twist angle $\theta = 0$ in the following calculations. The results recover the cold-fluid theory in the cold-fluid limit.

We express the transverse single-particle equations of motion in the paraxial approximation,

$$\mathbf{p} = m\gamma \frac{d\mathbf{x}_\perp}{dt} \cong m\gamma_b \beta_b c \frac{d\mathbf{x}_\perp}{ds}, \quad (19)$$

and

$$\frac{d\mathbf{p}}{dt} \approx \beta_b c \frac{d\mathbf{p}}{ds} = q \left(\mathbf{E} + \frac{\mathbf{v}}{c} \times \mathbf{B} \right). \quad (20)$$

where \mathbf{p} is the relativistic particle momentum. Here, $\mathbf{E} = -\nabla\phi^s$ with ϕ^s given in Eq. (7)

and $\mathbf{B} = \mathbf{B}^s + \mathbf{B}^{ext}$ with $\mathbf{B}^s = \nabla_\perp \times A_z^s \hat{\mathbf{e}}_z$ and \mathbf{B}^{ext} given in Eq. (4).

Since all the terms in Eqs. (19) and (20) are linear, we reorganize the equations of motion (19) and (20) into a matrix format,

$$\frac{d\chi}{ds} = \mathbf{F} \cdot \chi, \quad (21)$$

where

$$\chi = \begin{pmatrix} x \\ x' \\ y \\ y' \end{pmatrix} \quad (22)$$

and

$$\mathbf{F} = \begin{pmatrix} 0 & F_{xp_x} & 0 & 0 \\ F_{p_x x} & 0 & F_{p_x y} & F_{p_x p_y} \\ 0 & 0 & 0 & F_{yp_y} \\ F_{p_y x} & F_{p_y p_x} & F_{p_y y} & 0 \end{pmatrix}. \quad (23)$$

The prime denotes the derivative with respect to s . For $\theta = 0$, the elements of \mathbf{F} are

$$F_{xp_x} = F_{yp_y} = 1, \quad (24)$$

$$F_{p_x x} = \frac{2K}{a(s)[a(s)+b(s)]} - \kappa_q(s), \quad (25)$$

$$F_{p_x y} = 2 \frac{k_{0y}^2}{k_0^2} \frac{d\sqrt{\kappa_z(s)}}{ds}, \quad (26)$$

$$F_{p_x p_y} = 2\sqrt{\kappa_z(s)}, \quad (27)$$

$$F_{p_y x} = -2 \frac{k_{0x}^2}{k_0^2} \frac{d\sqrt{\kappa_z(s)}}{ds}, \quad (28)$$

$$F_{p_y p_x} = -2\sqrt{\kappa_z(s)}, \quad (29)$$

$$F_{p_y y} = \frac{2K}{b(s)[a(s)+b(s)]} + \kappa_q(s). \quad (30)$$

For a single charged particle, there exists a transfer matrix $\mathbf{T}(s, s_0)$ that transforms an initial location $\chi_0(s_0)$ into a corresponding location at a later time $\chi(s)$, i.e.,

$$\chi(s) = \mathbf{T}(s, s_0) \cdot \chi_0(s_0) \quad (31)$$

and note that the elements of $\mathbf{T}(s, s_0)$ satisfy

$$\frac{d\mathbf{T}(s, s_0)}{ds} = \mathbf{F}(s) \cdot \mathbf{T}(s, s_0). \quad (32)$$

Since we know the equations of motion for individual charged particles, we can determine the evolution of any distribution of charged particles in phase space following Sacherer's theory. In particular, the distribution that is consistent with the linear self and focusing forces is a hyperellipsoid in the four dimensional phase space that gives a uniform density profile in the transverse plane (x, y) . The hyperellipsoid can be described by a symmetric matrix \mathbf{M} through the equation

$$f_b(x, x', y, y', s) = f_b(\chi^T(s) \cdot \mathbf{M}^{-1}(s) \cdot \chi(s)) \equiv \delta(\chi^T(s) \cdot \mathbf{M}^{-1}(s) \cdot \chi(s) - 1), \quad (33)$$

where the superscript “ T ” denotes the transpose operation of a matrix and $\delta(x)$ is the Direc-Delta function. At any position s , the distribution has the elliptical boundary $\chi^T(s) \cdot \mathbf{M}^{-1}(s) \cdot \chi(s) = 1$. Making use of Eqs. (31) and (33), we have

$$\mathbf{M}(s) = \mathbf{T}(s, s_0) \cdot \mathbf{M}(s_0) \cdot \mathbf{T}^T(s, s_0). \quad (34)$$

The evolution of the beam distribution is fully characterized by the distribution matrix $\mathbf{M}(s)$, which evolves according to

$$\frac{d\mathbf{M}(s)}{ds} = \mathbf{F}(s) \cdot \mathbf{M}(s) + \mathbf{M}(s) \cdot \mathbf{F}^T(s), \quad (35)$$

where we have used Eqs. (32) and (34).

We relate the ten independent elements of the matrix $\mathbf{M}(s)$ to the physical parameters in Appendix B, yielding

$$M_{11}(s) = a^2(s), \quad (36.a)$$

$$M_{22}(s) = \frac{16\varepsilon_{xrms}^2(s)}{a^2(s)} + a^2(s)\mu_x^2(s), \quad (36.b)$$

$$M_{33}(s) = b^2(s), \quad (36.e)$$

$$M_{44}(s) = \frac{16\varepsilon_{yrms}^2(s)}{b^2(s)} + b^2(s)\mu_y^2(s), \quad (36.d)$$

$$M_{12}(s) = a^2(s)\mu_x(s), \quad (36.e)$$

$$M_{13}(s) = 0, \quad (36.f)$$

$$M_{14}(s) = a^2(s)\alpha_y(s), \quad (36.g)$$

$$M_{23}(s) = -b^2(s)\alpha_x(s), \quad (36.h)$$

$$M_{24}(s) = a^2(s)\mu_x(s)\alpha_y(s) - b^2(s)\mu_y(s)\alpha_x(s), \quad (36.i)$$

$$M_{34}(s) = b^2(s)\mu_y(s), \quad (36.j)$$

where $a(s)$ and $b(s)$ are the semi axes of the ellipse which bounds the beam distribution in the configuration space, $\varepsilon_{xrms}(s)$ and $\varepsilon_{yrms}(s)$ are the rms emittances in the x – and y – directions, respectively. Furthermore, $\mu_x(s)$, $\mu_y(s)$, $\alpha_x(s)$, and $\alpha_y(s)$ are the flow velocities as defined in Eq. (6) with $\theta = 0$.

We use the evolution equation of the matrix $\mathbf{M}(s)$, i.e, Eq. (35), to determine the evolution equations for $a(s)$, $b(s)$, $\mu_x(s)$, $\mu_y(s)$, $\alpha_x(s)$, $\alpha_y(s)$, $\varepsilon_{xrms}(s)$ and $\varepsilon_{yrms}(s)$. Substituting Eq. (36) into Eq. (35), the first and third diagonal elements give the equations for the flow velocities,

$$\mu_x(s) = \frac{1}{a(s)} \frac{da(s)}{ds}, \quad (37)$$

$$\mu_y(s) = \frac{1}{b(s)} \frac{db(s)}{ds}. \quad (38)$$

The third element on the first row of Eq. (35) gives a relation for the rotational flow velocity, i.e.,

$$\frac{\alpha_x(s)}{\alpha_y(s)} = \frac{a^2(s)}{b^2(s)}. \quad (39)$$

We use the second element on the first row and the fourth element on the third row of Eq. (35) to determine the envelope equations for the beam semi-axes, yielding

$$\frac{d^2 a(s)}{ds^2} + \kappa_q(s)a(s) - 2\sqrt{\kappa_z(s)}\alpha_y(s)a(s) - \frac{2K}{a(s)+b(s)} = \frac{16\varepsilon_{xrms}^2}{a^3(s)}, \quad (40)$$

$$\frac{d^2 b(s)}{ds^2} - \kappa_q(s)b(s) - 2\sqrt{\kappa_z(s)}\alpha_x(s)b(s) - \frac{2K}{a(s)+b(s)} = \frac{16\varepsilon_{yrms}^2}{b^3(s)}, \quad (41)$$

where use has been made of Eqs. (37) and (38). Further, the second element of the third row and the fourth element on the first row of Eq. (35) determine the evolution of the rotational flow velocities $\alpha_x(s)$ and $\alpha_y(s)$

$$\frac{d\alpha_x(s)}{ds} + \left[\frac{a'(s)}{a(s)} + \frac{b'(s)}{b(s)} \right] \alpha_x(s) + 2\sqrt{\kappa_z(s)} \frac{b'(s)}{b(s)} + 2 \frac{k_{0y}^2}{k_0^2} \frac{d\sqrt{\kappa_z(s)}}{ds} = 0, \quad (42)$$

$$\frac{d\alpha_y(s)}{ds} + \left[\frac{a'(s)}{a(s)} + \frac{b'(s)}{b(s)} \right] \alpha_y(s) + 2\sqrt{\kappa_z(s)} \frac{a'(s)}{a(s)} + 2 \frac{k_{0x}^2}{k_0^2} \frac{d\sqrt{\kappa_z(s)}}{ds} = 0. \quad (43)$$

Finally, we use the second and fourth diagonal elements of Eq. (35) to determine the evolution of the rms emittances. After considerable simplification with aid of Eqs. (39)-(43), we find that the evolution equations of the rms emittances are two total differential equations which is expressed as, after integration,

$$\varepsilon_{xrms}^2(s) = \frac{1}{16} a^4(s) \alpha_x(s) \alpha_y(s) + c_1, \quad (44)$$

$$\varepsilon_{yrms}^2(s) = \frac{1}{16} b^4(s) \alpha_x(s) \alpha_y(s) + c_2, \quad (45)$$

where c_1 and c_2 are integration constants. The constants c_1 and c_2 are related to the rms thermal emittances which are defined as

$$\varepsilon_{th,x}^2 \equiv \langle x^2 \rangle \langle (x' - V_x / \beta_b c)^2 \rangle = \frac{a^2(s)}{16} \left[\frac{16 \varepsilon_{xrms}^2(s)}{a^2(s)} - b^2(s) \alpha_x^2(s) \right] = c_1, \quad (46)$$

$$\varepsilon_{th,y}^2 \equiv \langle y^2 \rangle \langle (y' - V_y / \beta_b c)^2 \rangle = \frac{b^2(s)}{16} \left[\frac{16 \varepsilon_{yrms}^2(s)}{b^2(s)} - a^2(s) \alpha_y^2(s) \right] = c_2, \quad (47)$$

where $V_x = \beta_b c [\mu_x(s)x - \alpha_x(s)y]$ and $V_y = \beta_b c [\mu_y(s)y + \alpha_y(s)x]$ are the flow velocities in the x - and y - directions, respectively, and the average denotes $\langle \chi \rangle = \int \chi f_b dx dy dx' dy'$. It should be stressed that the thermal emittances are kept constant, although the rms emittances are not constant and evolve as the beam propagates. In the cold-fluid limit, $\varepsilon_{th,x} = \varepsilon_{th,y} = 0$, $\varepsilon_{xrms}^2 = a^4(s) \alpha_x(s) \alpha_y(s) / 16$, $\varepsilon_{yrms}^2 = b^4(s) \alpha_x(s) \alpha_y(s) / 16$, and Eqs. (40)-(43) recover the cold-fluid results in Eqs. (15)-(18) for $\theta = 0$.

IV. Examples of intense elliptic beam equilibria

In this section, we present two examples of periodically focused large-aspect-ratio elliptic beam equilibria in a hybrid magnetic field configuration consisting of a periodic non-axisymmetric magnetic focusing field and a quadrupole magnetic field. One example is a high-space-charge elliptic beam for a high-efficiency 200 W ribbon-beam amplifier (RBA) under development at Massachusetts Institute of Technology (MIT) and Beam Power Technology for wireless communication. The other is a relativistic elliptic beam which can be used in a 10 MW L-Band ribbon-beam klystron (RBK) for the International Linear Collider (ILC).

To aid the design of high-space-charge elliptic beam transport, a numerical module in the PFB2D code [5, 12] has been developed to solve the generalized envelope equations (40)-(43), which determines the required magnetic field for the desired major-axis $a(s)$ and minor-axis $b(s)$ of the beam ellipse. Those information are used in 2D self-consistent PIC PFB2D simulations and 3D OMNITRAK self-consistent particle trajectory simulations to verify the theory.

As the first example, we consider a space-charge-dominated 6:1 elliptic electron beam with desired beam semi-axes $a = 0.373$ cm and $b = 0.062$ cm propagating with current $I_b = 0.11$ A along a beam tunnel with a constant axial potential of $V_b = 2290$ V. For this beam, we have $\beta_b = 0.094$ and $\gamma_b = 1.0045$. Based on the discussion in Ref. [19], we can take the intrinsic thermal emittance to be zero in this case, i.e., $\varepsilon_{th,x} = \varepsilon_{th,y} = 0$. We use the PFB2D code to solve the set of the generalized envelope equations (15)-(18) [or Eqs. (40)-(43)] to determine the required magnetic fields for focusing such a beam. The parameters of the hybrid periodic permanent magnet focusing fields are found to be

$B_z(s) = -263 \sin(k_0 s)$ G , $B'_q = 30.0$ G/cm , $S = 1.912$ cm , $k_{0y}/k_{0x} = 6$ (see Table 1, Column 2). As seen in Fig. 2, the matched beam semi-axes $a(s)$ and $b(s)$ (solid curves) solve the generalized envelope equations (15)-(18). The semi-major axis is almost a constant, whereas the semi-minor axis oscillates slightly about a constant value.

Shown in Fig. 2, the dotted curves are the envelopes of the beam ellipse obtained from the PFB2D self-consistent PIC simulation for the example of a nonrelativistic elliptic beam with voltage $V_b = 2290$ eV , current $I_b = 0.11$ A, aspect ratio $a/b = 6$ and $\varepsilon_{th,x} = \varepsilon_{th,y} = 0$ in the hybrid magnetic field with $B_z(s) = -263 \sin(k_0 s)$ G , $B'_q = 30.0$ G/cm , $S = 1.912$ cm , and $k_{0y}/k_{0x} = 6$. In the simulation, 5×10^5 particles are used. The thermal emittance is negligibly small, and the cold-fluid approximation is valid. As shown in Fig. 2, there is excellent agreement between the theoretical envelope solution (solid curves) and the self-consistent PIC simulation results (dotted curves). We measured the angle of the beam ellipse with respect to the laboratory frame. The angle oscillations have a small amplitude of 0.1 degrees, which are due to fluctuations (noise) in the simulation.

The PFB2D simulation also shows that the transverse beam distribution preserves the equilibrium profile as it propagates. In Fig. 3, 5,000 particles (a sample of the 5×10^5 particles in the PFB2D simulation) are plotted in the (x, y) plane and $(x, dy/ds)$ plane for five snapshots within one period: $s/S = 9.0, 9.25, 9.5, 9.75$ and 10.0 for the same elliptic beam shown in Fig. 2. The results in Fig. 3 also suggest that the beam equilibrium is stable.

As a separate verification of the theories and PFB2D code, a 3D OMNITRAK [13, 19] simulation is performed for the 6:1 nonrelativistic elliptic beam. Since 3D trajectory simulations are time-consuming, only a 2-period interval is used for this test, as shown in Fig. 4. The beam is sent through a conducting cylindrical beam tunnel (not shown) of radius 10.0 mm. In this simulation, 10,000 macroparticle arrays are used. However, only a fraction of them (i.e., 64 macroparticle arrays) are shown in Fig. 4(a). Substantially parallel, non-twisting transport is achieved, and the simulated beam envelopes agree with the theoretical predictions as shown in Fig. 4(b).

As the second example, we consider a relativistic elliptic beam that can be used in a 10 MW L-Band ribbon-beam klystron (RBK) for the International Linear Collider (ILC). The beam has a current of $I_b = 111.1$ A, a voltage of $V_b = 120$ kV and an aspect ratio of 20:1, which corresponds to $\beta_b = 0.094$ and $\gamma_b = 1.0045$. The other beam parameters are listed in the third column of Table 1. Solving the generalized envelope equations (40)-(43) with $\varepsilon_{th,x} = \varepsilon_{th,y} = 0$, the hybrid magnetic fields are determined to be the form of Eq. (4) with $B_z(s) = -2000 \sin(k_0 s)$ G, $B'_q = 80.8$ G/cm, $S = 2.2$ cm, and $k_{0,y}/k_{0,x} = 20$. In Fig. 5, the solid curves are the beam semi-axes $a(s)$ and $b(s)$ calculated from the generalized envelope equations (40)-(43) with $\varepsilon_{th,x} = \varepsilon_{th,y} = 0$, whereas dotted curves are from the self-consistent PIC PFB2D simulation.

For practical devices, elliptic beams usually have nonzero temperature due to the heating of sources or other effects. To study the temperature effects, we solve the generalized envelope equations (40)-(43) with nonzero initial thermal emittances, i.e., $\varepsilon_{th,x}^2 = k_B T a^2(s=0) / m \gamma_b \beta_b^2 c^2$ and $\varepsilon_{th,y}^2 = k_B T b^2(s=0) / m \gamma_b \beta_b^2 c^2$. As shown in Fig. 6,

the elliptic beam envelopes are calculated for three different temperature choices: 0 eV, 50 eV and 100 eV. Compared with the cold beam envelopes shown as solid curves in Fig. 6, the warm beam envelopes are found to increase slightly as the beam temperature increases, while the aspect ratio of the beam decreases from 20:1 to 16.4:1 as the beam temperature increases from 0 eV to 100 eV.

For the second example of elliptic beams, we assume that the elliptic beam is generated from an electron gun with an intrinsic temperature of 0.1 eV and a current density of 1.5 A/cm^2 [19]. The elliptic beam has to be compressed by a factor of 471.5 in area to achieve a current density of 707.3 A/cm^2 in the focusing channel. During the compression, the temperature increases by a factor of 471.5 to 47.2 eV. Therefore, in our calculations, a temperature of 50 eV is a reasonable assumption. As shown in Fig. 7, the envelopes of the elliptic beam with a temperature of 50 eV are obtained by solving the envelope equations (40)-(43) (solid curves) and by the PFB2D PIC simulations (dotted curves). Both results showed a slight increase in the two envelope dimensions and the aspect ratio of the elliptic beam decreases to 17.8, compared with the cold elliptic beam.

V. Conclusions

A self-consistent solution for the focusing of coasting, sheet-like, space-charge-dominated elliptic beams using a hybrid of non-axisymmetric periodic permanent magnets (PPM) and quadrupole magnets was developed. The beam envelope equation and equilibrium flow profiles were obtained using a paraxial cold-fluid model. Further, a kinetic theory was developed to determine the self-consistent beam distribution and its evolution. Both the cold-fluid and kinetic equilibrium theories were validated by the two-dimensional (2D) particle-in-cell (PIC) simulations using the 2D Periodically Focused Beam (PFB2D) code, and the three-dimensional (3D) self-consistent trajectory simulations using OMNITRAK. The theories and PFB2D and OMNITRAK simulations were applied to design such high-space-charge elliptic beams for applications in klystrons and vacuum electron devices. Numerical results showed that the beam edges in both transverse directions are well confined without twisting and the beam density profile is well preserved. For space-charge-dominated elliptic beams used in ribbon-beam klystron applications, the temperature effects are studied using both the kinetic equilibrium theory and PFB2D simulations.

Acknowledgement

The authors would like to thank Thomas M. Bemis for his assistance on OMNITRAK simulations. This work was supported by U. S. Department of Energy, Office of High-Energy Physics, Grant No. DE-FG02-95ER40919, and Air Force Office of Scientific Research, Grant No. FA9550-06-0269.

Reference

- [1] C. Adolphsen, Proc. 2007 Part. Accel. Conf. (2007), p. 3813.
- [2] S. J. Russell, Z. F. Wang, W. B. Haynes, R. M. Wheat Jr., B. E. Carlsten, L. M. Earley, S. Humphries Jr., and P. Ferguson, Phys. Rev. ST Accel. Beams **8**, 080401 (2005).
- [3] H. P. Freund and T. M. Abu-Elfadl, IEEE Trans. Plasma Sci. **32**, 1015 (2004).
- [4] B. E. Carlsten, S. J. Russell, L. M. Earley, F. L. Krawczyk, J. M. Potter, P. Ferguson, and S. Humphries Jr., IEEE Trans. Plasma Sci. **33**, 85 (2005).
- [5] J. Zhou, R. Bhatt, and C. Chen, Phys. Rev. ST Accel. Beams **9**, 34401 (2006).
- [6] P. A. Sturrock, J. Electron Control **7**, 162 (1959).
- [7] Z. X. Zhang, V. L. Granatstein, W. W. Destler, S. W. Bidwell, J. Rodgers, S. Cheng, T. M. Antonsen Jr., B. Levush, and D. J. Radack, IEEE Trans. Plasma Sci. **21**, 760 (1993).
- [8] J. H. Booske, B. D. McVey, and T. M. Antonsen Jr., J. Appl. Phys. **73**, 4140 (1993).
- [9] J. H. Booske, A. H. Kumbasar, and M. A. Basten, Phys. Rev. Lett. **71**, 3979 (1993).
- [10] J. H. Booske and M. A. Basten, IEEE Trans. Plasma Sci. **27**, 134 (1999).

- [11] M. A. Basten and J. H. Booske, J. Appl. Phys. **85**, 6313 (1999).
- [12] J. Zhou and C. Chen, Phys. Rev. ST Accel. Beams **9**, 104201 (2006).
- [13] R. J. Bhatt, *Inverse Problems in Elliptic Charged-Particle Beams* (Massachusetts Institute of Technology, Cambridge, Massachusetts, 2006).
- [14] F. J. Sacherer, *Transverse Space Charge Effects in Circular Accelerators* (University of California, Berkeley, Lawrence Radiation Laboratory, Berkeley, California, 1968), p. 15.
- [15] C. Chen, R. Pakter, and R. C. Davidson, Phys. Rev. Lett. **79**, 225 (1997).
- [16] R. C. Davidson and H. Qin, *Physics of Intense Charged Particle Beams in High Energy Accelerators* (Imperial College Press, Singapore, 2001).
- [17] R. C. Davidson, *Physics of Nonneutral Plasmas* (World Scientific Publishing Company, 2001).
- [18] V. Danilov, S. Cousineau, S. Henderson, and J. Holmes, Phys. Rev. ST Accel. Beams **6**, 094202 (2003).
- [19] R. Bhatt and C. Chen, Phys. Rev. ST Accel. Beams **8**, 14201 (2005).

Figure Caption

Figure 1 Twisted coordinates.

Figure 2 Plots of the beam envelopes $a(s)$ and $b(s)$ versus the axial distance s for the nonrelativistic elliptic beam in Table 1. The solid curves are the generalized envelope solution, whereas the dotted curves are from the PFB2D simulation.

Figure 3 Plots of 5,000 particles (a sample of the 1×10^5 particles in the PFB2D simulation) in the (x, y) plane and $(x, dy/ds)$ plane for five snapshots within one period: $s/S = 9.0, 9.25, 9.5, 9.75$ and 10.0 for the same beam shown in Fig. 2.

Figure 4 3D OMNITRAK simulation results: (a) image of the simulated beam and (b) plots of the beam envelopes from the 3D OMNITRAK simulation (dotted curves) and the theory (solid curves). Here, the parameters of the nonrelativistic ellipse-shaped beam are listed in Table 1.

Figure 5 Plots of the beam envelopes $a(s)$ and $b(s)$ versus the axial distance s for the relativistic elliptic beam in Table 1 with zero temperature. The solid curves are the generalized envelope solution, whereas the dotted curves are from the PFB2D simulation.

Figure 6 Plots of the beam envelopes (a) $a(s)$ and (b) $b(s)$ versus the axial distance s for the relativistic elliptic beam in Table 1 for three different temperature choices: 0 eV, 50 eV and 100 eV.

Figure 7 Plots of the beam envelopes $a(s)$ and $b(s)$ versus the axial distance s for the relativistic elliptic beam in Table 1 for a temperature of 50 eV. The solid curves

are the generalized envelope solution, whereas the dotted curves are from the PFB2D simulation.

Table 1 System parameters for elliptic-beam examples

Parameter	Nonrelativistic	Relativistic
Application	Wireless Communication	ILC
Frequency (GHz)	1.95	1.3
RF Power (kW)	0.2 (cw)	10 (pulsed)
Current (A)	0.11	111.1
Voltage (kV)	2.29	120
a/b	6.0	20
a (cm)	0.373	1.0
S (cm)	1.912	2.2
k_{0y}/k_{0x}	6.0	20
B_0 (kG)	0.263	2.0
B'_q (G/cm)	30.0	80.8

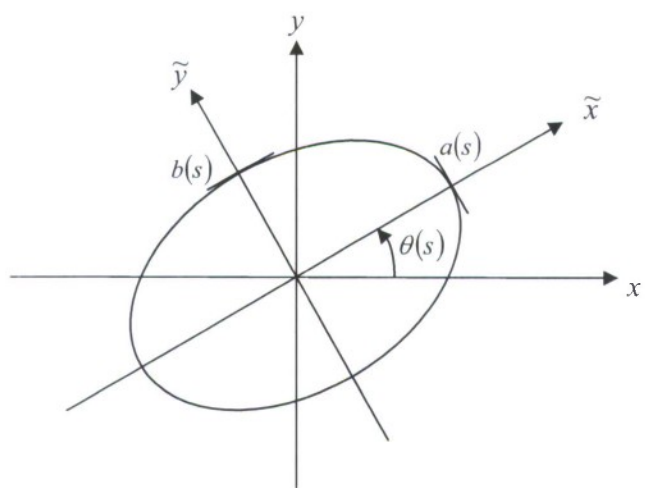


Fig. 1

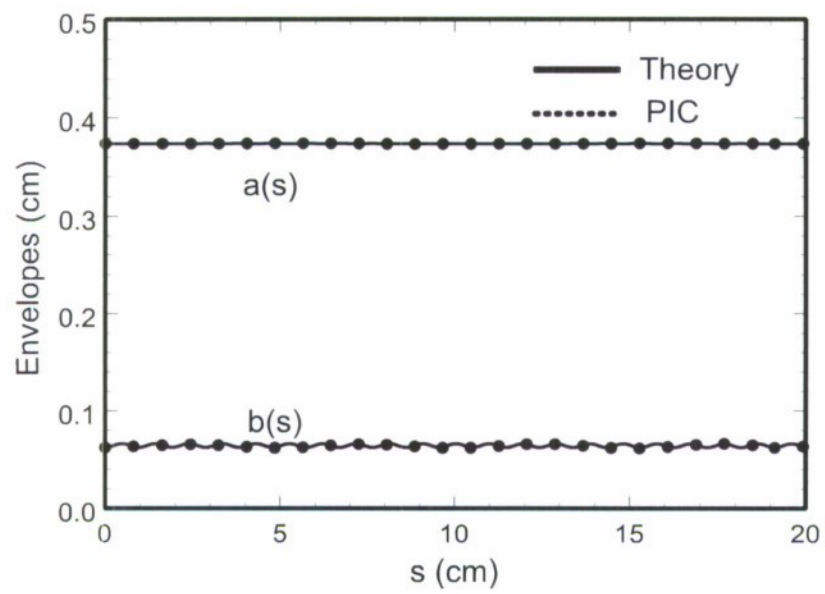


Fig. 2

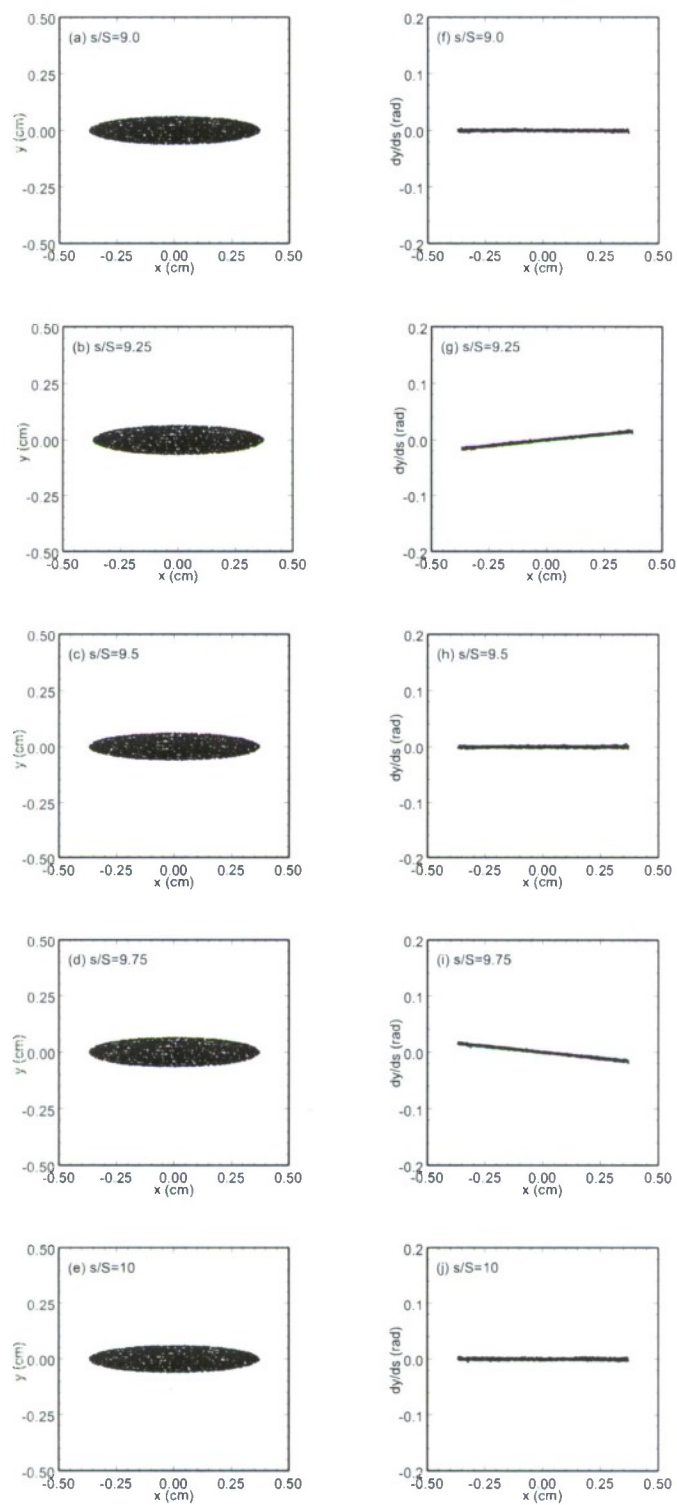


Fig. 3

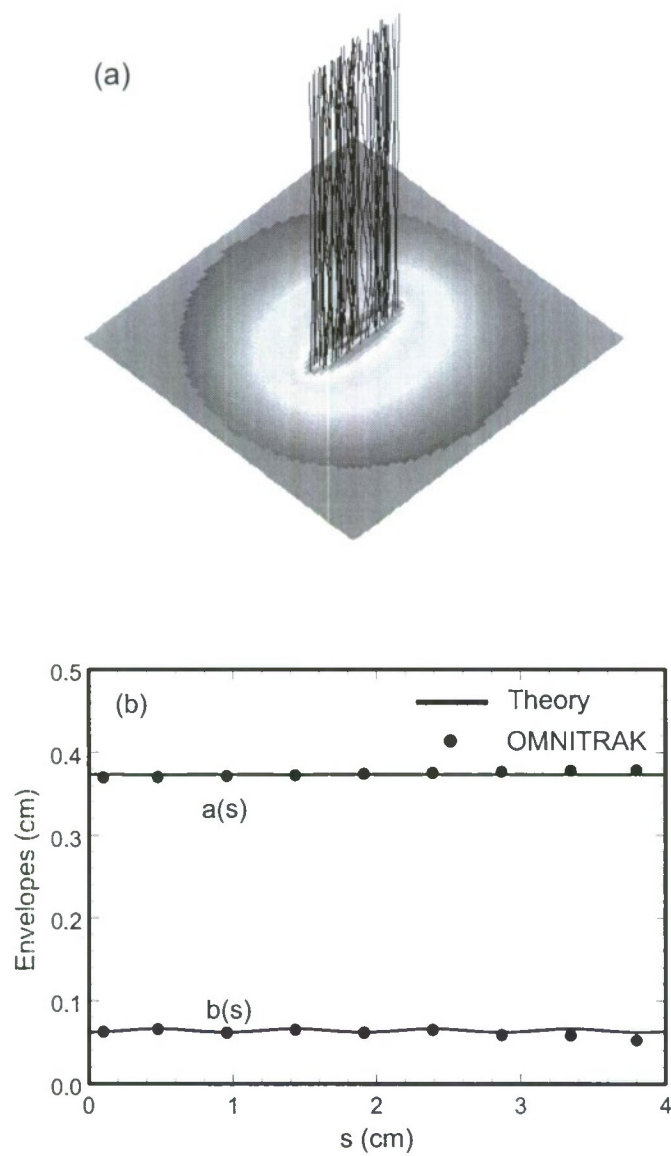


Fig. 4

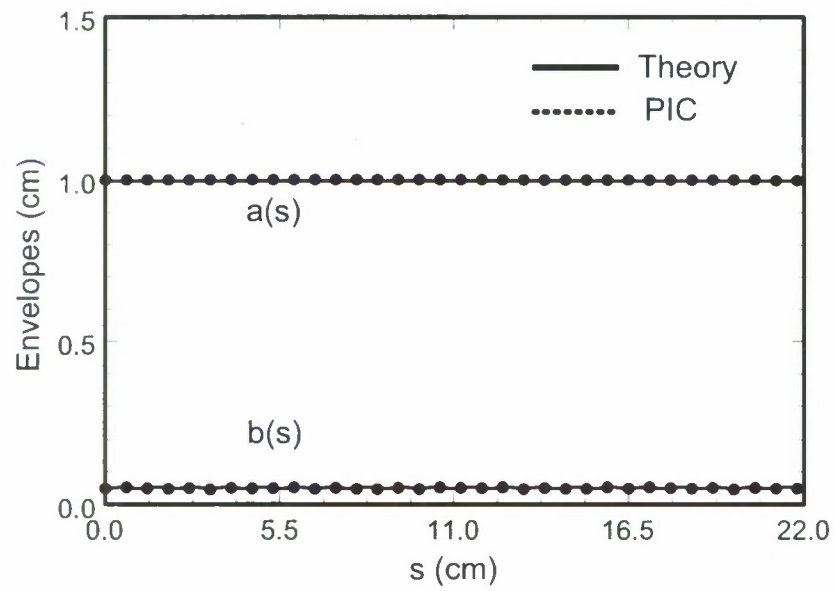


Fig. 5

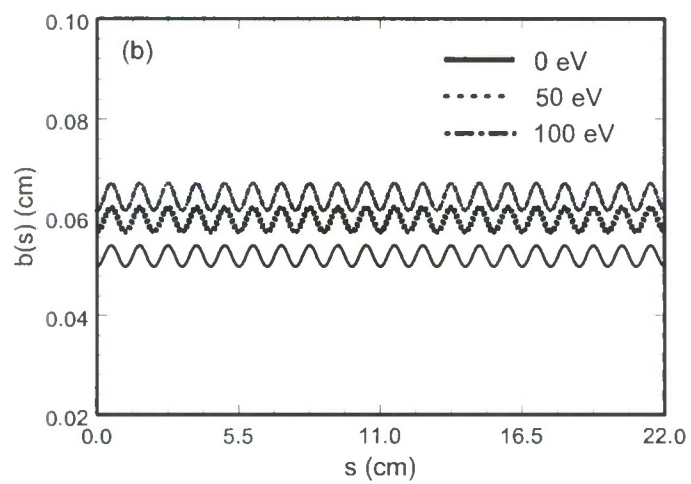
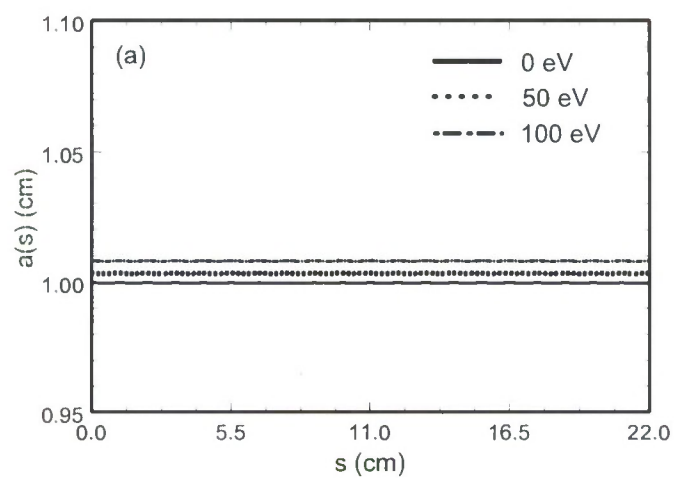


Fig. 6

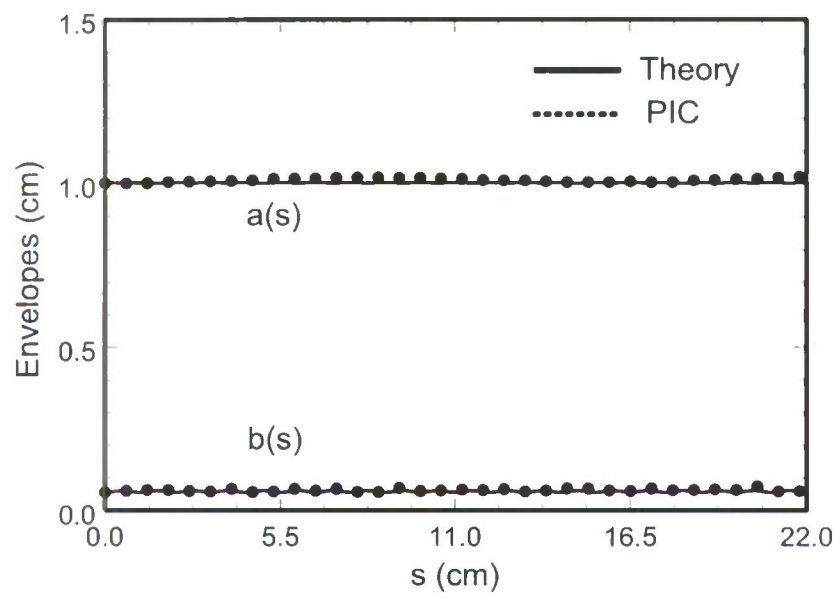


Fig. 7

Appendix A

The derivation of the generalized envelope equations (8)-(12) is as follows. We first solve the continuity equation (1). Substituting the density profile in Eq. (5) and the flow velocity profile in Eq. (6) into Eq (1), we obtain

$$\begin{aligned} & \left[\mu_x + \mu_y - \frac{a'}{a} - \frac{b'}{b} \right] \Theta \left[1 - \frac{\tilde{x}^2}{a^2} - \frac{\tilde{y}^2}{b^2} \right] + 2 \left[\left(\frac{a'}{a} - \mu_x \right) \frac{\tilde{x}^2}{a^2} + \left(\frac{b'}{b} - \mu_y \right) \frac{\tilde{y}^2}{b^2} \right. \\ & \left. + \left(-\frac{b}{a} \theta' + \frac{a}{b} \theta' + \frac{b}{a} \alpha_x - \frac{a}{b} \alpha_y \right) \frac{\tilde{x}\tilde{y}}{ab} \right] \delta \left[1 - \frac{\tilde{x}^2}{a^2} - \frac{\tilde{y}^2}{b^2} \right] = 0, \end{aligned} \quad (\text{A.1})$$

where the prime denotes $\partial/\partial s$, and the relations $\tilde{x}' = \tilde{y}\theta'$, $\tilde{y}' = -\tilde{x}\theta'$, $\partial \mathbf{e}_{\tilde{x}}/\partial s = \mathbf{e}_{\tilde{y}}\theta'$ and $\partial \mathbf{e}_{\tilde{y}}/\partial s = -\mathbf{e}_{\tilde{x}}\theta'$ have been used. Since Eq. (A.1) must be satisfied for all \tilde{x} and \tilde{y} , the coefficients of the terms proportional to Θ , $\tilde{x}^2\delta$, $\tilde{y}^2\delta$ and $\tilde{x}\tilde{y}\delta$ must vanish independently. This leads to the following equations

$$\mu_x = \frac{1}{a} \frac{da}{ds}, \quad (\text{A.2})$$

$$\mu_y = \frac{1}{b} \frac{db}{ds}, \quad (\text{A.3})$$

$$\frac{d\theta}{ds} = \frac{a^2\alpha_y - b^2\alpha_x}{a^2 - b^2}. \quad (\text{A.4})$$

Second, we solve the force balance equation (3). Substituting the density profile in Eq. (5), the flow velocity profile in Eq. (6), and the self-field potential in Eq. (7) into Eq. (3), we obtain two equations in the \tilde{x} – and \tilde{y} – directions, respectively. In the \tilde{x} – direction, we have

$$\begin{aligned}
& \beta_b^2 c^2 \left[(\mu'_x - \alpha_y \theta' + \mu_x^2 - \alpha_x \alpha_y + \alpha_y \theta') \tilde{x} + (-\alpha'_x + \mu_x \theta' - \mu_y \theta' - \alpha_x \mu_x - \alpha_x \mu_y) \tilde{y} \right] \\
& = \frac{q}{\gamma_b m} \left[\frac{1}{\gamma_b^2} \frac{2qN_b}{a+b} \frac{2\tilde{x}}{a} - \beta_b B_{\tilde{y}} + (\mu_y \tilde{y} + \alpha_y \tilde{x}) \beta_b B_z \right].
\end{aligned} \tag{A.5}$$

In the \tilde{y} - direction, we have

$$\begin{aligned}
& \beta_b^2 c^2 \left[(\alpha'_y - \mu_y \theta' + \mu_x \theta' + \alpha_y \mu_x + \alpha_y \mu_y) \tilde{x} + (\mu'_y + \alpha_y \theta' - \alpha_x \theta' + \mu_y^2 - \alpha_x \alpha_y) \tilde{y} \right] \\
& = \frac{q}{\gamma_b m} \left[\frac{1}{\gamma_b^2} \frac{2qN_b}{a+b} \frac{2\tilde{y}}{a} + \beta_b B_{\tilde{x}} - (\mu_x \tilde{x} - \alpha_x \tilde{y}) \beta_b B_z \right].
\end{aligned} \tag{A.6}$$

We can rewrite Eqs. (A.5) and (A.6) as

$$f_x \tilde{x} + g_y \tilde{y} = 0, \tag{A.7}$$

$$g_x \tilde{x} + f_y \tilde{y} = 0, \tag{A.8}$$

where

$$f_x = \mu'_x - \alpha_y \theta' + \mu_x^2 - \alpha_x \alpha_y + \alpha_x \theta' - \frac{2K}{a(a+b)} - 2\sqrt{\kappa_z(s)} \alpha_y + \frac{q}{\gamma_b \beta_b m c^2} B_{\tilde{y}\tilde{x}}, \tag{A.9}$$

$$f_y = \mu'_y + \alpha_y \theta' - \alpha_x \theta' + \mu_y^2 - \alpha_x \alpha_y - \frac{2K}{b(a+b)} - 2\sqrt{\kappa_z(s)} \alpha_x - \frac{q}{\gamma_b \beta_b m c^2} B_{\tilde{x}\tilde{y}}, \tag{A.10}$$

$$g_x = \alpha'_y - \mu_y \theta' + \mu_x \theta' + \alpha_y \mu_x + \alpha_y \mu_y + 2\sqrt{\kappa_z(s)} \mu_x - \frac{q}{\gamma_b \beta_b m c^2} B_{\tilde{x}\tilde{x}}, \tag{A.11}$$

$$g_y = -\alpha'_x + \mu_x \theta' - \mu_y \theta' - \alpha_x \mu_x - \alpha_x \mu_y - 2\sqrt{\kappa_z(s)} \mu_y + \frac{q}{\gamma_b \beta_b m c^2} B_{\tilde{y}\tilde{y}}, \tag{A.12}$$

with the definitions of

$$\sqrt{\kappa_z(s)} \equiv \frac{qB_z(s)}{2\gamma_b \beta_b m c^2} \text{ and } K \equiv \frac{2q^2 N_b}{\gamma_b^3 \beta_b^3 m c^2}. \tag{A.13}$$

We can express the magnetic field in Eq. (4) in the twisted coordinate as

$$\mathbf{B} = B_z(s)\mathbf{e}_z + (B_{\tilde{x}\tilde{x}}\tilde{x} + B_{\tilde{x}\tilde{y}}\tilde{y})\mathbf{e}_{\tilde{x}} + (B_{\tilde{y}\tilde{x}}\tilde{x} + B_{\tilde{y}\tilde{y}}\tilde{y})\mathbf{e}_{\tilde{y}}, \quad (\text{A.14})$$

where the magnetic fields contributions are

$$B_{\tilde{x}\tilde{x}} = -\frac{dB_z(s)}{ds} \left[\frac{k_{0x}^2}{k_0^2} \cos^2 \theta(s) + \frac{k_{0y}^2}{k_0^2} \sin^2 \theta(s) \right] + 2B'_q \sin \theta(s) \cos \theta(s), \quad (\text{A.14})$$

$$B_{\tilde{x}\tilde{y}} = -\frac{dB_z(s)}{ds} \left(-\frac{k_{0x}^2}{k_0^2} + \frac{k_{0y}^2}{k_0^2} \right) \cos \theta(s) \sin \theta(s) + B'_q [\cos^2 \theta(s) - \sin^2 \theta(s)], \quad (\text{A.15})$$

$$B_{\tilde{y}\tilde{x}} = -\frac{dB_z(s)}{ds} \left(-\frac{k_{0x}^2}{k_0^2} + \frac{k_{0y}^2}{k_0^2} \right) \cos \theta(s) \sin \theta(s) + B'_q [\cos^2 \theta(s) - \sin^2 \theta(s)], \quad (\text{A.16})$$

$$B_{\tilde{y}\tilde{y}} = -\frac{dB_z(s)}{ds} \left[\frac{k_{0x}^2}{k_0^2} \sin^2 \theta(s) + \frac{k_{0y}^2}{k_0^2} \cos^2 \theta(s) \right] - 2B'_q \sin \theta(s) \cos \theta(s). \quad (\text{A.17})$$

Since Eq. (A.7) and (A.8) must be satisfied for all \tilde{x} and \tilde{y} , the coefficients of the terms proportional to \tilde{x} and \tilde{y} must vanish independently, which lead to

$$f_x = 0, \quad (\text{A.18})$$

$$f_y = 0, \quad (\text{A.19})$$

$$g_x = 0, \quad (\text{A.20})$$

$$g_y = 0. \quad (\text{A.21})$$

Substituting Eqs. (A.2)-(A.4) into Eqs. (A.18)-(A.21), we obtain

$$\begin{aligned}
f_x &= \mu'_x - \alpha_y \theta' + \mu_x^2 - \alpha_x \alpha_y + \alpha_x \theta' - \frac{2K}{a(a+b)} - 2\sqrt{\kappa_z(s)}\alpha_y + \frac{qB_{\widetilde{y\widetilde{x}}}}{\gamma_b \beta_b mc^2} \\
&= \frac{d}{ds} \left(\frac{a'}{a} \right) + \left(\frac{a'}{a} \right)^2 + (\alpha_x - \alpha_y) \frac{a^2 \alpha_y - b^2 \alpha_x}{a^2 - b^2} - \alpha_x \alpha_y - \frac{2K}{a(a+b)} - 2\sqrt{\kappa_z(s)}\alpha_y + \frac{qB_{\widetilde{y\widetilde{x}}}}{\gamma_b \beta_b mc^2} \\
&= \frac{1}{a} \frac{d^2 a}{ds^2} - \frac{b^2 (\alpha_x^2 - 2\alpha_x \alpha_y) + a^2 \alpha_y^2}{a^2 - b^2} - \frac{2K}{a(a+b)} - 2\sqrt{\kappa_z(s)}\alpha_y + \frac{qB_{\widetilde{y\widetilde{x}}}}{\gamma_b \beta_b mc^2} \\
&= 0,
\end{aligned} \tag{A.22}$$

$$\begin{aligned}
f_y &= \mu'_y + \alpha_y \theta' - \alpha_x \theta' + \mu_y^2 - \alpha_x \alpha_y - \frac{2K}{b(a+b)} - 2\sqrt{\kappa_z(s)}\alpha_x - \frac{qB_{\widetilde{x\widetilde{y}}}}{\gamma_b \beta_b mc^2} \\
&= \frac{d}{ds} \left(\frac{b'}{b} \right) + \left(\frac{b'}{b} \right)^2 - (\alpha_x - \alpha_y) \frac{a^2 \alpha_y - b^2 \alpha_x}{a^2 - b^2} - \alpha_x \alpha_y - \frac{2K}{b(a+b)} - 2\sqrt{\kappa_z(s)}\alpha_x - \frac{qB_{\widetilde{x\widetilde{y}}}}{\gamma_b \beta_b mc^2} \\
&= \frac{1}{b} \frac{d^2 b}{ds^2} + \frac{a^2 (\alpha_y^2 - 2\alpha_x \alpha_y) + b^2 \alpha_x^2}{a^2 - b^2} - \frac{2K}{b(a+b)} - 2\sqrt{\kappa_z(s)}\alpha_x - \frac{qB_{\widetilde{x\widetilde{y}}}}{\gamma_b \beta_b mc^2} \\
&= 0,
\end{aligned} \tag{A.23}$$

$$\begin{aligned}
g_x &= \alpha'_y - \mu_y \theta' + \mu_x \theta' + \alpha_y \mu_x + \alpha_y \mu_y + 2\sqrt{\kappa_z(s)}\mu_x - \frac{qB_{\widetilde{x\widetilde{x}}}}{\gamma_b \beta_b mc^2} \\
&= \alpha'_y + (\mu_x - \mu_y) \frac{a^2 \alpha_y - b^2 \alpha_x}{a^2 - b^2} + \alpha_y \left(\frac{a'}{a} + \frac{b'}{b} \right) + 2\sqrt{\kappa_z(s)}\mu_x - \frac{qB_{\widetilde{x\widetilde{x}}}}{\gamma_b \beta_b mc^2} \\
&= \frac{1}{a^2} \frac{d}{ds} (a^2 \alpha_y) - \frac{1}{a} \frac{b^3 (\alpha_x - \alpha_y)}{a^2 - b^2} \frac{d}{ds} \left(\frac{a}{b} \right) + 2 \frac{a'}{a} \sqrt{\kappa_z(s)} - \frac{qB_{\widetilde{x\widetilde{x}}}}{\gamma_b \beta_b mc^2} \\
&= 0,
\end{aligned} \tag{A.24}$$

$$\begin{aligned}
g_y &= -\alpha'_x + \mu_x \theta' - \mu_y \theta' - \alpha_x \mu_x - \alpha_x \mu_y - 2\sqrt{\kappa_z(s)}\mu_y + \frac{qB_{\widetilde{y\widetilde{y}}}}{\gamma_b \beta_b mc^2} \\
&= -\alpha'_x + (\mu_x - \mu_y) \frac{a^2 \alpha_y - b^2 \alpha_x}{a^2 - b^2} - \alpha_x \left(\frac{a'}{a} + \frac{b'}{b} \right) - 2\sqrt{\kappa_z(s)}\mu_y + \frac{qB_{\widetilde{y\widetilde{y}}}}{\gamma_b \beta_b mc^2} \\
&= -\frac{1}{b^2} \frac{d}{ds} (b^2 \alpha_x) + \frac{1}{b} \frac{a^3 (\alpha_x - \alpha_y)}{a^2 - b^2} \frac{d}{ds} \left(\frac{b}{a} \right) - 2\sqrt{\kappa_z(s)} \frac{b'}{b} + \frac{qB_{\widetilde{y\widetilde{y}}}}{\gamma_b \beta_b mc^2} \\
&= 0.
\end{aligned} \tag{A.25}$$

The generalized envelope equations are

$$\frac{d^2 a}{ds^2} - \frac{b^2(\alpha_x^2 - 2\alpha_x\alpha_y) + a^2\alpha_y^2}{a^2 - b^2} a - \frac{2K}{(a+b)} - 2\sqrt{\kappa_z(s)}\alpha_y a + \frac{qB_{\widetilde{y\widetilde{x}}}}{\gamma_b\beta_b mc^2} a = 0, \quad (\text{A.26})$$

$$\frac{d^2 b}{ds^2} + \frac{a^2(\alpha_y^2 - 2\alpha_x\alpha_y) + b^2\alpha_x^2}{a^2 - b^2} b - \frac{2K}{(a+b)} - 2\sqrt{\kappa_z(s)}\alpha_x b - \frac{qB_{\widetilde{x\widetilde{y}}}}{\gamma_b\beta_b mc^2} b = 0, \quad (\text{A.27})$$

$$\frac{d}{ds}(a^2\alpha_y) - \frac{ab^3(\alpha_x - \alpha_y)}{a^2 - b^2} \frac{d}{ds}\left(\frac{a}{b}\right) + 2a'a\sqrt{\kappa_z(s)} - \frac{qB_{\widetilde{x\widetilde{x}}}}{\gamma_b\beta_b mc^2} a^2 = 0, \quad (\text{A.28})$$

$$\frac{d}{ds}(b^2\alpha_x) - \frac{a^3b(\alpha_x - \alpha_y)}{a^2 - b^2} \frac{d}{ds}\left(\frac{b}{a}\right) + 2b'b\sqrt{\kappa_z(s)} - \frac{qB_{\widetilde{y\widetilde{y}}}}{\gamma_b\beta_b mc^2} b^2 = 0, \quad (\text{A.29})$$

$$\frac{d\theta}{ds} = \frac{a^2\alpha_y - b^2\alpha_x}{a^2 - b^2}. \quad (\text{A.30})$$

Substituting Eqs. (A.14)-(A.17) into Eqs. (A.26)-(A.30), we obtain the set of generalized envelope equations (8)-(12).

Appendix B

In this Appendix, we determine the elements of the matrix $\mathbf{M}(s)$. In order to determine the elements of the matrix $\mathbf{M}(s)$, we make the projection of a four-dimensional (4D) hyperellipsoid to a two dimensional ellipse. Let us first define the 4D hyperellipsoid through the equation

$$\boldsymbol{\chi}^T(s) \cdot \mathbf{L}(s) \cdot \boldsymbol{\chi}(s) = 1, \quad (\text{B.1})$$

where $\mathbf{L}(s) = \mathbf{M}^{-1}(s)$ and

$$\boldsymbol{\chi} = \begin{pmatrix} x_1 \\ x_2 \\ x_3 \\ x_4 \end{pmatrix}. \quad (\text{B.2})$$

We expand Eq. (B.1) as

$$\begin{aligned} 1 = & L_{11}x_1^2 + L_{22}x_2^2 + L_{33}x_3^2 + L_{44}x_4^2 \\ & + 2L_{12}x_1x_2 + 2L_{13}x_1x_3 + 2L_{14}x_1x_4 + 2L_{23}x_2x_3 + 2L_{24}x_2x_4 + 2L_{34}x_3x_4. \end{aligned} \quad (\text{B.3})$$

To project the 4D hyperellipsoid defined by Eq. (B.3) onto the subspace (x_1, x_2, x_3) , we find the extremal points in these coordinates by differentiating Eq. (B.3) implicitly and setting $dx_1 = dx_2 = dx_3 = 0$. In this case, we find

$$x_4 = -\frac{1}{L_{44}}(L_{14}x_1 + L_{24}x_2 + L_{34}x_3), \quad (\text{B.4})$$

which we substitute into Eq. (B.3) to obtain the equation for the 3D ellipsoid that bounds the projection of the 4D hyperellipsoid defined by Eq. (B.3) onto the subspace (x_1, x_2, x_3) , i.e.,

$$\begin{aligned} L_{44} = & (L_{11}L_{44} - L_{14}^2)x_1^2 + (L_{22}L_{44} - L_{24}^2)x_2^2 + (L_{33}L_{44} - L_{34}^2)x_3^2 \\ & + 2(L_{12}L_{44} - L_{14}L_{24})x_1x_2 + 2(L_{13}L_{44} - L_{14}L_{34})x_1x_3 + 2(L_{23}L_{44} - L_{24}L_{34})x_2x_3. \end{aligned} \quad (\text{B.4})$$

The 3D ellipsoid of Eq. (B.4) can be further projected onto the 2D subspace (x_1, x_2) .

We again differentiate Eq. (B.4) implicitly and set $dx_1 = dx_2 = 0$ to obtain

$$x_3 = \frac{(L_{14}L_{34} - L_{13}L_{44})x_1 + (L_{24}L_{34} - L_{23}L_{44})x_2}{L_{33}L_{44} - L_{34}^2}, \quad (\text{B.5})$$

which we substitute into Eq. (B.4) to obtain

$$\begin{aligned} 1 = & \frac{L_{14}^2L_{33} - 2L_{13}L_{14}L_{34} + L_{11}L_{34}^2 + L_{13}^2L_{44} - L_{11}L_{33}L_{44}}{L_{34}^2 - L_{33}L_{44}}x_1^2 \\ & + 2\frac{L_{14}L_{24}L_{33} - L_{14}L_{23}L_{34} - L_{13}L_{24}L_{34} + L_{12}L_{34}^2 + L_{13}L_{23}L_{44} - L_{12}L_{33}L_{44}}{L_{34}^2 - L_{33}L_{44}}x_1x_2 \\ & + \frac{L_{24}^2L_{33} - 2L_{23}L_{24}L_{34} + L_{22}L_{34}^2 + L_{23}^2L_{44} - L_{22}L_{33}L_{44}}{L_{34}^2 - L_{33}L_{44}}x_2^2. \end{aligned} \quad (\text{B.6})$$

Equation (B.6) is the 2D ellipse boundary of the projection of the 4D hyperellipsoid defined by Eq. (B.1) onto the subspace (x_1, x_2) .

Expressing the elements L_{ij} in terms of the elements M_{ij} via the relation

$\mathbf{L}(s) = \mathbf{M}^{-1}(s)$, we obtain after lengthy manipulation,

$$1 = \frac{M_{22}}{M_{11}M_{22} - M_{12}^2}x_1^2 - 2\frac{M_{12}}{M_{11}M_{22} - M_{12}^2}x_1x_2 + \frac{M_{11}}{M_{11}M_{22} - M_{12}^2}x_2^2. \quad (\text{B.6})$$

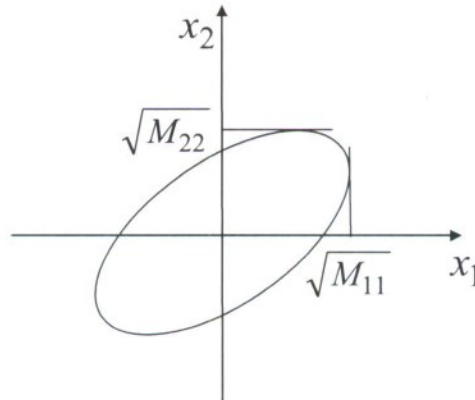


Figure B.1 The boundary ellipse defined in Eq. (B.6).

Note that there are a few useful properties associated with the ellipse defined in Eq. (B.6).

The area bounded by the ellipse is $\pi\sqrt{M_{11}M_{22} - M_{12}^2}$. The maximum extents of the distribution in the x_1 - and x_2 - directions are $\sqrt{M_{11}}$ and $\sqrt{M_{22}}$, respectively, as shown in Fig. B.1.

Since the projection of the 4D hyperellipsoid distribution onto any 2D subspace produces a uniform distribution bounded by the ellipse defined in Eq. (B.6), we can relate the $\mathbf{M}(s)$ matrix elements to the statistical averages,

$$\begin{aligned}
 \langle x_1^2 \rangle &= \frac{\iint x_1^2 dx_1 dx_2}{\iint dx_1 dx_2} \\
 &= \frac{\int_0^{2\pi} \int_0^1 \left(\sqrt{\frac{M_{11}M_{22} - M_{12}^2}{M_{22}}} r \cos \theta + \frac{M_{12}}{\sqrt{M_{22}}} r \sin \theta \right)^2 \sqrt{M_{11}M_{22} - M_{12}^2} r dr d\theta}{\int_0^{2\pi} \int_0^1 \sqrt{M_{11}M_{22} - M_{12}^2} r dr d\theta} \quad (\text{B.7}) \\
 &= \frac{1}{4} M_{11},
 \end{aligned}$$

$$\begin{aligned}
 \langle x_2^2 \rangle &= \frac{\iint x_2^2 dx_1 dx_2}{\iint dx_1 dx_2} \\
 &= \frac{\int_0^{2\pi} \int_0^1 \left(\sqrt{M_{22}} r \sin \theta \right)^2 \sqrt{M_{11}M_{22} - M_{12}^2} r dr d\theta}{\int_0^{2\pi} \int_0^1 \sqrt{M_{11}M_{22} - M_{12}^2} r dr d\theta} \quad (\text{B.8}) \\
 &= \frac{1}{4} M_{22},
 \end{aligned}$$

$$\begin{aligned}
\langle x_1 x_2 \rangle &= \frac{\iint_{\text{ellipse area}} x_1 x_2 dx_1 dx_2}{\iint_{\text{ellipse area}} dx_1 dx_2} \\
&= \frac{\int_0^{2\pi} \int_0^1 \left(\sqrt{\frac{M_{11}M_{22} - M_{12}^2}{M_{22}}} r \cos \theta + \frac{M_{12}}{\sqrt{M_{22}}} r \sin \theta \right) \sqrt{M_{22}} r \sin \theta \sqrt{M_{11}M_{22} - M_{12}^2} r dr d\theta}{\int_0^{2\pi} \int_0^1 \sqrt{M_{11}M_{22} - M_{12}^2} r dr d\theta} \\
&= \frac{1}{4} M_{12},
\end{aligned} \tag{B.9}$$

It follows from Eqs. (B.7)-(B.9) that,

$$\langle x_1^2 \rangle \langle x_2^2 \rangle - \langle x_1 x_2 \rangle^2 = \frac{1}{16} (M_{11}M_{22} - M_{12}^2). \tag{B.10}$$

We use the result in Eq. (B.6) to project the 4D hyperellipsoid defined in Eq. (33) onto the subspace $(x, y) = (x_1, x_3)$. By the definition of the density profile, such a project should produce an elliptic boundary defined by

$$\frac{x^2}{a^2(s)} + \frac{y^2}{b^2(s)} = 1. \tag{B.11}$$

Comparing the coefficients in Eqs. (B.6) and (B.7), we find that $M_{11}(s) = a^2(s)$, $M_{13}(s) = 0$, and $M_{33}(s) = b^2(s)$, which give Eqs. (36.a), (36.f), and (36.c), respectively.

We project the 4D hyperellipsoid defined in Eq. (33) onto the subspace $(x, x') = (x_1, x_2)$ to yield an elliptic boundary. We find that the usual rms emittance is related to the area of the ellipse as

$$\varepsilon_{x\text{rms}}(s) \equiv \sqrt{\langle x^2 \rangle \langle x'^2 \rangle - \langle x x' \rangle^2} = \frac{1}{4} \sqrt{M_{11}M_{22} - M_{12}^2}, \tag{B.12}$$

where $\varepsilon_{xrms}(s)$ is the rms emittance in the x – direction. Using the relation in Eq. (B.9), the correlation coefficient of x and x' is $\langle xx' \rangle / \langle x^2 \rangle = M_{12}/M_{11}$, which allows us to relate the flow velocity defined in Eq. (6) to the element M_{12} as [see Eq. (36.e)]

$$M_{12}(s) = a^2(s)\mu_x(s), \quad (\text{B.13})$$

where use has been made of $\langle xx' \rangle = \langle xV_x/\beta_b c \rangle = \langle \mu_x x^2 \rangle = \frac{1}{4}\mu_x a^2$. Solving Eq. (B.12) yields

$$M_{22}(s) = \frac{16\varepsilon_{xrms}^2(s)}{a^2(s)} + a^2(s)\mu_x^2(s), \quad (\text{B.14})$$

which gives Eq. (36.b).

In a similar manner, we determine the corresponding elements of the matrix $\mathbf{M}(s)$ for the subspace $(y, y') = (x_3, x_4)$, i.e.,

$$M_{34}(s) = b^2(s)\mu_y(s), \quad (\text{B.15})$$

and

$$M_{44}(s) = \frac{16\varepsilon_{yrms}^2(s)}{b^2(s)} + b^2(s)\mu_y^2(s), \quad (\text{B.16})$$

which give Eqs. (36.j) and (36.d), respectively. Here, $\mu_y(s)$ is the flow velocity in the y – direction, and

$$\varepsilon_{yrms}(s) \equiv \sqrt{\langle y^2 \rangle \langle y'^2 \rangle - \langle yy' \rangle^2} = \frac{1}{4} \sqrt{M_{33}M_{44} - M_{34}^2} \quad (\text{B.17})$$

is the rms emittance in the y – direction.

We project the 4D hyperellipsoid defined in Eq. (33) onto the subspace $(x, y') = (x_1, x_4)$ to yield an elliptic boundary describing the coupling of the particle motion between the x - and y' - directions. The projection involves the elements $M_{11}(s)$, $M_{14}(s)$ and $M_{44}(s)$. We use the relation in Eq. (B.9), i.e., $\langle xy' \rangle / \langle x^2 \rangle = M_{14} / M_{11}$ and the definition of the flow velocity in Eq. (6) to express

$$M_{14}(s) = a^2(s) \alpha_y(s) \quad (\text{B.18})$$

where $\alpha_y(s)$ is the rotational flow velocity in the y - direction. Similarly, we have

$$M_{23}(s) = -b^2(s) \alpha_x(s), \quad (\text{B.19})$$

where $\alpha_x(s)$ is the rotational velocity in x - direction. Equations (B.18) and (B.19) give Eqs. (36.g) and (36.h), respectively.

Finally, we project the 4D hyperellipsoid defined in Eq. (33) onto the subspace $(x', y') = (x_2, x_4)$. The correlation of the particle motion between the x' - and y' - directions is calculated to be

$$M_{24}(s) = \langle x'y' \rangle = \frac{\langle x'x \rangle \langle xy' \rangle}{\langle x^2 \rangle} + \frac{\langle x'y \rangle \langle yy' \rangle}{\langle y^2 \rangle} = a^2(s) \mu_x(s) \alpha_y(s) - b^2(s) \mu_y(s) \alpha_x(s). \quad (\text{B.20})$$

which gives Eq. (36.i).



US007381967B2

(12) **United States Patent**
Bhatt et al.

(10) **Patent No.:** **US 7,381,967 B2**

(45) **Date of Patent:** **Jun. 3, 2008**

(54) **NON-AXISYMMETRIC
 CHARGED-PARTICLE BEAM SYSTEM**

6,670,767 B2 * 12/2003 Villa 315/111.61

(75) Inventors: **Ronak J. Bhatt**, Cambridge, MA (US);
Chipling Chen, Needham, MA (US);
Jing Zhou, Cambridge, MA (US)

FOREIGN PATENT DOCUMENTS
 EP 0739492 B 6/2000

(73) Assignee: **Massachusetts Institute of
 Technology**, Cambridge, MA (US)

OTHER PUBLICATIONS

(*) Notice: Subject to any disclaimer, the term of this
 patent is extended or adjusted under 35
 U.S.C. 154(b) by 341 days.

Basten, M.A. et al., "Magnetic Quadrupole Formation of Elliptical
 Sheet Electron Beams for High-Power Microwave Devices" IEEE
 Transactions on Plasma Science, vol. 22, No. 5, Oct. 1994, pp.
 960-966.

Basten, M.A. et al., "Two-plane focusing of high-space-charge
 electron beams using periodically cusped magnetic fields" Journal
 of Applied Physics, New York, vol. 85, No. 9, May 1999, pp.
 6313-6322.

Chen C. et al., "Ideal Matching of Heavy Ion Beams" Nuclear
 Instruments and Methods in Physics Research, Section A: Accelerators,
 Spectrometers, Detectors and Associated Equipment, vol. 464,
 No. 1-3, May 21, 2001, pp. 518-523.

Pierce, J. R., "Rectilinear Electron Flow in Beams," Journal of
 Applied Physics, Aug. 1940, vol. 11, pp. 548-554.

Pirkle D. R. et al., "Pierce-wiggler electron beam system of 250
 GHz gyro-BWO" International Electron Devices Meeting-Technical
 Digest, Dec. 11, 1988, pp. 159-161.

(21) Appl. No.: **11/145,804**

(22) Filed: **Jun. 6, 2005**

(65) **Prior Publication Data**

US 2006/0017002 A1 Jan. 26, 2006

Related U.S. Application Data

(60) Provisional application No. 60/577,132, filed on Jun.
 4, 2004.

(51) Int. Cl.
B01D 59/44 (2006.01)
H01J 49/00 (2006.01)

* cited by examiner

Primary Examiner—Jack Berman
Assistant Examiner—Meenakshi S Sahu

(74) *Attorney, Agent, or Firm*—Gauthier & Connors LLP

(52) U.S. Cl. **250/396 ML**; 313/346 R;
 313/363.1; 315/501; 315/505; 118/50.1; 136/58

(58) **Field of Classification Search** 250/298,
 250/299, 300, 396 ML; 313/346 R, 363.1;
 315/501, 505; 118/50.1; 136/58

See application file for complete search history.

(56) **References Cited**

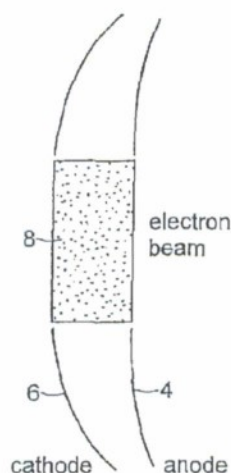
U.S. PATENT DOCUMENTS

2,410,863 A 11/1946 Broadway et al.

(57) **ABSTRACT**

The charged-particle beam system includes a non-axisym-
 metric diode forms a non-axisymmetric beam having an
 elliptic cross-section. A focusing element utilizes a magnetic
 field for focusing and transporting the non-axisymmetric
 beam, wherein the non-axisymmetric beam is approximately
 matched with the channel of the focusing element.

32 Claims, 13 Drawing Sheets



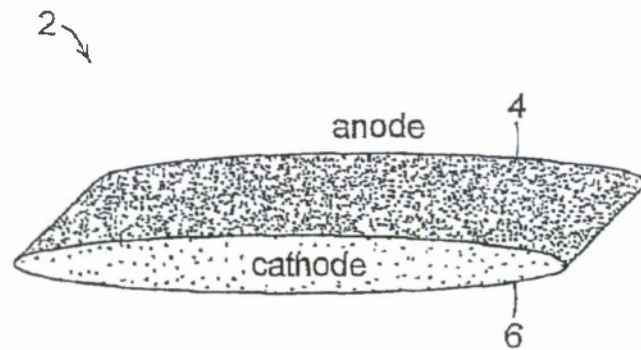


FIG. 1A

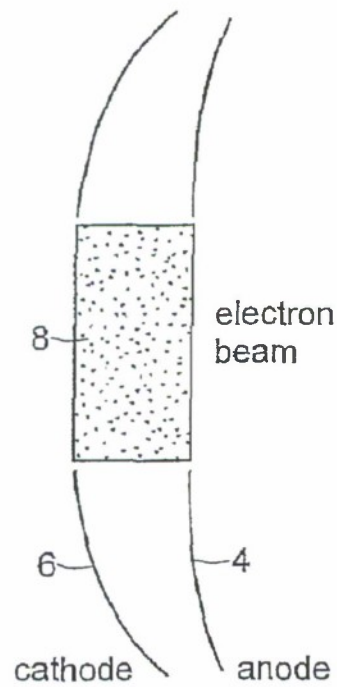


FIG. 1B

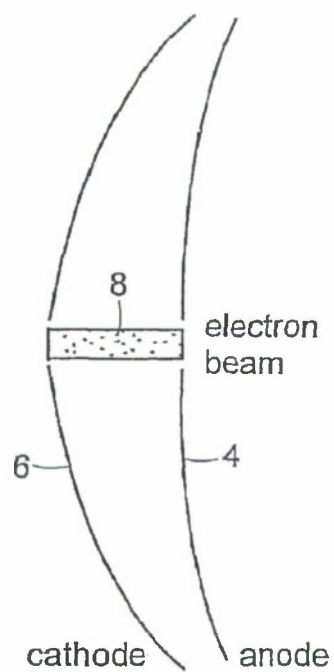


FIG. 1C

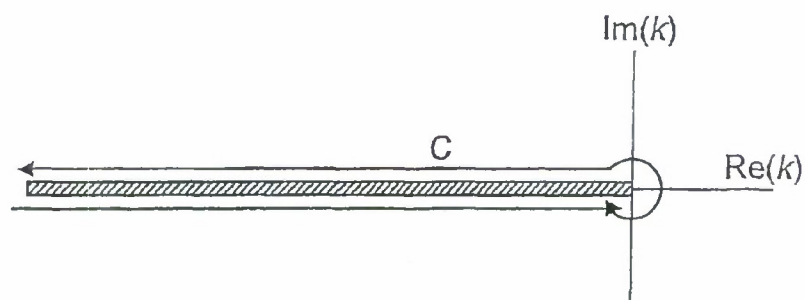


FIG. 2

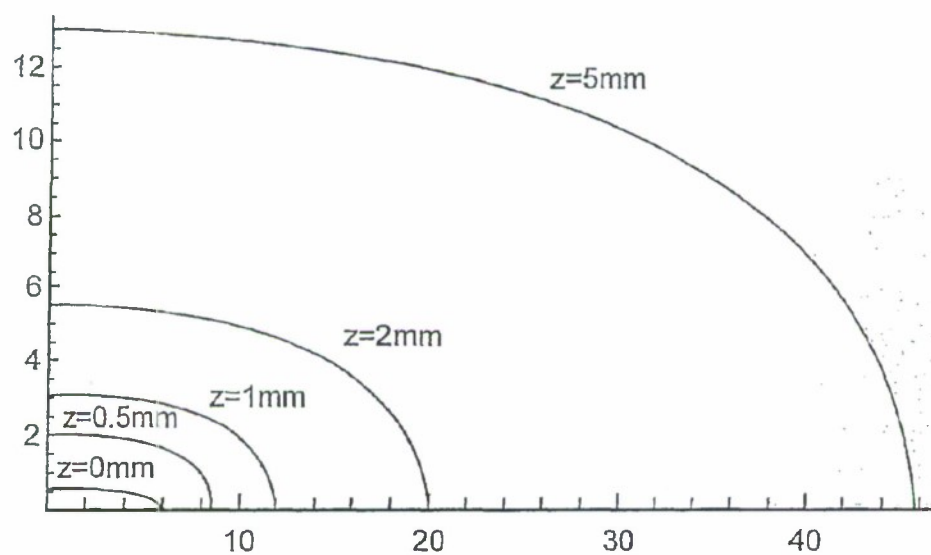


FIG. 3

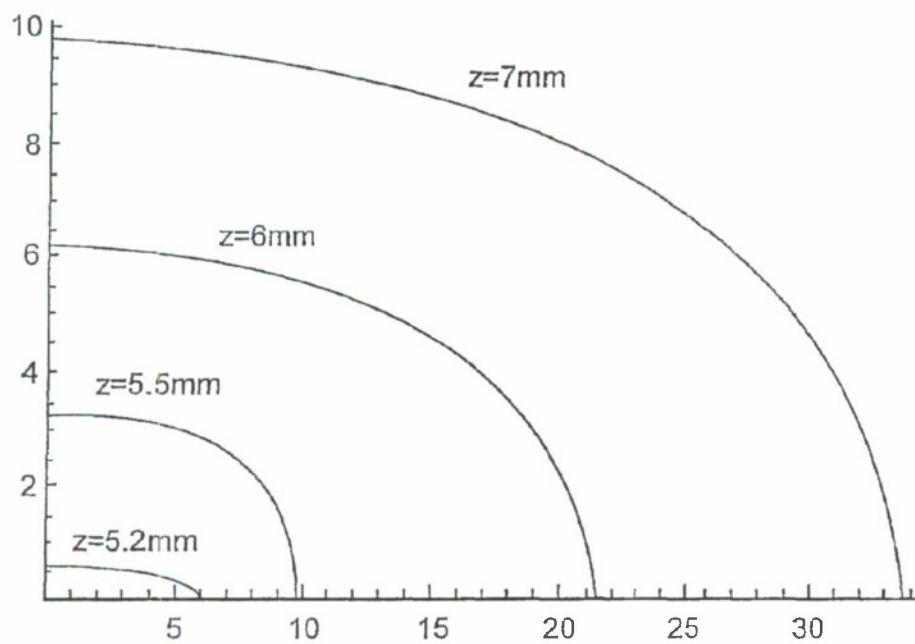


FIG. 4

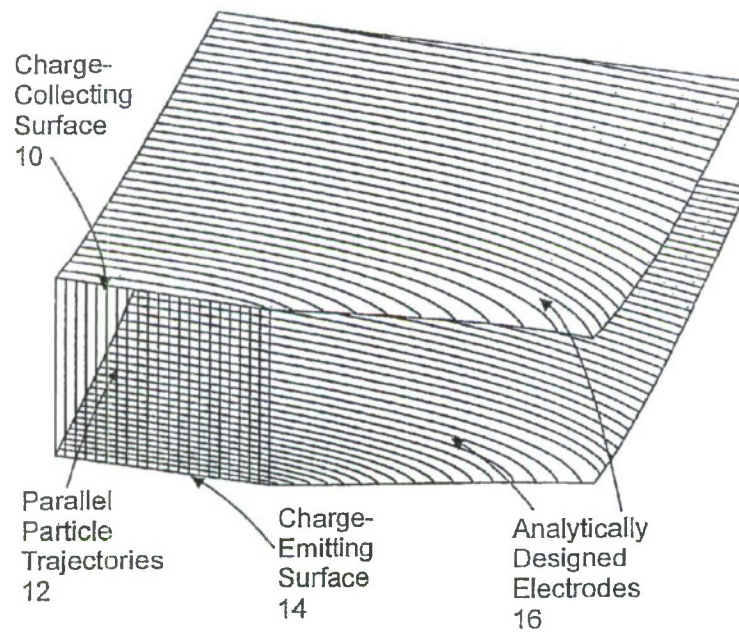


FIG. 5

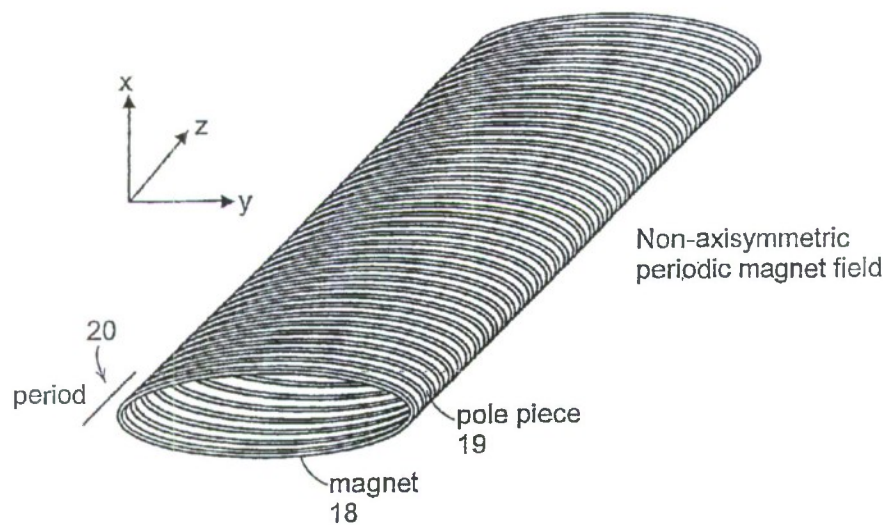
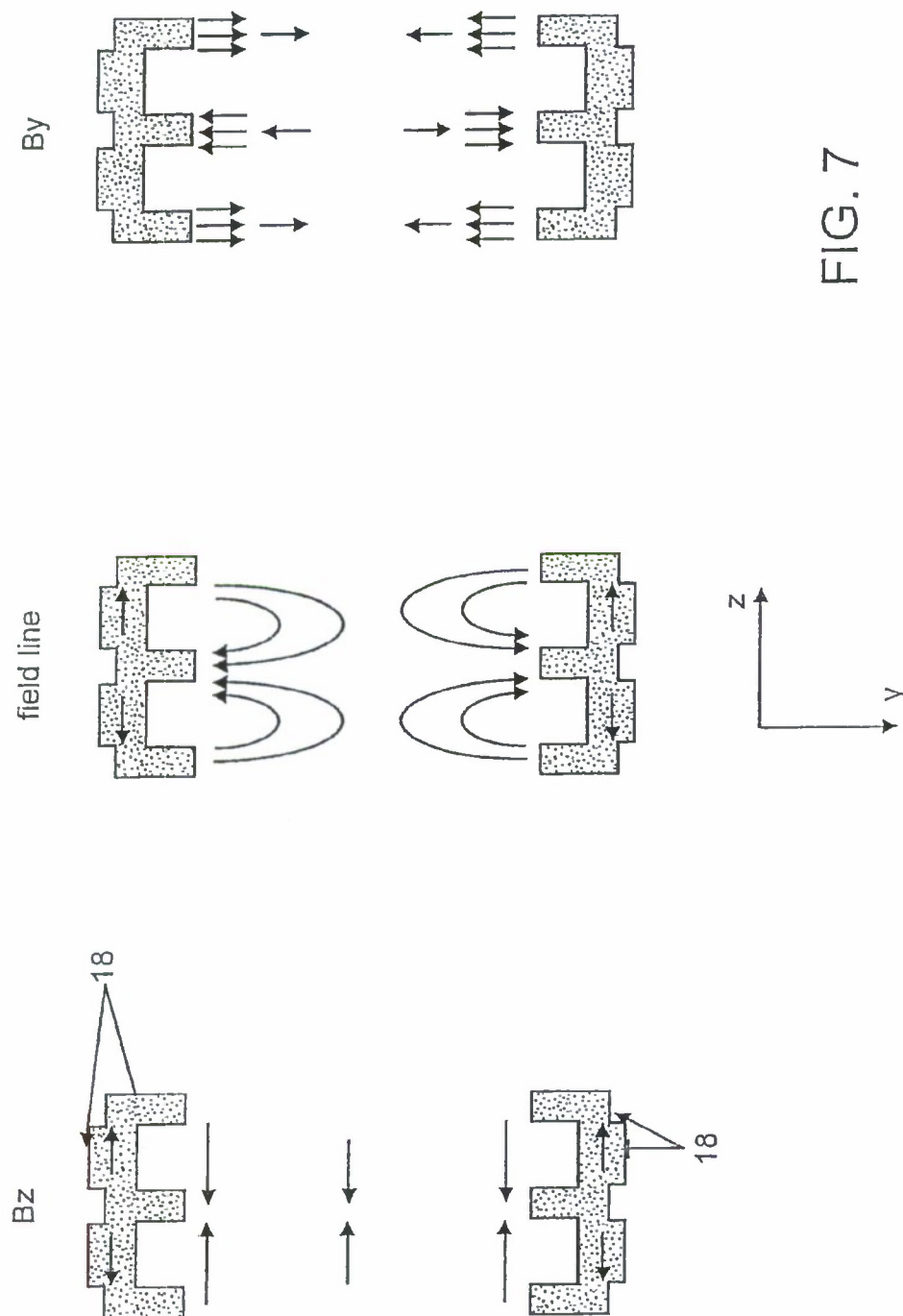


FIG. 6



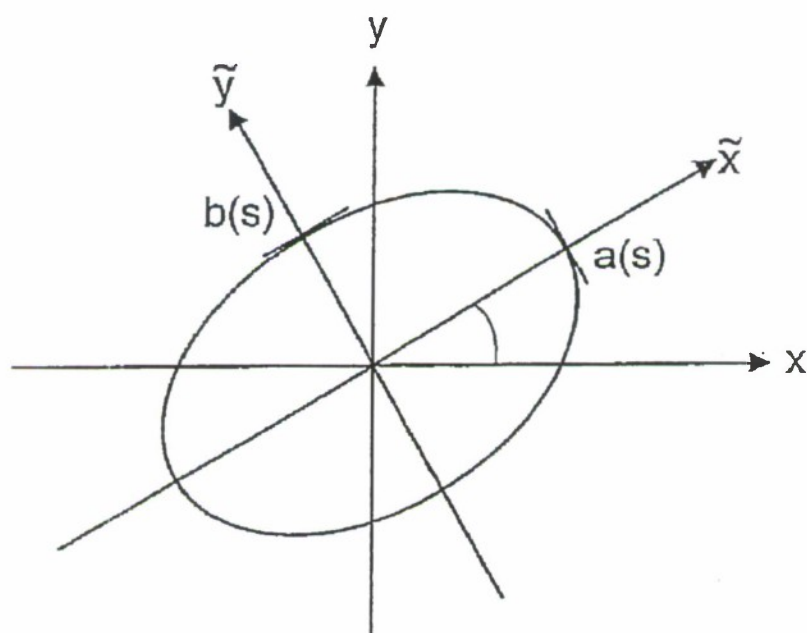


FIG. 8

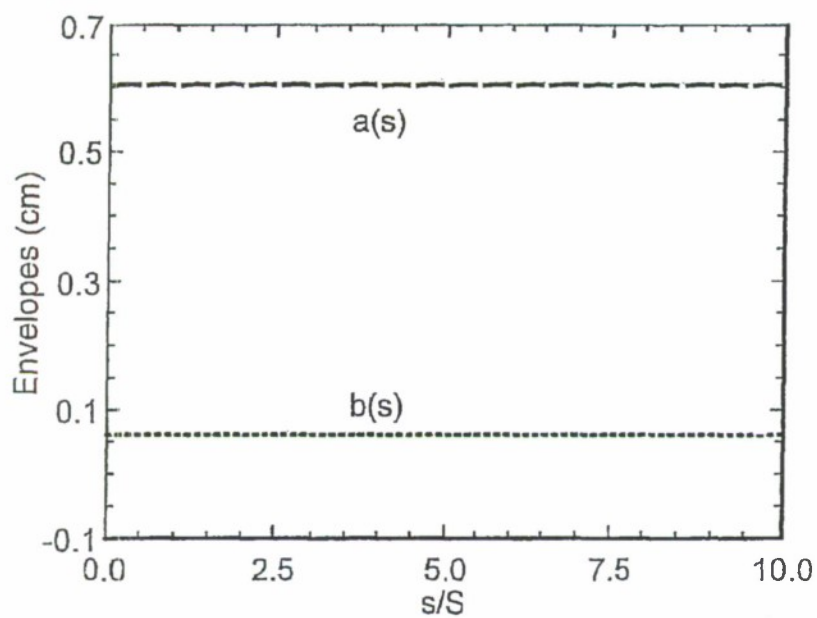


FIG. 9A

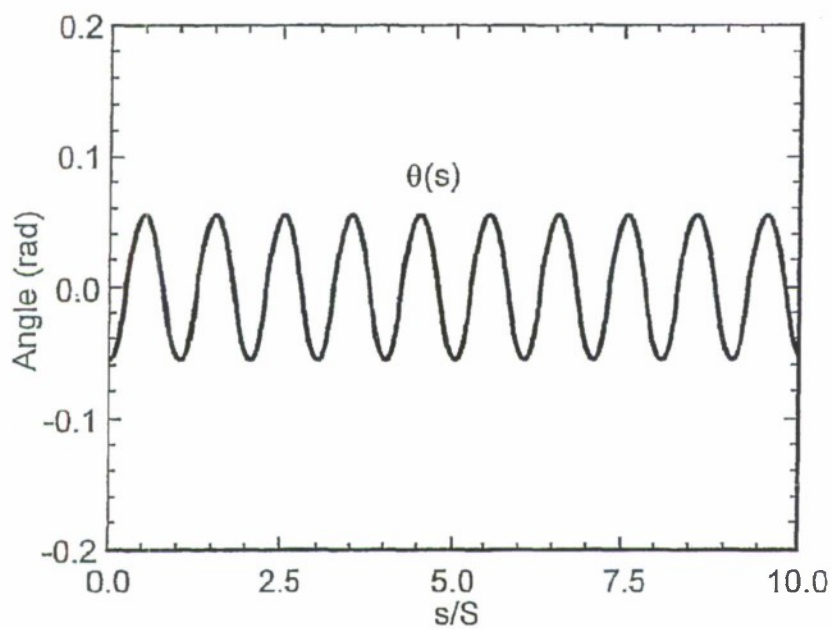


FIG. 9B

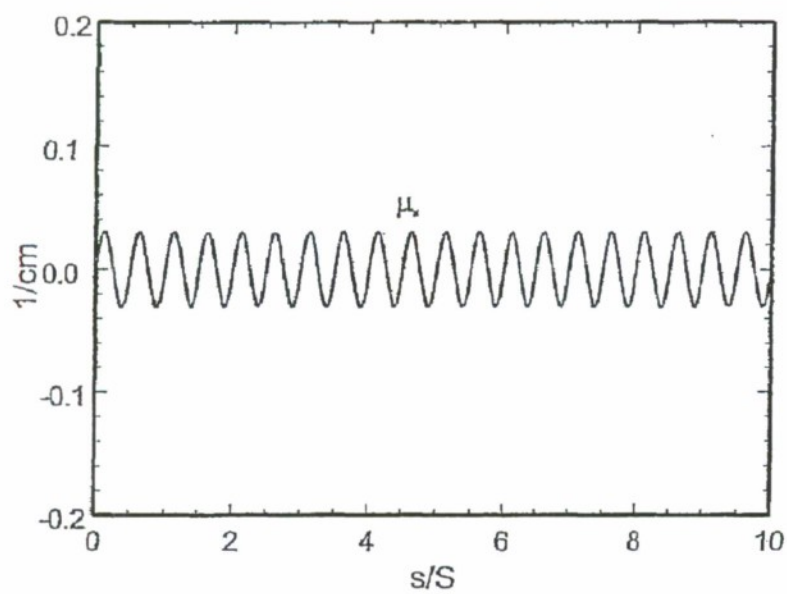


FIG. 9C

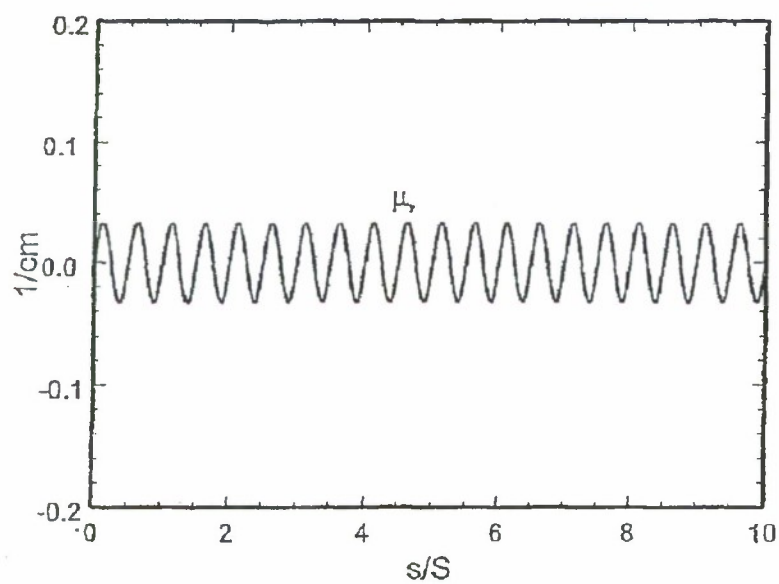


FIG. 9D

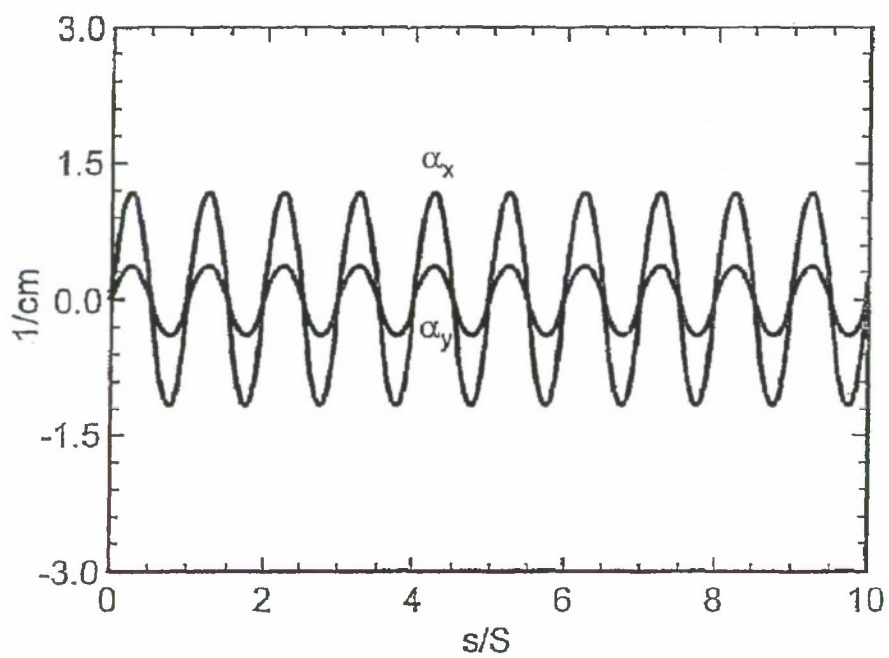


FIG. 9E

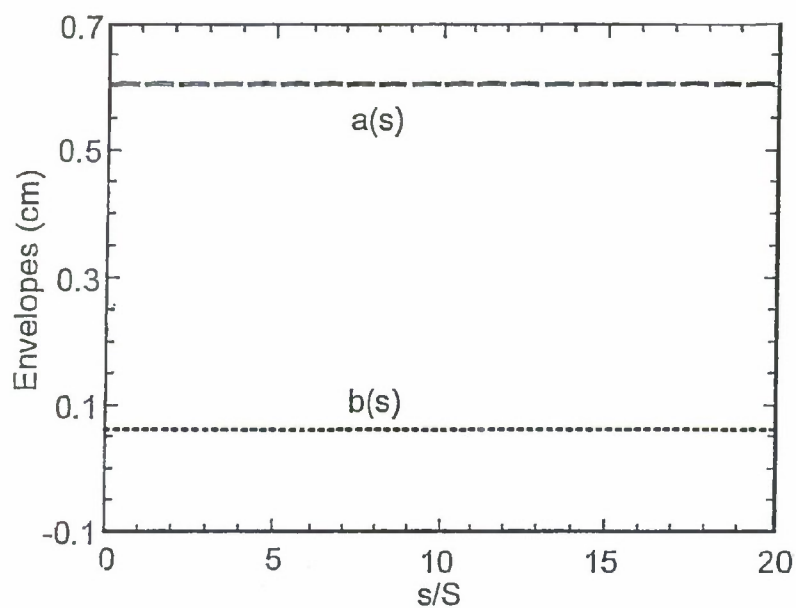


FIG. 10A

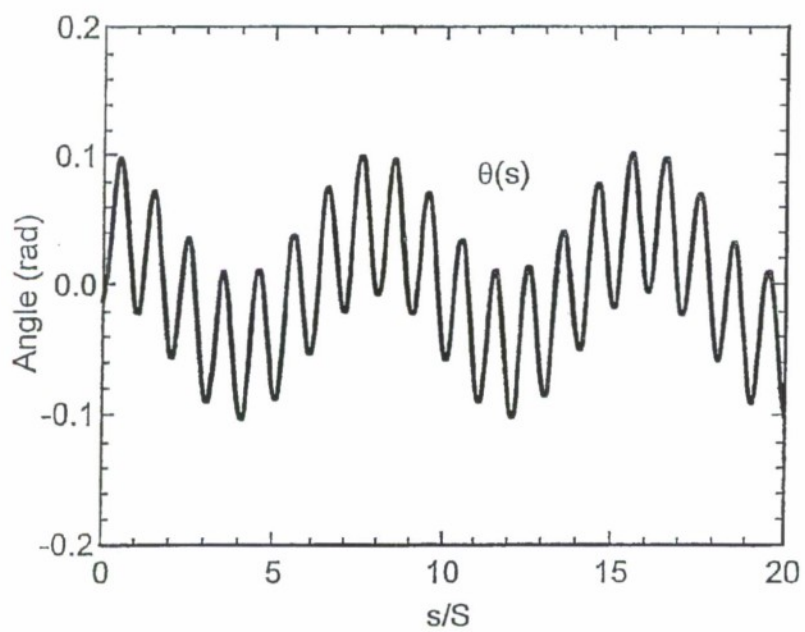


FIG. 10B

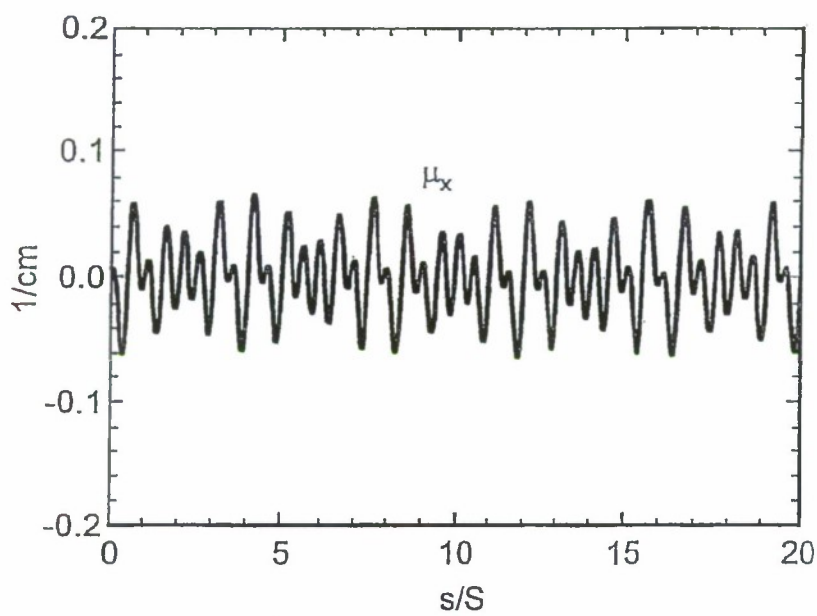


FIG. 10C

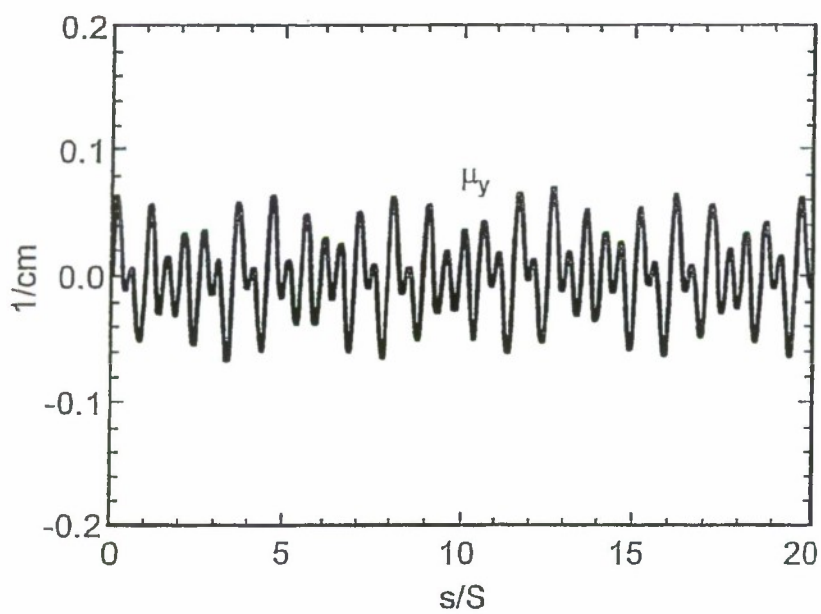


FIG. 10D

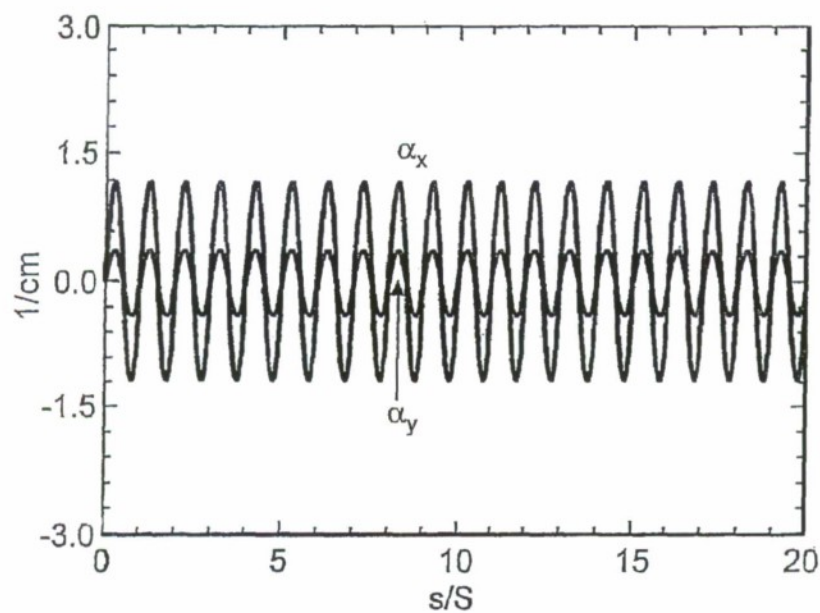


FIG. 10E

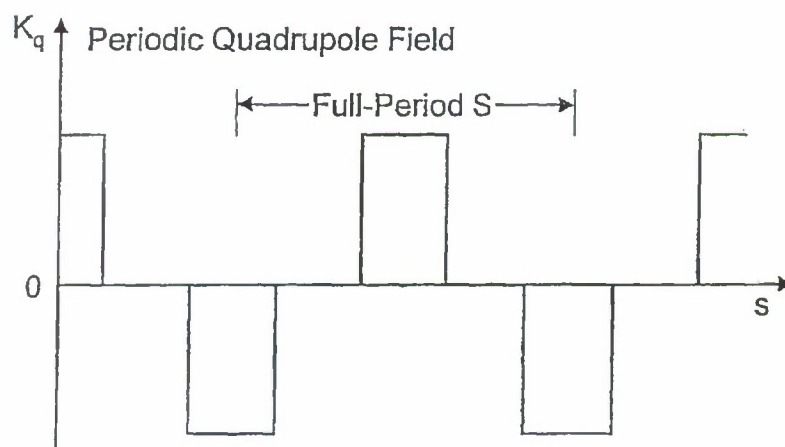


FIG. 11

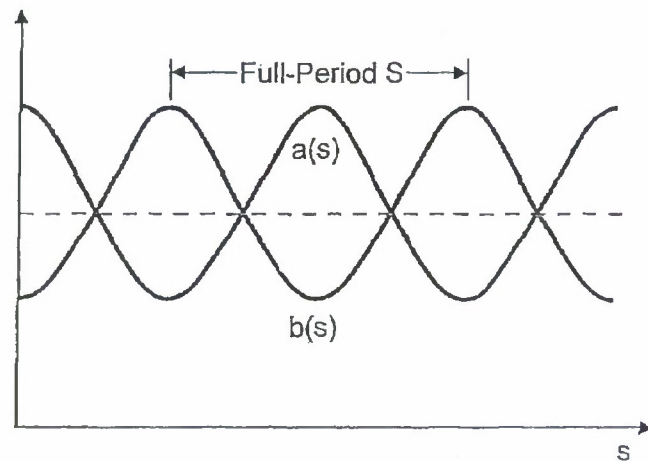


FIG. 12

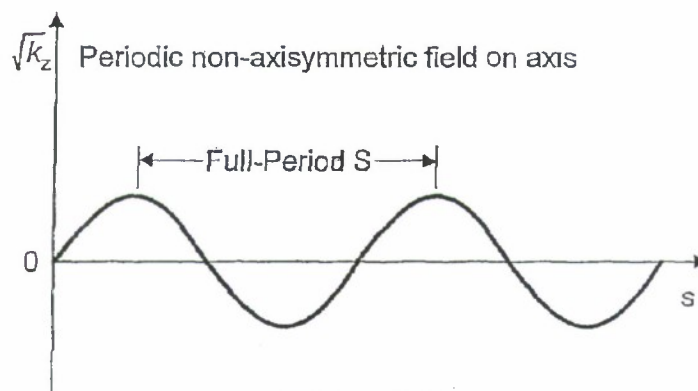


FIG. 13

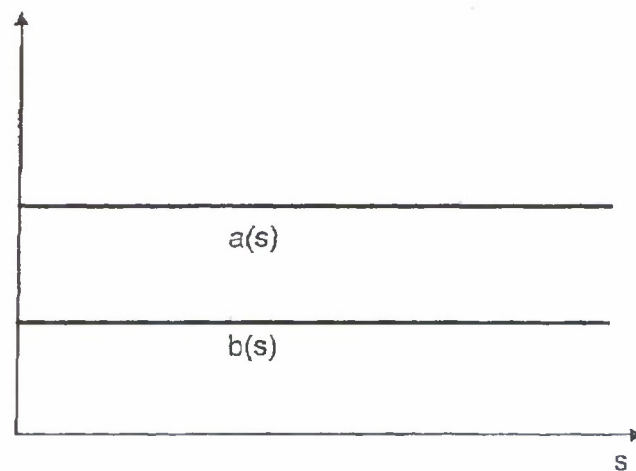


FIG. 14

1

NON-AXISYMMETRIC CHARGED-PARTICLE BEAM SYSTEM

PRIORITY INFORMATION

This application claims priority from provisional application Ser. No. 60/577,132 filed Jun. 4, 2004, which is incorporated herein by reference in its entirety.

BACKGROUND OF THE INVENTION

The invention relates to the field of charged-particle systems, and in particular to a non-axisymmetric charged-particle system.

The generation, acceleration and transport of a high-brightness, space-charge-dominated, charged-particle (electron or ion) beam are the most challenging aspects in the design and operation of vacuum electron devices and particle accelerators. A beam is said to be space-charge-dominated if its self-electric and self-magnetic field energy is greater than its thermal energy. Because the beam brightness is proportional to the beam current and inversely proportional to the product of the beam cross-sectional area and the beam temperature, generating and maintaining a beam at a low temperature is most critical in the design of a high-brightness beam. If a beam is designed not to reside in an equilibrium state, a sizable exchange occurs between the field and mean-flow energy and thermal energy in the beam. When the beam is space-charge-dominated, the energy exchange results in an increase in the beam temperature (or degradation in the beam brightness) as it propagates.

If brightness degradation is not well contained, it can cause beam interception by radio-frequency (RF) structures in vacuum electron devices and particle accelerators, preventing them from operation, especially from high-duty operation. It can also make the beam from the accelerator unusable because of the difficulty of focusing the beam to a small spot size, as often required in accelerator applications.

The design of high-brightness, space-charge-dominated, charged-particle beams relies on equilibrium beam theories and computer modeling. Equilibrium beam theories provide the guideline and set certain design goals, whereas computer modeling provides detailed implementation in the design.

While some equilibrium states are known to exist, matching them between the continuous beam generation section and the continuous beam transport section has been a difficult task for beam designers and users, because none of the known equilibrium states for continuous beam generation can be perfectly matched into any of the known equilibrium states for continuous beam transport.

For example, the equilibrium state from the Pierce diode in round two dimensional (2D) geometry cannot be matched into a periodic quadrupole magnetic field to create a Kapachinskij-Vladimirov (KV) beam equilibrium. A rectangular beam made by cutting off the ends of the equilibrium state from the Pierce diode in infinite, 2D slab geometry ruins the equilibrium state.

However, imperfection of beam matching in the beam system design yields the growth of beam temperature and the degradation of beam brightness as the beam propagates in an actual device.

SUMMARY OF THE INVENTION

According to one aspect of the invention, there is provided a charged-particle beam system. The charged-particle beam system includes a non-axisymmetric diode which

2

forms a non-axisymmetric beam having an elliptic cross-section. A focusing channel utilizes a magnetic field for focusing and transporting a non-axisymmetric beam.

According to another aspect of the invention, there is provided a non-axisymmetric diode. The non-axisymmetric diode comprises at least one electrical terminal for emitting charged-particles and at least one electrical terminal for establishing an electric field and accelerating charged-particles to form a charged-particle beam. These terminals are arranged such that the charged-particle beam possesses an elliptic cross-section.

According to another aspect of the invention, there is provided a method of forming a non-axisymmetric diode comprising forming at least one electrical terminal for emitting charged-particles, forming at least one electrical terminal for establishing an electric field and accelerating charged-particles to form a charged-particle beam, and arranging said terminals such that the charged-particle beam possesses an elliptic cross-section.

According to another aspect of the invention, there is provided a charged-particle focusing and transport channel wherein a non-axisymmetric magnetic field is used to focus and transport a charged-particle beam of elliptic cross-section.

According to another aspect of the invention, there is provided a method of designing a charged-particle focusing and transport channel wherein a non-axisymmetric magnetic field is used to focus and transport a charged-particle beam of elliptic cross-section.

According to another aspect of the invention, there is provided a method of designing an interface for matching a charged-particle beam of elliptic cross section between a non-axisymmetric diode and a non-axisymmetric magnetic focusing and transport channel.

According to another aspect of the invention, there is provided a method of forming a charged-particle beam system. The method includes forming a non-axisymmetric diode that includes a non-axisymmetric beam having an elliptic cross-section. Also, the method includes forming a focusing channel that utilizes a magnetic field for focusing and transporting the elliptic cross-section beam.

BRIEF DESCRIPTION OF THE DRAWINGS

FIGS. 1A-1C are schematic diagrams demonstrating a non-axisymmetric diode;

FIG. 2 is a graph demonstrating the Integration Contour C for the potential Φ ;

FIG. 3 is a graph demonstrating the cross-section of the $\Phi=0$ electrode at various positions along the beam axis;

FIG. 4 is a graph demonstrating the cross-section of the $\Phi=V$ electrode at various positions along the beam axis;

FIG. 5 is a schematic diagram demonstrating the electrode geometry of a well-confined, parallel beam of elliptic cross section;

FIG. 6 is a schematic diagram of a non-axisymmetric periodic magnetic field;

FIG. 7 is a schematic diagram of the field distribution of a non-axisymmetric periodic magnetic field;

FIG. 8 is a schematic diagram demonstrating the laboratory and rotating coordinate systems;

FIGS. 9A-9E are graphs demonstrating matched solutions of the generalized envelope equations for a non-axisymmetric beam system with parameters corresponding to: $k_{0x}=3.22 \text{ cm}^{-1}$, $k_{0y}=5.39 \text{ cm}^{-1}$, $\sqrt{\kappa_z}=0.805 \text{ cm}^{-1}$, $K=1.53 \times 10^{-2}$ and axial periodicity length $S=0.956 \text{ cm}$;

3

FIGS. 10A-10E are graphs demonstrating the envelopes and flow velocities for a non-axisymmetric beam system with the choice of system parameters corresponding to: $k_{0x}=3.22 \text{ cm}^{-1}$, $k_{0y}=5.39 \text{ cm}^{-1}$, $\sqrt{k_z}=0.805 \text{ cm}^{-1}$, $K=1.53 \times 10^{-2}$, axial periodicity length $S=0.956 \text{ cm}$, and a slight mismatch;

FIG. 11 is a graph demonstrating the focusing parameter for a periodic quadrupole magnetic field;

FIG. 12 is a graph demonstrating the beam envelopes of a pulsating elliptic beam equilibrium state in the periodic quadrupole magnetic field shown in FIG. 11;

FIG. 13 is a graph demonstrating the focusing parameter for a non-axisymmetric periodic permanent magnetic field; and

FIG. 14 is a graph demonstrating the beam envelopes of an elliptic beam equilibrium state in the non-axisymmetric periodic permanent magnetic field shown in FIG. 13.

DETAILED DESCRIPTION OF THE INVENTION

The invention comprises a non-axisymmetric charged-particle beam system having a novel design and method of design for non-axisymmetric charged-particle diodes.

A non-axisymmetric diode 2 is shown schematically in FIGS. 1A-1C. FIG. 1A shows the non-axisymmetric diode 2 with a Child-Langmuir electron beam 8 with an elliptic cross-section having an anode 4 and cathode 6. FIG. 1B is a vertical cross-sectional view of the non-axisymmetric diode 2 and FIG. 1C is a horizontal cross-sectional view of the non-axisymmetric diode 2 showing an electron beam 8 and the cathode 6 and anode 4 electrodes.

The electron beam 8 has an elliptic cross section and the characteristics of Child-Langmuir flow. The particles are emitted from the cathode 6, and accelerated by the electric field between the cathode 6 and anode 4. For an ion beam, the roles of cathode and anode are reversed.

To describe the method of designing a non-axisymmetric diode with an elliptic cross-section, one can introduce the elliptic coordinate system $(\xi, \eta, z; f)$, defined in terms of the usual Cartesian coordinates by

$$x=f \cosh(\xi) \cos(\eta), y=f \sinh(\xi) \sin(\eta), z=z \quad (1.1)$$

where $\xi \in [0, \infty)$ is a radial coordinate, $\eta \in [0, 2\pi)$ is an angular coordinate, and f is a constant scaling parameter. A charged-particle beam flowing in the \hat{e}_z direction and taking the Child-Langmuir profile of parallel flow with uniform transverse density will possess an internal electrostatic potential of

$$\Phi(\xi, \eta, z) = V \left(\frac{z}{d} \right)^{4/3}, \quad (1.2)$$

where one can have defined $\Phi(z=0)=0$ along a planar charge-emitting surface and $\Phi(z=d)=V$ along a planar charge-accepting surface.

If both planes have transverse boundaries of elliptic shape, specified by the surface $\xi=\xi_0=\text{constant}$, then a solution exists for a parallel flow, uniform transverse density, Child-Langmuir charged-particle beam of elliptic cross-section, flowing between the planes at $z=0$ and $z=d$. Due to the mutual space-charge repulsion of the particles constituting the beam, this Child-Langmuir profile must be supported by the imposition of an external electric field through the

4

construction of appropriately shaped electrodes. The design of said electrodes requires knowledge of the electrostatic potential function external to the beam which satisfies appropriate boundary conditions on the beam edge:

$$\Phi(\xi_0, \eta, z) = V \left(\frac{z}{d} \right)^{4/3}, \quad (1.3)$$

$$\frac{\partial}{\partial \xi} \Phi(\xi, \eta, z) \Big|_{\xi=\xi_0} = 0.$$

As the potential and its normal derivative are specified independently on the surface $\xi=\xi_0$, this forms an elliptic Cauchy problem, for which standard analytic and numerical solution methods fail due to the exponential growth of errors which is characteristic of all elliptic Cauchy problems. The present technique builds on the 2-dimensional technique of Radley in order to formulate a method of solution for the full 3D problem of determining the electrostatic potential outside a Child-Langmuir charged-particle beam of elliptic cross-section.

In the region external to the beam, the potential satisfies Laplace's equation, which is written in elliptic coordinates as

$$\begin{aligned} 0 &= \frac{1}{F(\xi, \eta, z)} \nabla^2 F(\xi, \eta, z) \\ &= \frac{1}{F(\xi, \eta, z)} \left[\frac{2}{f^2 (\cosh 2\xi - \cos 2\eta)} \left(\frac{\partial^2}{\partial \xi^2} + \frac{\partial^2}{\partial \eta^2} \right) + \frac{\partial^2}{\partial z^2} \right] F(\xi, \eta, z) \\ &= \frac{1}{Z(z)T(\xi, \eta)} \left[\frac{2}{f^2 (\cosh 2\xi - \cos 2\eta)} \left(\frac{\partial^2}{\partial \xi^2} + \frac{\partial^2}{\partial \eta^2} \right) + \frac{\partial^2}{\partial z^2} \right] Z(z)T(\xi, \eta) \\ &= \frac{1}{T(\xi, \eta)} \frac{2}{f^2 (\cosh 2\xi - \cos 2\eta)} \left(\frac{\partial^2}{\partial \xi^2} + \frac{\partial^2}{\partial \eta^2} \right) T(\xi, \eta) + \frac{1}{Z(z)} \frac{\partial^2}{\partial z^2} Z(z), \end{aligned} \quad (1.4)$$

where one can follow the usual technique of separation of variables, writing $F(\xi, \eta, z)=Z(z)T(\xi, \eta)$ and introducing the separation constant k^2 . The separated equations can now be written as

$$0 = \left(\frac{\partial^2}{\partial z^2} - k^2 \right) Z(z), \quad (1.5)$$

$$\begin{aligned} 0 &= \frac{1}{T(\xi, \eta)} \left(\frac{\partial^2}{\partial \xi^2} + \frac{\partial^2}{\partial \eta^2} \right) T(\xi, \eta) + k^2 \frac{f^2}{2} (\cosh 2\xi - \cos 2\eta) \\ &= \frac{1}{R(\xi)} \frac{\partial^2}{\partial \xi^2} R(\xi) + \frac{k^2 f^2}{2} \cosh 2\xi + \frac{1}{\Theta(\eta)} \frac{\partial^2}{\partial \eta^2} \Theta(\eta) - \frac{k^2 f^2}{2} \cos 2\eta. \end{aligned} \quad (1.6)$$

5

where one can have performed another separation on the transverse equation, writing $T(\xi, \eta) = R(\xi)\Theta(\eta)$ and introducing the separation constant a . This last equation thus yields

$$0 = \frac{\partial^2}{\partial \xi^2} R(\xi) - \left(a - \frac{k^2 f^2}{2} \cosh 2\xi \right) R(\xi), \quad (1.7)$$

$$0 = \frac{\partial^2}{\partial \eta^2} \Theta(\eta) + \left(a - \frac{k^2 f^2}{2} \cos 2\eta \right) \Theta(\eta). \quad (1.8)$$

Solutions to the separated transverse equations are known as the Radial Mathieu Functions $R(\xi)$ and Angular Mathieu Functions $\Theta(\eta)$, respectively, while the solutions to the separated longitudinal equation are easily expressed in terms of exponentials $Z(z) \propto e^{\pm kz}$.

The solution for the potential is now represented as a superposition of separable solutions which, jointly, satisfy the boundary conditions on Φ . One can write

$$\Phi(\xi, \eta, z) = \int dk [A(k)e^{kz} B(a)R_a(\xi; k)\Theta_a(\eta; k)da] \quad (1.9)$$

where the amplitude functions $A(k)$ and $B(a)$ are introduced and the integration contours are as yet unspecified. In order to satisfy the boundary condition on Φ along the beam edge, using the analytic continuation of the Gamma function, one can write

$$z^{4/3} = \frac{1}{\Gamma(-\frac{4}{3})} \frac{i}{2\sin(\frac{4\pi}{3})} \int_C e^{kz} k^{-7/3} dk, \quad (1.10)$$

where the integration contour C is taken around the branch cut as shown in FIG. 2.

One can then write the boundary condition as

$$\begin{aligned} \Phi(\xi_0, \eta, z) &= V \left(\frac{z}{d} \right)^{4/3} \\ &= \frac{Vd^{-4/3}}{\Gamma(-\frac{4}{3})} \frac{i}{2\sin(\frac{4\pi}{3})} \int_C e^{kz} k^{-7/3} dk \\ &= \int dk [A(k)e^{kz} B(a)R_a(\xi_0; k)\Theta_a(\eta; k)da]. \end{aligned} \quad (1.11)$$

The boundary condition is satisfied by choosing C as the integration contour for the representation of Φ and making the correspondences

$$A(k) = \frac{Vd^{-4/3}}{\Gamma(-\frac{4}{3})} \frac{i}{2\sin(\frac{4\pi}{3})} k^{-7/3}, \quad (1.12)$$

and

$$\int B(a)R_a(\xi_0; k)\Theta_a(\eta; k)da = 1. \quad (1.13)$$

The physical system requires a solution periodic in η and symmetric about $\eta=0$ and $\eta=\pi/2$. In general, the Angular Mathieu Functions $\Theta_a(\eta)$ are not periodic. Indeed, a periodic solution arises only for certain characteristic eigenvalues of the separation constant a . There are 4 infinite and discrete

6

sets of eigenvalues denoted by $a_{2n}, a_{2n+1}, b_{2n}, b_{2n+1}$ for $N \in \{0, 1, 2, \dots\}$ which differ in their symmetry properties. Only the set a_{2n} and the corresponding cosine-elliptic solutions denoted by $\Theta(\eta) = ce_{2n}(\eta; k)$ possess the appropriate symmetries, and the integral over a becomes a sum of the form

$$1 = \sum_{n=0}^{\infty} B_{2n} R_{a_{2n}}(\xi_0; k) ce_{2n}(\eta; k). \quad (1.14)$$

Moreover, the set of solutions ce_{2n} is orthogonal and complete over the space of functions with the desired symmetry and periodicity properties. Thus one can expand unity as

$$1 = \sum_{n=0}^{\infty} ce_{2n}(\eta; k) \frac{\int_0^{2\pi} ce_{2n}(\eta; k) d\eta}{\int_0^{2\pi} |ce_{2n}(\eta; k)|^2 d\eta}. \quad (1.15)$$

The boundary condition on Φ is then satisfied by choosing

$$B_{2n} = \frac{\int_0^{2\pi} ce_{2n}(\eta; k) d\eta}{\int_0^{2\pi} |ce_{2n}(\eta; k)|^2 d\eta}, \quad (1.16)$$

and

$$R_{a_{2n}}(\xi_0; k) = 1. \quad (1.17)$$

The condition that the normal derivative of the potential vanishes along the beam surface implies

$$\frac{\partial}{\partial \xi} R_{a_{2n}}(\xi; k) \Big|_{\xi=\xi_0} = 0, \quad (1.18)$$

which, along with the boundary value of $R_{a_{2n}}$ and the eigenvalue a_{2n} , fully specify the second-order Radial Mathieu Equation. It can then be integrated by standard methods in order to determine the radial solutions.

Thus, one may rewrite the expansion for Φ as

$$\Phi(\xi, \eta, z) = \frac{Vd^{-4/3}}{\Gamma(-\frac{4}{3})} \frac{i}{2\sin(\frac{4\pi}{3})} \quad (1.19)$$

$$\int_C dk \left[k^{-7/3} e^{kz} \left\{ \sum_{n=0}^{\infty} ce_{2n}(\eta; k) R_{a_{2n}}(\xi; k) \frac{\int_0^{2\pi} ce_{2n}(\eta; k) d\eta}{\int_0^{2\pi} |ce_{2n}(\eta; k)|^2 d\eta} \right\} \right]$$

A number of methods may be used to evaluate the characteristic values a_{2n} and the corresponding Angular Mathieu Functions ce_{2n} . These can be integrated by standard methods. In practice, only the first few terms of the infinite series need be retained in order to reduce fractional errors to below 10^{-5} . The integral along the contour C can be transformed

into definite integrals of complex-valued functions along the real line, and thus it, too, can be evaluated using standard methods.

Once the potential profile is known, one can employ a root-finding technique in order to determine surfaces along which one may place constant-potential electrodes. A numerical module has been developed which determines these electrode shapes based on the theory described and solution methods described above. Sample electrode designs are shown in FIGS. 3 and 4 for the case of a 10:1 elliptical beam of semi-major radius 6 mm and semi-minor radius 0.6 mm. These electrodes serve to enforce the analytically-derived potential profile along the beam edge, which in turn serves to confine the beam and maintain it in the Child-Langmuir form.

The 3-dimensional charged-particle optics tool Omni-Trak has been used to simulate the emission and transport of charge particles in the geometry of FIGS. 3 and 4. The resulting particle trajectories, shown in FIG. 5, are indeed parallel, as predicted by the theory. The results of the Omni-Trak simulation also provide a validation of the analytical method presented above.

One will often wish to extract this beam and inject it into another device by excising a portion of the charge-collecting plate. Doing so will modify the boundary conditions of the problem such that the above solution can no longer be considered exact, however, the errors introduced by relatively small excisions will be negligible, and the appropriate electrode shapes will be substantially unchanged from those produced by the method outlined above.

It should also be noted that additional electrodes, intermediate in potential between the cathode and anode, may be added in order to aid the enforcement of the Child-Langmuir flow condition. The above prescription allows for their design. As with the charge-collecting plate, neither the cathode electrode nor the intermediate electrodes need be extended arbitrarily close to the beam edge in order to enforce the Child-Langmuir flow condition. The portion of these electrodes nearest the beam may be excised without substantially affecting the beam solution.

Along similar lines, in a physical device, one cannot extend the electrodes infinitely far in the transverse directions. The analytically-prescribed electrodes correspond to the surfaces of conductors separated by vacuum and/or other insulating materials and (in some region distant from the beam) deviating from the analytically-prescribed profiles. Nevertheless, as the influence of distant portions of the electrodes diminish exponentially with distance from the beam edge, these deviations will have a negligible effect on the beam profile, provided that they occur at a sufficient distance from the beam edge.

FIG. 5 depicts an Omni-Trak simulation in which the finiteness of the electrodes is evident without affecting the parallel-flow of the charged particle beam. Note FIG. 5 illustrates the charge collection surface 10, charge emitting surface 14, parallel particle trajectories 12, and analytically designed electrodes 16. By equating the electrode geometry with equipotential surfaces, the analytic method of electrode design detailed herein specifies the precise geometry of the charge-emitting 14 and charge-collecting 10 surfaces as well as the precise geometry of external conductors 16. These external conductors may be held at any potential, however, generally, two external conductors are used—one held at the emitter potential and the other at the collector potential. A charged-particle system designed conformally to this geom-

etry will generate a high-quality, laminar, parallel-flow, Child-Langmuir beam of elliptic cross-section as shown in FIG. 5.

As an illustrated example, a non-axisymmetric periodic magnetic field for focusing and transporting a non-axisymmetric beam is shown FIG. 6. FIG. 6 shows the iron pole pieces 18 and magnets 19 used to form the periodic magnetic field. The iron pole pieces are optional and may be omitted in other embodiments. The period of the magnetic field is defined by the line 20. The field distribution is illustrated FIG. 7. Note FIG. 7 illustrates the field lines form by the iron pole pieces 18 and magnets 19 of FIG. 6.

For a high-brightness, space-charge-dominated beam, kinetic (emittance) effects are negligibly small, and the beam can be adequately described by cold-fluid equations. In the paraxial approximation, the steady-state cold-fluid equations for time-stationary flow ($\partial/\partial t=0$) in cgs units are:

$$\beta_b c \frac{\partial}{\partial s} n_b + \nabla_{\perp} \cdot (n_b \mathbf{V}_{\perp}) = 0, \quad (2.1)$$

$$\nabla_{\perp}^2 \phi^s = \beta_b^{-1} \nabla_{\perp}^2 A_z^s = -4\pi q n_b, \quad (2.2)$$

$$n_b \left(\beta_b c \frac{\partial}{\partial s} + \mathbf{V}_{\perp} \cdot \frac{\partial}{\partial \mathbf{x}_{\perp}} \right) \mathbf{V}_{\perp} = \frac{q n_b}{\gamma_b m} \left[-\frac{1}{\gamma_b} \nabla_{\perp} \cdot \phi^s + \beta_b \hat{e}_2 \times \mathbf{B}_{\perp}^{ext} + \frac{\mathbf{V}_{\perp}}{c} \times \mathbf{B}_{\perp}^{ext}(s) \hat{e}_z \right], \quad (2.3)$$

where $s=z$, q and m are the particle charge and rest mass, respectively,

$$\gamma_b = \frac{1}{\sqrt{1 - \beta_b^2}}$$

is the relativistic mass factor, use has been made of $\beta_z = \beta_b = \text{const}$, and the self-electric field E^s and self-magnetic field B^s are determined from the scalar potential ϕ^s and vector potential $A_z^s \hat{e}_z$, i.e., $E^s = -\nabla_{\perp} \phi^s$ and $B^s = \nabla \times A_z^s \hat{e}_z$.

One seeks solutions to Eqs. (2.1)-(2.3) of the form

$$n_b(x_{\perp}, s) = \frac{N_b}{\pi a(s)b(s)} \Theta \left[1 - \frac{\tilde{x}^2}{a^2(s)} - \frac{\tilde{y}^2}{b^2(s)} \right], \quad (2.4)$$

$$\mathbf{V}_{\perp}(x_{\perp}, s) = [\mu_x(s)\tilde{x} - \alpha_x(s)\tilde{y}] \beta_b c \hat{e}_1 + [\mu_y(s)\tilde{y} + \alpha_y(s)\tilde{x}] \beta_b c \hat{e}_2, \quad (2.5)$$

In Eqs. (2.4) and (2.5), $\mathbf{x}_{\perp} = \tilde{x} \hat{e}_1 + \tilde{y} \hat{e}_2$ is a transverse displacement in a rotating frame illustrated in FIG. 8; $\theta(s)$ is the angle of rotation of the ellipse with respect to the laboratory frame; $\Theta(x)=1$ if $x>0$ and $\Theta(x)=0$ if $x<0$; and the functions $a(s)$, $b(s)$, $\mu_x(s)$, $\mu_y(s)$, $\alpha_x(s)$, $\alpha_y(s)$ and $\theta(s)$ are to be determined self-consistently [see Eqs. (2.11)-(2.15)].

For the self-electric and self-magnetic fields, Eqs. (2.2) and (2.4) are solved to obtain the scalar and vector potentials

$$\phi^s = \beta_b^{-1} A_z^s = -\frac{2qN_b}{a+b} \left(\frac{\tilde{x}^2}{a} + \frac{\tilde{y}^2}{b} \right) \quad (2.6)$$

For a 3D non-axisymmetric periodic magnetic field with an axial periodicity length of S , one can describe it as the fundamental mode,

$$B^{(u)}(x) = \quad (2.7)$$

$$B_0 \left[\frac{k_{0x}}{k_0} \sin h(k_{0x}x) \cos h(k_{0y}y) \cos(k_{0z}z) \hat{e}_x + \frac{k_{0y}}{k_0} \cos h(k_{0x}x) \sin h(k_{0y}y) \right.$$

$$\left. \cos(k_{0z}z) \hat{e}_y - \cos h(k_{0x}x) \cos h(k_{0y}y) \sin(k_{0z}z) \hat{e}_z \right],$$

and further expand it to the lowest order in the transverse dimension to obtain

$$B^{(u)}(x) \approx B_0 \left[\frac{k_{0x}^2}{k_0} \cos(k_{0z}z) \hat{e}_x + \frac{k_{0y}^2}{k_0} \cos(k_{0z}z) \hat{e}_y - \sin(k_{0z}z) \hat{e}_z \right] \quad (2.8)$$

$$= B_0 \left[\cos(k_{0z}z) \left(\frac{k_{0x}^2 \cos^2 \theta + k_{0y}^2 \sin^2 \theta}{k_0} \hat{x} - \right. \right.$$

$$\left. \frac{k_{0x}^2 - k_{0y}^2}{2k_0} \sin(2\theta) \hat{y} \right] \hat{e}_x +$$

$$\cos(k_{0z}z) \left(-\frac{k_{0x}^2 - k_{0y}^2}{2k_0} \sin(2\theta) \hat{x} + \right.$$

$$\left. \frac{k_{0x}^2 \sin^2 \theta + k_{0y}^2 \cos^2 \theta}{k_0} \hat{y} \right] \hat{e}_y - \sin(k_{0z}z) \hat{e}_z.$$

In Eqs. (2.7) and (2.8),

$$k_0 = \frac{2\pi}{S}, \quad (2.9)$$

$$k_{0x}^2 + k_{0y}^2 = k_0^2. \quad (2.10)$$

The 3D magnetic field is specified by the three parameters B_0 , S and k_{0x}/k_{0y} .

Using the expressions in Eqs. (2.5), (2.6) and (2.8), it can be shown that both the equilibrium continuity and force equations (2.1) and (2.3) are satisfied if the dynamical variables $a(s)$, $b(s)$, $\mu_x(s) = a^{-1} da/ds$, $\mu_y(s) = b^{-1} db/ds$, $\alpha_x(s)$, $\alpha_y(s)$ and $\theta(s)$ obey the generalized beam envelope equations:

$$\frac{d^2 a}{ds^2} + \left[-\frac{b^2(\alpha_x^2 - 2\alpha_x\alpha_y) + a^2\alpha_y^2}{a^2 - b^2} + \sqrt{\kappa_z} \frac{k_{0x}^2 - k_{0y}^2}{k_0} \cos(k_{0z}z) \sin(2\theta) - \right. \quad (2.11)$$

$$\left. 2\sqrt{\kappa_z} \alpha_y \sin(k_{0z}z) \right] a - \frac{2K}{a+b} = 0,$$

$$\frac{d^2 b}{ds^2} + \left[\frac{a^2(\alpha_y^2 - 2\alpha_x\alpha_y) + b^2\alpha_x^2}{a^2 - b^2} + \sqrt{\kappa_z} \frac{k_{0x}^2 - k_{0y}^2}{k_0} \cos(k_{0z}z) \sin(2\theta) + \right. \quad (2.12)$$

$$\left. 2\sqrt{\kappa_z} \alpha_x \sin(k_{0z}z) \right] b - \frac{2K}{a+b} = 0,$$

$$\frac{d}{ds} (a^2 \alpha_y) - \frac{ab^3(\alpha_x - \alpha_y)}{a^2 - b^2} \frac{d}{ds} \left(\frac{a}{b} \right) -$$

$$2\sqrt{\kappa_z} \cos(k_{0z}z) \frac{k_{0x}^2 \cos^2 \theta + k_{0y}^2 \sin^2 \theta}{k_0} a^2 - 2\sqrt{\kappa_z} a \frac{da}{ds} \sin(k_{0z}z) a = 0, \quad (2.13)$$

-continued

$$\frac{d}{ds} (b^2 \alpha_x) - \frac{a^3 b(\alpha_x - \alpha_y)}{a^2 - b^2} \frac{d}{ds} \left(\frac{b}{a} \right) - \quad (2.14)$$

$$2\sqrt{\kappa_z} \cos(k_{0z}z) \frac{k_{0x}^2 \sin^2 \theta + k_{0y}^2 \cos^2 \theta}{k_0} b^2 - 2\sqrt{\kappa_z} b \frac{db}{ds} \sin(k_{0z}z) = 0, \quad (2.15)$$

$$\frac{d\theta}{ds} = \frac{a^2 \alpha_y - b^2 \alpha_x}{a^2 - b^2}, \text{ where} \quad (2.16)$$

$$\sqrt{\kappa_z} = \frac{qB_0}{2\gamma_b \beta_y m c^2} \text{ and } K = \frac{2q^2 N_b}{\gamma_b^3 \beta_y^2 m c^2}. \quad (2.16)$$

Equations (2.11)-(2.15) have the time reversal symmetry under the transformations $(s, a, b, a', b', \alpha_x, \alpha_y, \theta) \rightarrow (-s, a, b, -a', -b', -\alpha_x, -\alpha_y, \theta)$. This implies that the dynamical system described by Eqs. (2.11)-(2.15) has the hyper symmetry plane $(a', b', \alpha_x, \alpha_y)$.

A numerical module was developed to solve the generalized envelope equations (2.11)-(2.15). There are, in total, seven functions $a(s)$, $b(s)$, $a'(s)$, $b'(s)$, $\alpha_x(s)$, $\alpha_y(s)$ and $\theta(s)$ to be solved. The time inverse symmetry of the dynamical system requires the quantities $(a', b', \alpha_x, \alpha_y)$ vanish at $s=0$ for matched solutions, therefore, only the three initial values $a(0)$, $b(0)$ and $\theta(0)$ corresponding to a matched solution need to be determined by using Newton's method. The matched solutions of the generalized envelope equations are shown in FIGS. 9A-9E for a non-axisymmetric beam system with the choice of system parameters corresponding to: $k_{0x}=3.22 \text{ cm}^{-1}$, $k_{0y}=5.39 \text{ cm}^{-1}$, $\sqrt{\kappa_z}=0.805 \text{ cm}^{-1}$, $K=1.53 \times 10^{-2}$ and axial periodicity length $S=0.956 \text{ cm}$.

In particular, FIG. 9A demonstrates the envelopes associated with the functions $a(s)$ and $b(s)$. FIG. 9B is graphical representation of rotating angle $\theta(s)$. FIG. 9C is a graph illustrating velocity

$$\mu_x(s) = \frac{1}{a} \frac{da}{ds}. \quad (2.17)$$

FIG. 9D is a graph demonstrating velocity

$$\mu_y(s) = \frac{1}{b} \frac{db}{ds}. \quad (2.18)$$

FIG. 9E is a graph demonstrating velocities $\alpha_x(s)$ and $\alpha_y(s)$ versus the axial distance s for a flat, ellipse-shaped, uniform-density charged-particle beam in a 3D non-axisymmetric magnetic field.

The matching from the charged-particle diode to the focusing channel might not be perfect in experiments. If a mismatch is unstable, it might ruin the beam. However, investigations of small-mismatch beams show that the envelopes are stable against small mismatch.

For example, the envelopes and flow velocities are plotted in FIGS. 10A-10E for a non-axisymmetric beam system with the choice of system parameters corresponding to: $k_{0x}=3.22 \text{ cm}^{-1}$, $k_{0y}=5.39 \text{ cm}^{-1}$, $\sqrt{\kappa_z}=0.805 \text{ cm}^{-1}$, $K=1.53 \times 10^{-2}$ and axial periodicity length $S=0.956 \text{ cm}$ with an initial 5% mismatch of θ , i.e. $\theta(s=0)=0_{\text{matched}}(s=0) \times (1.05)$.

In particular, FIG. 10A demonstrates the envelopes associated with the functions $a(s)$ and $b(s)$. FIG. 10B is graphical representation of rotating angle $\theta(s)$. FIG. 10C is a graph illustrating velocity

$$\mu_x(s) = \frac{1}{a} \frac{da}{ds}$$

FIG. 10D is a graph demonstrating velocity

$$\mu_y(s) = \frac{1}{b} \frac{db}{ds}$$

FIG. 10E is a graph demonstrating velocities $\alpha_x(s)$ and $\alpha_y(s)$ versus the axial distance s for a flat, ellipse-shaped, uniform-density charged-particle beam in a 3D non-axisymmetric magnetic field.

By the technique described herein, one can design a non-axisymmetric magnetic focusing channel which preserves a uniform-density, laminar charged-particle beam of elliptic cross-section.

One can illustrate how to match an elliptic charged-particle beam from the non-axisymmetric diode, described herein, into a periodic quadrupole magnetic field. In the paraxial approximation, the periodic quadrupole magnetic field is described by

$$B^{ext} = \left(\frac{\partial B_z^q}{\partial y} \right)_0 (y\hat{e}_x + x\hat{e}_y). \quad (3.1)$$

The concept of matching is illustrated in FIGS. 11 and 12.

FIG. 11 shows an example of the magnetic focusing parameter

$$k_q(s) = \frac{q}{\gamma_b \beta_b m c^2} \left(\frac{\partial B_z^q}{\partial y} \right)_0 \quad (3.2)$$

associated with the periodic quadrupole magnetic field for a beam of charged particles with charge q , rest mass m , and axial momentum $\gamma_b \beta_b m c$.

FIG. 12 shows the envelopes for pulsating elliptic beam equilibrium in the periodic quadrupole magnetic field, as described previously.

The matching of the equilibrium state from the diode to the equilibrium state for the periodic quadrupole magnetic field at $s=0$ is feasible, because the transverse density profile and flow velocity of the two equilibrium states are identical at $s=0$. In particular, the transverse particle density is uniform within the beam ellipse and the transverse flow velocity vanishes at $s=0$.

Also, one can illustrate how to match an elliptic charged-particle beam from the non-axisymmetric diode, as described herein, into a non-axisymmetric periodic permanent magnetic field. In the paraxial approximation, the non-axisymmetric permanent magnetic field is described by Eq. (2.8). The concept of matching is illustrated in FIGS. 13 and 14.

FIG. 13 shows an example of the magnetic focusing parameter

$$\sqrt{k_z(s)} = \frac{q B_z(s)}{2 \gamma_b \beta_b m c^2} \quad (4.1)$$

associated with the non-axisymmetric periodic permanent magnetic field (presented for a beam of charged particles with charge q , rest mass m , and axial momentum $\gamma_b \beta_b m c$).

FIG. 14 shows the envelopes for a flat, elliptic beam equilibrium state in the non-axisymmetric periodic permanent magnetic field. The angle of the ellipse exhibits slight oscillations. However, these oscillations can be corrected by utilizing higher longitudinal harmonics of the magnetic field profile.

The matching of the equilibrium state from the diode to the equilibrium state for the non-axisymmetric periodic permanent magnetic field at $s=0$ is feasible, because the transverse density profile and flow velocity of the two equilibrium states are identical. In particular, the transverse particle density is uniform within the beam ellipse and the transverse flow velocity vanishes at $s=0$.

The matching procedure discussed herein illustrates a high quality interface between a non-axisymmetric diode and a non-axisymmetric magnetic focusing channel for charged-particle beam.

This beam system will find application in vacuum electron devices and particle accelerators where high brightness, low emittance, low temperature beams are desired.

Although the present invention has been shown and described with respect to several preferred embodiments thereof, various changes, omissions and additions to the form and detail thereof, may be made therein, without departing from the spirit and scope of the invention.

What is claimed is:

1. A charged-particle beam system comprising a non-axisymmetric diode that forms a non-axisymmetric beam having an elliptic cross-section; and

a focusing channel that utilizes a magnetic field for focusing and transporting said elliptic cross-section beam.

2. The charged-particle beam system of claim of 1, wherein said charged-particle beam possesses a uniform transverse density.

3. The charged-particle beam system of claim of 1, wherein said charged-particle beam possesses a laminar flow.

4. The charged-particle beam system of claim of 1, wherein said charged-particle beam possesses a parallel longitudinal flow.

5. The charged-particle beam system of claim 1, wherein said focusing channel comprises a non-axisymmetric magnetic field for focusing and transporting said charged-particle beam.

6. The charged-particle beam system of claim 5, wherein said non-axisymmetric magnetic field includes a non-axisymmetric periodic magnetic field.

7. The charged-particle beam system of claim 5, wherein said non-axisymmetric magnetic field includes a non-axisymmetric permanent magnetic field.

8. The charged-particle beam system of claim 5, wherein said non-axisymmetric magnetic field includes a non-axisymmetric periodic permanent magnetic field.

9. The charged-particle beam system of claim of 5, wherein said non-axisymmetric magnetic field includes at least one quadrupole magnetic field.

13

10. The charged-particle beam system of claim of 5, wherein said non-axisymmetric magnetic field includes a periodic quadrupole magnetic field.

11. The charged-particle beam system of claim 2, wherein said focusing channel comprises a non-axisymmetric magnetic field for focusing and transporting said charged-particle beam.

12. The charged-particle beam system of claim 11, wherein said non-axisymmetric magnetic field includes a non-axisymmetric periodic magnetic field.

13. The charged-particle beam system of claim 11, wherein said non-axisymmetric magnetic field includes a non-axisymmetric permanent magnetic field.

14. The charged-particle beam system of claim 11, wherein said non-axisymmetric magnetic field includes a non-axisymmetric periodic permanent magnetic field.

15. The charged-particle beam system of claim of 11, wherein said non-axisymmetric magnetic field includes at least one quadrupole magnetic field.

16. The charged-particle beam system of claim of 11, wherein said non-axisymmetric magnetic field includes a periodic quadrupole magnetic field.

17. A method of forming a charged-particle beam system comprising

forming a non-axisymmetric diode that includes a non-axisymmetric beam having an elliptic cross-section; and

forming a focusing channel that utilizes a magnetic field for focusing and transporting said elliptic cross-section beam.

18. The method of claim 17, wherein said charged-particle beam possesses a uniform transverse density.

19. The method of claim 17, wherein said charged-particle beam possesses a laminar flow.

20. The method of claim 17, wherein said charged-particle beam possesses a parallel longitudinal flow.

21. The method of claim 17, wherein said focusing channel comprises a non-axisymmetric magnetic field for focusing and transporting said charged-particle beam.

14

22. The method of claim 21, wherein said non-axisymmetric magnetic field includes a non-axisymmetric periodic magnetic field.

23. The method of claim 21, wherein said non-axisymmetric magnetic field includes a non-axisymmetric permanent magnetic field.

24. The method of claim 21, wherein said non-axisymmetric magnetic field includes a non-axisymmetric periodic permanent magnetic field.

25. The method of claim 21, wherein said non-axisymmetric magnetic field includes at least one quadrupole magnetic field.

26. The method of claim 21, wherein said non-axisymmetric magnetic field includes a periodic quadrupole magnetic field.

27. The method of claim 18, wherein said focusing channel comprises a non-axisymmetric magnetic field for focusing and transporting said charged-particle beam.

28. The charged-particle beam system of claim 27, wherein said non-axisymmetric magnetic field includes a non-axisymmetric periodic magnetic field.

29. The charged-particle beam system of claim 27, wherein said non-axisymmetric magnetic field includes a non-axisymmetric permanent magnetic field.

30. The charged-particle beam system of claim 27, wherein said non-axisymmetric magnetic field includes a non-axisymmetric periodic permanent magnetic field.

31. The charged-particle beam system of claim of 27, wherein said non-axisymmetric magnetic field includes at least one quadrupole magnetic field.

32. The charged-particle beam system of claim of 27, wherein said non-axisymmetric magnetic field includes a periodic quadrupole magnetic field.

* * * * *